UNIVERSITÀ DI BOLOGNA

Dipartimento di Scienze della Terra
e Geologico-Ambientali

DOTTORATO IN SCIENZE DELLA TERRA
XIX° CICLO
Coordinatore: Prof. William Cavazza

Tesi di Dottorato

Magnetic structural evidences of the 41st parallel zone (Tyrrhenian Sea) inferred from potential field data: the 3D model of the discontinuity - GEO/10 -

Presentata da:
Dott. Luca Cocchi

Relatori
Dott. Fabio Caratori Tontini

Dott. Osvaldo Faggioni

Coordinatore Dottorato in Scienze della Terra
Prof. William Cavazza

Co-relatore
Dott. Michael Marani

Ciclo di studi 2004-2006

Contents

List of Figures

Introduction

Potential field data hold a leading role in geologic-structural applications, and becomes even more significant when applied to extremely inaccessible zones such as oceanic basins or non-anthropized areas. Aero-naval surveys make it possible to cover large areas in a short time in order to define their deep crustal features, which are otherwise not accessible by other direct methods. The analysis of magnetic field data is particularly effective in the study of those crustal portions characterized by lateral variations in magnetic susceptibility, and therefore magnetic analysis is often applied in areas where sub-volcanic bodies or relic portions of oceanic nature are located within sedimentary deposits.

The aim of this thesis is the development of a tridimensional model of the 41^{st} parallel zone departing from potential field data. The name 41^{st} parallel indicates a geographic zone lying along N41°of latitude, an area longitudinally defined between the Continental Campanian Margin (Gulf of Naples and Ischia and Procida islands) and the northeastern portion of the island of Sardinia.

From a geological point of view, the 41^{st} parallel is a complicated area containing a number of geological structures: submerged volcanic bodies such as the Vercelli and Cassinis seamounts, emerged edifices associated with the Pliocenic-Quaternary volcanism of the Central Tyrrhenian sea (Palmarola, Zenone, Ponza, Ischia and Procida) and several deep fault structures such as the E-W Ponza fault. It is still not clearly understood how the structural setting of the 41^{st} parallel zone was formed and developed, partly due to the fact that is an inaccessible area and its main geophysical evidence are represented by magnetic data.

Observation of the magnetic anomalous field shows an alignment of several magnetic anomalies along the N41°latitude lying on the main structural evidences of the area, which is in apparent conflict with the bathymetric data and related information. I therefore attempt to gain more detail from the magnetic data in order to provide a quantitative analysis giving further insight into the 41^{st} parallel

zone.

The magnetic data used for our 3D magnetic model is taken from the dataset of the Aeromagnetic Anomaly Map of Italy (Caratori Tontini et al., 2004). The original magnetic dataset includes the total intensity field of Italy and its surrounding seas acquired partly during the aeromagnetic surveys performed by Agip (now Eni-Spa) between 1971 and 1980 and partly during new surveys in the years 2001-2002 (Eni, Exploration & Production Division - Igmar, La Spezia). A cesium-magnetometer was used to record the magnetic data uniformly, after which the raw data was reprocessed to produce an updated magnetic anomaly map which contains a wealth of useful information in good agreement with the sea-level map of Chiappini et al. (2002).

In the first chapter of this thesis I describe the overall geological and structural features of the Tyrrhenian sea but I also analyse the 41^{st} parallel zone commencing from the data available in current literature. The second chapter evaluates the Bouguer gravity field of the Tyrrhenian Sea by using two methodologies in order to select an optimal Bouguer reduction density. This section includes details of the use of a free-air gravimetric satellite data set of the Tyrrhenian sea to plot an isostatic level map of the central Tyrrhenian area.

In the third chapter the properties of the geomagnetic field and its representation are described with particular attention to the time and spatial dependencies of the field. The fourth section goes on to give details of the raw magnetic data used for the quantitative elaboration and to describe the characteristics of the anomaly field of the study area. The fifth chapter explains how the properties of the magnetic signal were studied by applying a statistical analysis of the power spectrum (Spector and Grant, 1970) and a Continuous Wavelet Transform. Following on from these analyses, in the sixth chapter I introduce the concept of the magnetic basement and the relationship between magnetic signal and temperature. Departing from the regional heat-flow data (Della Vedova et al., 2001) of the Central Tyrrhenian area, a Curie Isotherm surface model was produced defining the maximum depth of the

magnetic-thermal basement. The boundaries of the magnetic sources (top and bottom) represent the base-line for the subsequent quantitative analysis steps, in which a 2D inversion algorithm was used to obtain an apparent susceptibility map. The seventh chapter illustrates how this algorithm was applied to the magnetic evidence of the 41^{st} parallel zone and to the Selli Line region, and how this procedure suggests a distribution of magnetization that connects the 41^{st} parallel zone with structural elements of the Southern Tyrrhenian Sea such as the Magnaghi Basin and the Selli Line fault system. In practical terms the results obtained from the apparent magnetization maps were used as a basis for a 3D inversion of magnetic data which was to provide information on the vertical distribution of the sources.

The eighth chapter, which represents a key part of the thesis, describes the inverse problem in the potential field analysis introducing a new 3D algorithm capable of evaluating the depth to the bottom of the source. Next, this algorithm was applied to the real magnetic dataset of the 41^{st} and Selli Line regions, plotting models which show the shape, location in depth and direction of development of the magnetic generating sources and thus suggesting the geometric relationships between the different sources themselves, this information being important for evaluation of the crustal setting of the study area. Finally, in the last chapter I interpret the results of the inversion process to assess the relationship between the 41^{st} parallel and the Selli Line region. This proves how the magnetic models of these two regions were successfully processed to provide a chronological reconstruction of the geodynamic evolution of the Central Tyrrhenian Sea.

Introduzione

I dati di potenziale rivestono un ruolo molto importante nello studio geologico-strutturale di un'area. Il loro utilizzo diventa ancora più importante se applicato a zone estremamente inaccessibili come bacini oceanici o aree poco antropizzate. Utilizzando vettori di acquisizione di tipo aereo e/o navale è possibile coprire grandi aree in poco tempo e definire così le caratteristiche strutturali medio-profonde di aree poco esplorabili con altri metodiche di indagine di tipo diretto. L'analisi dei dati di campo magnetico si rivela estremamente importante laddove esiste un assetto geologico strutturale caratterizzato da variazioni laterali di suscettività magnetica dovuto alla presenza di corpi vulcanici o a porzioni relitte crosta oceanica.

Lo scopo di questa tesi è quello di costruire un modello tridimensionale del comprensorio geografico del 41° *parallelo partendo da dati di potenziale. Con il termine* 41° *parallelo si indica una fascia geografica allineata lungo latitudine N*41° *e longitudinalmente compresa tra il margine continentale campano (Golfo di Napoli, Ischia e Procida)e la zona nord orientale della Sardegna.*

Da un punto di vista geologico il 41° *parallelo rappresenta una zona estremamente complicata. Lungo tale fascia geografica sono localizzate strutture geologiche di varia natura: edifici vulcanici sommersi (Etruschi, Vercelli e Cassinis Seamount), evidenze emerse del vulcanismo Pliocenico-Quaternario dell'area Centro Tirrenica come Palmarola, Zenone, Ponza, Ischia e Procida, nonchè sistemi di faglie profonde come quella localizzata a Nord del Golfo di Napoli. La formazione di questo particolare allineamento non è ancora chiara ed è oggetto di dibattito in letteratura. L'evidenza di un allineamento di strutture lungo il* 41° *parallelo è osservabile preferenzialmente da dati magnetici. Il campo di anomalia magnetica mostra una distribuzione preferenziale E-W di anomalie in corrispondenza della latitudine N41, tali evidenze magnetiche sono impostate in corrispondenza dei corpi magmatici, sia emersi che sommersi che lungo le zone di faglia. I dati di batimetria e gli altri dati geofisici non evidenziano tale caratteristica. Proprio per questo motivo ho scelto*

di utilizzare i dati magnetici per analizzare in modo quantitativo le caratteristiche crostali di quest'area.

I dati magnetici utilizzati in questa tesi derivano da un dataset più grande, comprendente i dati di tutta l'Italia e dal quale è stata recentemente realizzata la Mappa Aeromagnetica d'Italia (Caratori Tontini et al., 2004). Il dataset originario è costituito da dati di campo magnatico totale relativo alla penisola italia e alle zone marine limitrofe. Questi dati sono stati acquisiti da Agip (ora Eni Spa) mediante diversi rilievi aerei effettuati in una prima fase tra il 1971 e il 1980 e successivamente integrati da nuovi acquisizioni avvenute tra il 2001-2002 (Eni, Exploration & Production Division in collaborazione di IGmar, La Spezia). Grazie ad una fitta copertura dell'area è stato possibile ottenere una omogenea acquisizione, inoltre l'utilizzo di un magnetometro al cesio ha fornito dati di grande qualità. Il reprocessing dei dati così acquisiti ha fornito una dettagliata mappa di anomalia magnetica in buon accordo con la già nota Carta di Anomalia Magnetica acquisita a livello del mare di Chiappini et al. (2002).

Nel primo capitolo di questa tesi ho introdotto, in via generale, le caratteristiche geologico-geofisiche dell'area tirrenica e dell'area del 41° *parallelo partendo dalle principali informazioni di bibliografia esistente. Nel secondo capitolo ho ricostruito il campo di anomalia di Bouguer partendo da dati di gravità in aria libera da satellite. Il valore ottimale della densità di riduzione di Bouguer per l'area in analisi è stato simato combinando un approccio frattale alla correlazione tra Bouguer e batimetria. Nel terzo e quarto capitolo vengono descritte le principali caratteristiche del campo magnetico terrestre del campo anomalo e successivamente vengono analizzati i dati di anomalia magnetica relativi alla zona del Mar Tirreno. Il contenuto principale del quinto capitolo è rappresentato dall'analisi informativa del segnale magnetico associato alle strutture crostali medio-profonde dell'area. Lo studio statistico degli spettri di potenza fornisce informazioni sulla distribuzione in profondità delle sorgenti di anomalia (Spector and Grant, 1970). Inoltre per una relazione quantitativa segnale magnetico-posizione geografica della sorgente, il campo magnetico è stato*

analizzato mediante la Trasformata Continua di Wavelet. Nel sesto capitolo viene introdotto il concetto di basamento magnetico mediante la costruzione di un modello termico. Partendo da dati di flusso di calore regionale dell'area Centro Tirrenica ho valutato la profondità della superficie isoterma di Curie definendo così un limite inferiore della porzione crostale magnetizzata. Una volta identificata la porzione di crosta magneticamente valutabile ho applicato un algoritmo d'inversione bidimensionale per valuare la distribuzione della suscettività magnetica. Questa analisi è applicata alle evidenze magnetiche del 41° *parallelo ed a quelle delle zone limitrofe come l'area della Linea Selli e del bacino del Magnaghi. Le mappe di magnetizzazione apparente di queste due aree sono riportate, commentate ed interpretate nel settimo capitolo L'ottavo capitolo rappresenta una parte molto importante della tesi, in quanto, viene descritto un nuovo algoritmo d'inversione tridimensionale per i dati di potenziale. Tale algoritmo è strutturato in due parti, una prima dove si può stimare preventivamente il limite inferiore della sorgente (chiusura verso il basso) e una seconda dove si ricostruice matematicamente la sorgente nelle sue 3 dimesioni. I modelli tridimensionali ottenuti applicando questo algoritmo sono molto informativi in quanto, evidenziano la forma, dimensione, profondità e modalità di crecita nelle tre dimensioni delle sorgenti di anomalia. Nel nono capitolo ho applicato questa procedura d'inversione sia all'area del* 41° *parallelo che alle strutture abissali del Mar Tirreno Meridonale. Nell'ultimo capitolo si racchiude la parte d'interpretazione dei modelli d'inversione ottenuti precedentemente in modo da definire l'assetto geologico strutturale del'area. In questo contesto ho valutato le possibili relazioni esistenti tra l'allineamento del* 41° *parallelo e la Line Selli. Dallo studio dei modelli magnetici ottenuti dall'inversione relativi a queste due zone è nato un possibile modello interpretativo della evoluzione geodinamica del Tirreno centrale.*

1 The Tyrrhenian area

This chapter describes the main geological and geophysical characteristics of the Tyrrhenian sea area, with particular attention to those features which distinguish the Southern Tyrrhenian basin from its Northern counterpart.

The differing structural settings of these two Tyrrhenian domains are due to the uneven rate of stretching which occurred in the European continental crust (Patacca et al., 1990; Royden, 1988; Malinverno and Ryan, 1986).

Since the lineament of the 41^{st} parallel is located at the boundaries of these two Tyrrhenian domains, evaluation of the geological and geophysical features of the Tyrrhenian sea provides key data for interpretation of the nature and development of the 41^{st} parallel. To this aim, a detailed description is provided of the magmatic features, deep crustal setting, shallow heat flow distribution and Bouguer anomaly field of the Tyrrhenian sea, followed by analysis of the geologic-structural setting of the 41^{st} parallel zone in the light of the major theories concerning its nature and evolution.

1.1 The geodynamic setting

The Tyrrhenian sea, a Tortonian-Pleistocenic back-arc basin of triangular shape, is the easternmost basin of the Western Mediterranean sea. One result of the geodynamic evolution of the Mediterranean area was the opening of the Tyrrhenian as partial consequence of an extensional tectonic starting in the Provençal and Valencia and progressively moving to Algeria and the Tyrrhenian Basin (Doglioni et al., 1991, 1999, 2004; Patacca et al., 1990). An eastward migration of the subduction system in the Central Mediterranean Sea between the Oligocene and Present was associated with stretching of the continental crust with a basin formation. The Tyrrhenian Sea is thus an abyssal basin formed by flexural withdrawal of the subduction (Patacca et al., 1990; Royden, 1988; Malinverno and Ryan, 1986). In this area the compression setting generated by a westward subduction movement of the

Africa Plate under the European continental plate came to an end during the Early Tortonian, at which time the strong eastward migration of the subduction system was superimposed over the compressional movement. The link between evolution of the back-arc rift and movement of the Apennine subduction is supported by a coeval evolution of the two processes and the eastward migration itself: the largest opening of the Southern Tyrrhenian Sea occurred at a point corresponding to with the maximum subduction depth of the Calabrian slab where the oceanic lithosphere is involved (Catalano et al., 2001; Doglioni et al., 2004). It may also be suggested that the eastward migration of the subduction system is connected to an underlying mantle flow pushing eastward against the subduction plate (Doglioni et al., 1999; Gueguen et al., 1997).

During the Tortonian-Quaternary the rate and direction of the opening of the Tyrrhenian sea was not continuous, as is shown by the presence of features such as uneven distribution of magmatic episodes (submerged volcanic edifices) connected to the rifting phase and to the chronological variation of the opening process. In the Tyrrhenian area the eastward migration and consequently the opening process commenced in a W-E direction in the Tortonian: while the southeastern part of the basin was affected by an opening process in a SE direction (Pliocene) (Fig.1), the rifting process evolved separately in the Northern Tyrrhenian portion with a different opening rate. Specifically, the average rate of the Northern Tyrrhenian Sea is 1.5-2 cm/y (Facenna et al., 1997) in contrast to the 5-6 cm/y of the Southern domain (Patacca et al., 1990), this difference being caused by the nature of the subducting lithosphere, which is continental in the Adriatic Sea and oceanic and heavier in the Ionian area (Doglioni et al., 2004).

The Northern Tyrrhenian is a roughly triangular sea extending between 41°N and beyond 42°30'N (fig. 1.1). The tectonic-structural setting of this area is characterized by several rotated crustal blocks with low-angle extensional faults associated with high-angle faults such as the Basin and Range Provinces (Marani and Gamberi, 2004). In this area the extension and crustal thinning are related to a system

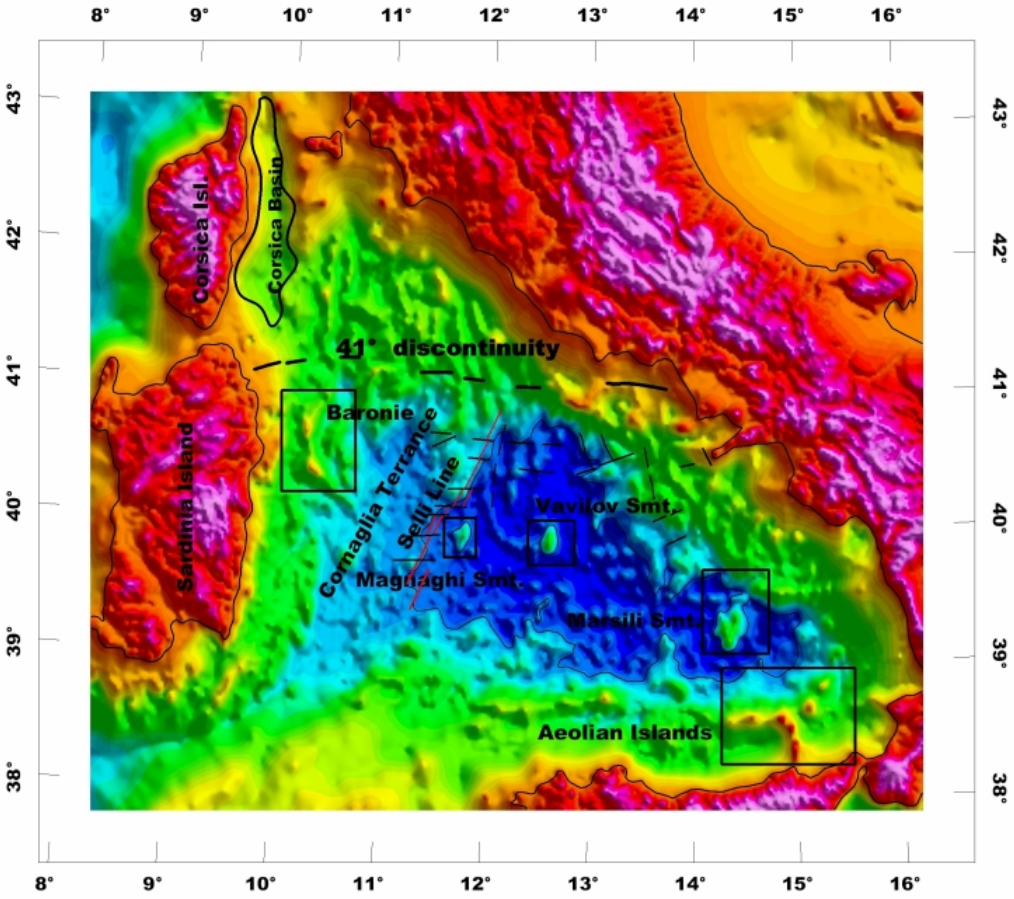

Figure 1.1: Reconstruction of the main geologic/structural evidences of the Tyrrhenian Sea

of crustal shear zones and a chronological movement of magmatism from Corsica (older events) to the Apennine (younger events) (Serri et al., 1993; Facenna et al., 1997). The western portion of this domain (Corsica basin)contains 15-20 Ma old syn-rift deposits whereas in the Apennine sector the deposits are estimated to be 2 Ma old and the normal faults are still active (Bartole, 1995; Marani and Gamberi, 2004). The eastward migration of the subduction system caused an eastward shift of the extensional basin and of volcanism, this movement being of smaller proportions due to a lower rate of migration, an extension of approximately 25 km having been calculated for this area (Doglioni et al., 2004). Bathymetric data of the northern

Tyrrhenian Sea show its oldest basin running N-S with a younger NNW-SSE system of structural highs (Facenna et al., 1997).

The Southern Tyrrhenian is characterized by a peculiar structural setting due to the higher rate of eastward migration of the subduction system. Morphologically, this domain is a deep abyssal basin floored with a new oceanic crust. In the Southern Tyrrhenian Basin, the syn-rift deposits are 10-12 Ma old in the Sardinia Basin and approximately 5 Ma in the Vavilov Basin (Kastens et al., 1988; Sartori et al., 1990; Facenna et al., 1997). The initial rifting episodes first occurred in the Upper Tortonian and were coeval on both the Calabrian and Sardinian Margins. The evolution of the rifting progressed in an E-SE direction with stretching of the continental crust and successive magmatic activity.

The accretion of the new oceanic crust is the result of two main episodes, the first of which occurred at a location corresponding to the current position of the Vavilov basin and the second in the Marsili area. The accretion of new oceanic crust in the Vavilov basin is estimated to be between 4.5 and 2.6 Ma old (ODP 650) while the Marsili basin (ODP 651) is dated at approximately 1.8-2.0 Ma (Kastens et al.,1988; Serri et al., 2001; Sartori, 2001). The abyssal southern Tyrrhenian Sea, which includes these two sub-basins, is bordered by several structural evidences such as the Central Fault and the Pontine-Palinuro continental slope region. The Central Fault, also known as the Selli Line, is a normal fault system dipping in a SE direction, which divides the active extensional basin from the passive Sardinia Margin. This fault system extends NW-SE between the Magnaghi region and the Cornaglia Terrace, the latter being a Late Miocene system of N-S grabens (Van Djik and Scheeper, 1995) considered as the eastern portion of the Sardinia margin. The Selli Line, bathymetrically a deep escarpment of 800-1000 meters, is considered the real Northwestern border of the southern Tyrrhenian sea, whose NE margin instead is bordered by the Pontine-Palinuro continental slope. This region is considered as an active margin province of the Tyrrhenian system (Marani and Gamberi, 2004). In this area, the continental slope extends in a NNW-SSE direction defined by a

normal fault system. This morphologic structure is a west-dipping master fault stretching for 80 km with an increasing throw southwards from 400 to 1 km (Marani and Gamberi, 2004). Musacchio et al.(1990) have interpreted this fault system as a transtensive system with leftward movement. Finally, the Southern Tyrrhenian basin is bordered by a major strike-slip fault on the northward margin of Sicily running E-W (Rosembaum and Lister, 2004), along which are located several magmatic structures such as Ustica and the Alcione and Anchise Seamounts (Savelli, 2002).

1.2 The distribution of magmatism

The most significant magmatic activity in the Tyrrhenian Sea area occurred between the Early Oligocene and the Quaternary, during which the several magmatic episodes are related to different geodynamic processes. The Tyrrhenian domain is characterized by subduction-related magmatism products (calc-alkaline affinity), intraplate alkaline magmatism and MORB type basalts (Serri, 1993; Serri et al., 2001; Savelli, 2002 and references therein). Data on the time-space distribution of the calc-alkaline subduction-related magmatism makes it possible to recreate the movement of the subduction system. The calc-alkaline magmatism occurrences become younger from the western Tyrrhenian margin to the Eastern side as a result of the eastward migration of the subduction system.

The evidence of Oligo-Miocene calc-alkaline magmatism is visible in the Sardinia and Corsica regions. During this period (32-13 Ma, Serri et al., 2001 or 30-15 Ma as proposed by Savelli, 2002), basalt, basaltic andesites, HK-andesites and ignimbritic rhyolites were erupted into the area (Savelli, 2002 and references therein). The petrogenesis of these products is connected to a northwestward oceanic subduction below Sardinia (Serri et al., 2001). In southwestern Corsica arc-magmatism developed during the Burdigalian (17 Ma.)(Serri et al., 2001) while the subsequent calc-alkaline magmatism phase (13-7 Ma)is highlighted by several N-S striking magmatic centers located in the North Tyrrhenian Sea such as the island of Montecristo and

the Vercelli Seamount (Serri et al., 1993; Rosembaum and Lister, 2004). The Vercelli Smt is a granitic intrusion set into the shallow stretched crust of the North Tyrrhenian dated 7.5 Ma old (Barberi et al., 1978; Savelli, 1988). This intrusion could be associated with the change from compressional to extensional geodynamics of the Tyrrhenian basin (Barberi et al., 1978). The subduction-related magmatism activity continued during the Messinian, migrating from the Sardinia-Corsica area to the Apennine margin. This magmatic phase also includes the monzogranite-granodiorite of Mount Capanne on the Island of Elba and the andesite-dacitic effusion of Capraia Island (Serri et al., 1993; Savelli, 2002). Commencing in the Messinian, an eastward movement of the subduction system took place in the southern Tyrrhenian sea and stopped in the northern portion. The high rate of eastward extension in this area has been estimated at 5-6 cm/yr (Patacca et al., 1990; Doglioni, 1991; Facenna et al., 1997)and the fast extension led to considerable stretching of the continental crust and subsequently accretion of new oceanic crust.

The Southern Tyrrhenian is divided into two main sub-basins: the Vavilov and the Marsili. The Vavilov basin is characterized by two submerged volcanic edifices with MORB/OIB composition (Serri et al., 2001), the Magnaghi and the Vavilov Smts, both of which show similar NNE-SSW structural trends. The Magnaghi, whose age has been estimated at 2.7-3.0 Ma (Sartori et al., 2004), is located westward of the Selli line fault system, and its drilled lava samples(ODP 654) are alkaline-weakly alkaline basalts with a MORB/OIB chemism (Robin et al., 1987; Savelli, 1988; Serri et al., 2001). The Vavilov Seamount extends in a N-S direction for a distance of 30 km, with its bottom lying at a depth of 3600 m b.s.l. Formation of this seamount occurred at a later stage following oceanization of the Vavilov basin at approximately 2.4-3.0 Ma (Kastens et al., 1987). The Vavilov is asymmetric in shape, its western flank having a steeper gradient than the eastern side probably due to a flank collapse or main fault (Marani and Gamberi, 2004), and its lava is mainly alkaline basalt (ODP-drilling site 650).

The southeastern oceanic sub-basin of the Tyrrhenian Sea, the Marsili, is

formed by a basalt crust associated with an extension running axially E-SE and dated $<$ 2Ma (Kastens et al., 1990). The Marsili basement has a transitional MORB-type basalt composition (ODP-drilling site 650) (Serri et al., 2001). From the center of this basin rises the Marsili seamount, a large structure extending for 50 km NNE-SSW and rising to a height of 3500 m from the bottom of the basin. In terms of age it is estimated that the Marsili basin was formed between 1.87-1.67 Ma (Kastens et a., 1988), while the lava of the upper portion of the volcano is dated around 0.1-0.2 Ma (K/Ar chronological data)(Selli e al., 1977). Evaluation of the magnetic pattern suggests that the seamount was created between 0.78 and 0.1 Ma (Crones C1-Brunes, normal polarity), while the negative magnetization of the external portion of the volcano appears to be indicative of a Olduvai-Late Matuyama age (Savelli and Schroeder, 1991; Schroeder et al., 1993). These features point to a fast accretion (lasting 0.78 Ma) of the Marsili edifice (Marani,2004; Nicolosi et al., 2006).

Quaternary magmatism of the southern Tyrrhenian Sea is represented by the Aeolian arc, a volcanic island arc caused by subduction of the Ionian plate under the continental European plate and, along with the Aegean arc, the only active island arc in the Mediterranean Sea. The Aeolian arc consists of seven islands and several seamounts in which magmatic activity commenced around 1.3-1 Ma in the Sisifo seamount and Filicudi island (Serri et al., 2001) and subsequently spread to the eastern portion of the arc, where volcanism is still active. The composition of erupted materials from approx 0.8 Ma to the present is dominated by shoshonitic and calc-alkaline/High-K calc-alkaline chemism, and in the active sector of the emerged arc it is possible to observe an evolution of products from calc-alkaline/High-K calc-alkaline (older series) to shoshonitic (younger series)(Serri et al., 2001). The petrogenetic nature of Aeolian arc basalt is attributed to MORB/OIB sources contaminated by dehydration of the subducted oceanic crust and by the subduction of sediment (Ellam et al., 1988; Serri, 1990; Francalanci et al., 1993; Francalanci and Manetti, 1994).

1.3 The thermal regime

The distribution of the shallow heat flow may indicate a variation in the physical features of a deep crustal portion. Generally speaking, the thermal pattern is closely connected with the tectonic-geodynamic setting and in fact the Tyrrhenian Sea shows a thermal setting compatible with the extension process which developed as the basin opened. The different rate of extension in the northern and southern Tyrrhenian areas is also demonstrated by the pattern of the surface heat flow field.

A number of studies into the heat flow of the Italian-Tyrrhenian region have been carried out over the last ten years, producing various regional maps (Mongelli and Zito, 1994; Cataldi et al., 1995; Della Vedova et al., 1995; Della Vedova et al., 2001), the latter being the most recent.

As a general rule the on-shore portions of the Italian Peninsula give an average shallow heat flow reading around 120-150 mW/m^2, which is lower than the average value of the entire Tyrrhenian Sea (200-230 mW/m^2). This thermal pattern is shown in figure 1.2 (redrawn after Della Vedova et al., 2001). As can be seen from Fig. 1.2, in the northern Tyrrhenian domain the heat flow values range from 80 to 120 mW/m^2 and tend to be evenly distributed. The highest values are recorded in the Tuscan-Latium archipelago, the geothermical setting of the local volcanic district. The northern Tyrrhenian domain is separated from the southern area by an E-W lineament along the 41^{st} parallel, which exhibits lower heat flow values (approx $80mW/m^2$), suggesting that this lineament also represents a zone of thermal differentiation between the northern and southern domains.

The heat flow field of the Southern Tyrrhenian basin is instead characterized by high values (max $250mW/m^2$, located in the Marsili area) with a non-homogeneous pattern. The shallow heat flow distribution of this area is affected by the deep meteoric water infiltration (see Vavilov basin) and by thermal convective systems (Aeolian arc, Marsili basin) (Della Vedova et al., 2001). Yet another factors influencing this area, in addition to the usual radiogenic contribution are the mantle

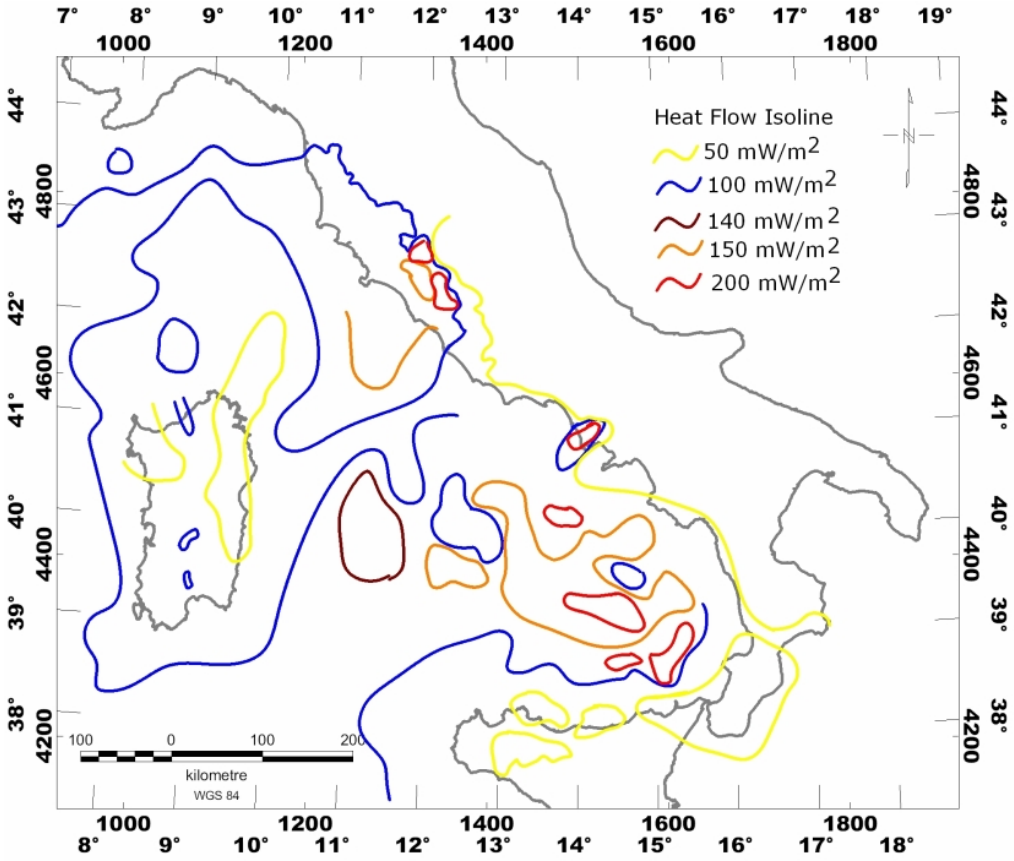

Figure 1.2: Map of surface heat flow, modified after Della Vedova et al.(2001)

component and the effect of asthenospheric intrusion. From a thermal point of view, the local extension of the crust and the successive intrusion of asthenospheric material is considerable, as shown in a thermal model of the southern Tyrrhenian basin (Zito et al., 2003), which estimates that the high heat flow values of the two sub-basins, Vavilov and Marsili, are respectively associated with the asthenospheric intrusions at depths of 11.2 and 10 km.

1.4 Moho isobaths and lithosphere thickness

An in-depth analysis of the distribution of seismic wave velocities is a important tool for the study of the deep-seated features of the upper and lower crust.

Seismic waves are generated artificially by dynamite shoots onshore and with air gun arrays in offshore areas. This explorative method is generally useful to determine the distribution and properties of the deep crust structures, especially when reflection and refraction seismic methodologies are applied to obtain a better image of the low crust features such as the main discontinuity zone and location of undefined bodies. A seismic prospection is obtained by localizing the seismic reflection and interpreting the results. To give an example, a transparent zone in the seismic section may indicate the presence of intrusive bodies while in the lower crust an abrupt termination of seismic reflectors may indicate the location of a crustal-mantle discontinuity (Mohorovich) reflection. Where there is a Moho-discontinuity the p-wave velocities decrease, an effect caused by a change in the petrographic properties of the crust (Nicolich, 2001). A number of reconstructions of Mohorovich discontinuity distribution have been carried out in recent decades (Locardi and Nicolich, 1988; Nicolich and Dal Piaz, 1992; Nicolich, 1989, 2001), and the latest map of Moho isobaths of the Ionian and Tyrrhenian area was plotted by Scarascia et al.(1994). Figure 1.3 gives a map of the Moho isobaths of the Tyrrhenian Sea, redrawn after Nicolich (2001).

In the Italian Peninsula the crust is of continental nature, in contrast with the Pliocenic oceanic crust of the southern Tyrrhenian Sea and the Ionian area, which is believed to have a Mesozoic oceanic crust (Catalano et al., 2001). Seismically, the Tyrrhenian Sea is divided by the 41^{st} parallel zone into two main structural domains (Spadini and Wezel, 1995), which are also associated with two distinct mantle domes: the Tuscany archipelago and the southern Tyrrhenian sea (Nicolich, 2001). The Moho isobath map highlights features linked with the rift processes of the continental crust, with the southern Tyrrhenian showing evidence of vertical evolution of mantle swell and, in addition, a differentiating mantle from West to East (Locardi and Nicolich, 1988)

Characterization of the lithosphere-asthenosphere transition is based on deep seismic sounding data and analysis of surface wave dispersion (Panza et al.1980 ;

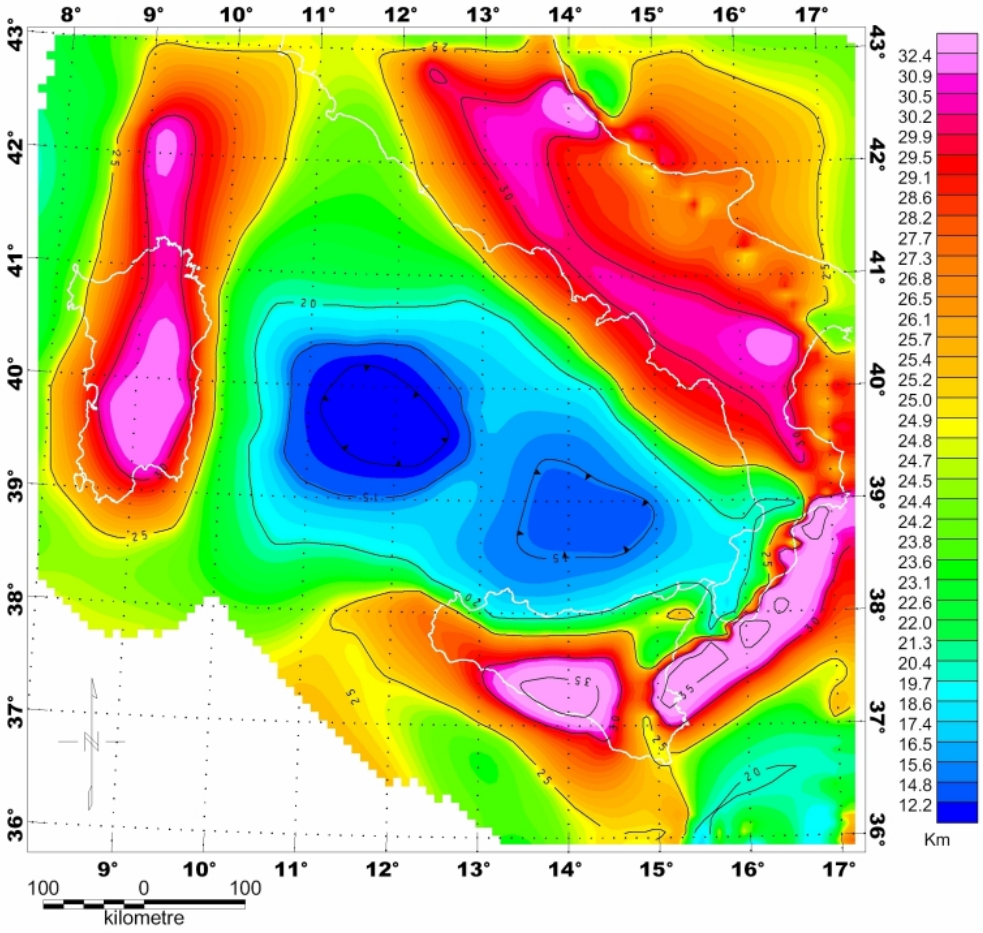

Figure 1.3: Map of the Moho-isobaths of the Italy region, after Nicolich (2001)

Calcagnile and Panza, 1980; Panza et al., 2003). I refer to a map of the lithosphere thickness of Italy and its surrounding seas compiled by Panza and Suhadolc (1990). By distribution of the average sub-Moho shear-wave velocities (V_s), the Tyrrhenian Sea area is divided in two domains, the southern basin and the Tuscan area (Panza et al., 1982; Suhadolc and Panza,1987; Della Vedova et al., 1991). The northern Tyrrhenian portion, near the Tuscan archipelago, is characterized by V_s=4.2-4.35 Km/s associated with a continental lithosphere thickness of approx 60-70 km in an area which does not have a high-velocity lid (Calcagnile and Panza, 1980; Panza et al., 1980; Suhadolc and Panza, 1987; Della Vedova et al., 1991). The other

lithospheric domain, which includes the central and southern Tyrrhenian sea, shows a lithosphere thickness of approx 30 km which is compatible with a young oceanic basin system (Della Vedova et al., 1991). The limit between the northern and southern domains is located slight southward of the 41 parallel. In this area the Moho is 7-10 km with V_s=4.1 Km/s. A low-velocity layerV_s=3.0 Km/s is located under the Moho-discontinuity, where a partial melting process is active (Bottiga and Steinmetz, 1979). The asthenosphere domain, under the low-velocity lid, shows an average shear wave velocity of approx 4.1-4.3 Km/s (Panza et al., 2003).

1.5 Bouguer anomaly field

The gravimetric field data is related to density variation of the crustal portion. A Bouguer anomaly map is plotted after free-air correction of the raw gravimetric data and subsequently the Bouguer reduction. The positive and negative Bouguer anomalies are associated with zones with densities higher or lower than the Bouguer reference density (usually $\rho = 2.67 g/cm^3$). Positive Bouguer anomalies are usually found where there is a gravimetric contribution of high density structures such as mantle intrusions ($\rho > \rho_{Bouguer}$).

Since 1960 a number of Bouguer anomaly maps of the Italian peninsula and surrounding sea have been plotted (Ballarin, 1963; Mongelli et al.,1975; Servizio Geologico Nazionale, 1989). A recent revision (1992) of the gravimetric data of Italy by CNR (the National Research Council) produced a 1:500000 map of the Italian region. Figure 1.4 gives this Bouguer anomaly map of Italy and the Tyrrhenian Sea. The Tyrrhenian Sea is dominated by a high gravity anomaly field with an increase from North to South: while the Bouguer anomaly field of the Northern Tyrrhenian Sea is positive, the readings are considerably lower than in the Southern area. The different gravity patterns of the Tyrrhenian Sea may be related to the differing rates of extension which occurred as the Tyrrhenian opened. Maximum positive values of gravimetric anomaly are located over the oceanic sub-basins, Vavilov (+250 mGal)

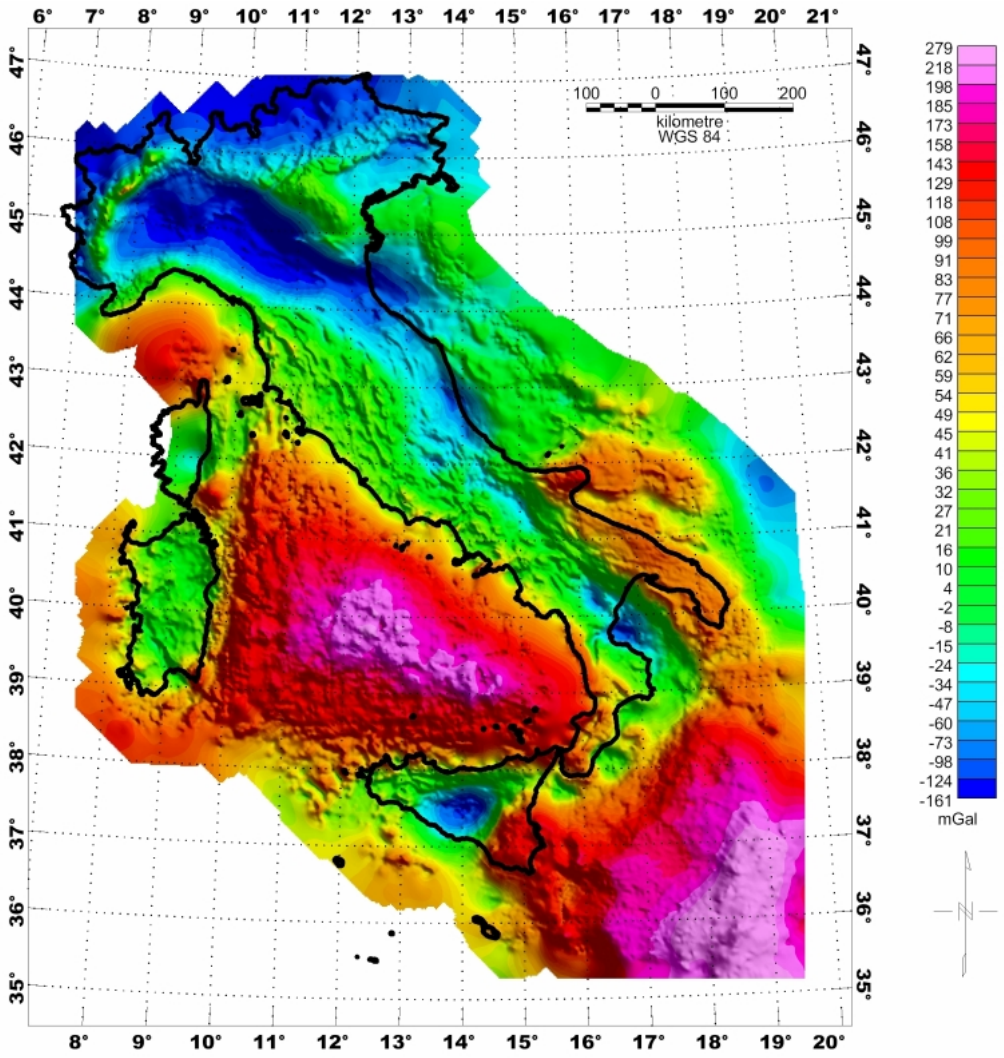

Figure 1.4: Bouguer anomaly map of Italy and Tyrrhenian Sea, contour line every 20 mGal, redrawn from CNR (1992)

and Marsili (+225-240 mGal). The two Tyrrhenian domains can be separated by observation of the shape and distribution of the anomaly field. In the Southern basin the gravimetric positive shows a shape similar to the bathymetric morphology of the basin and the anomalies run NE-SW like the Selli-line structure (Northwestern border of the basin), while northwards of 41^{st} parallel the gravity pattern is characterized by N-S oriented anomalies.

Chapter 2 contains a detailed study of the Bouguer anomaly of the Tyrrhenian area with implications on its isostatic setting.

1.6 The 41^{st} parallel area

The 41^{st} parallel represents the separation point between the Northern and Southern Tyrrhenian basin. Across this particular zone, the thermal regime, the lithosphere properties and the chemism of the magmatism change their behaviour.

In literature the 41^{st} parallel is well known for its magnetic patterns. Along this latitude, a pronounced lineament of magnetic anomalies is located between the Sardinia Margin and the Campanian area. The magnetic lineament is connected with structures of different geologic nature such as intrusive-submerged bodies, volcanic islands and a fault system. Moreover, several magnetic evidences are not correlated with shallow bathymetric structures.

The magnetic lineament can therefore be considered as an expression of a deep boundary between the two Tyrrhenian domains characterized by two distinct magnetic provinces. In the Northern Tyrrhenian domain the magnetic anomaly field is mainly associated with a low-frequency contribution in which the high-wavelength field represents the spectral contribution of the magnetic basement, where locally high-frequency magnetic evidences are shown. Southward of the 41^{st} parallel zone the magnetic pattern is dominated by a high frequency signal where it is possible to observe the highest magnetic anomaly values of the entire Tyrrhenian area. These high-frequency magnetic evidences are associated with several shallow crustal

structures of the southern Tyrrhenian basin, and the high-frequency anomalies are superimposed over a low-frequency field that clearly takes the shape of the Vavilov and Marsili oceanic sub-basins.

From a geological point of view, the 41^{st} parallel is characterized by a lineament of several structures of differing geologic nature stretching for a distance of approx 300 km connecting the Campanian coastal area to the northwestern margin of Sardinia. In the Western sector of this line (near the Sardinia Margin) there are small magmatic evidences such as the Vercelli granitic intrusion dated around 7.5-7 Ma (Barberi et al., 1978) and small Pleistocenic sub-volcanic bodies with tholeiitic chemism (Bigi et al., 1989) while Quaternary magmatic structures such as Ponza, Palmarola and Zenone outcrop at its eastern edge. The Plio-Pleistocenic genesis of these volcanic islands is linked with a subduction-related magmatism, with a particularly differing magmatic affinity with Ponza due to their different magmatic sources. The Pleistocenic rhyolites of Palmarola have a chemism linked to a OIB-type magmatic source, which may derive from an up-welling of deep material due to a extension during Tyrrhenian Sea opening (Cadoux et al., 2005). According to this new data the Pontine area represents the transitional zone between subduction-related magmatism and the opening process. The easternmost portion of the 41^{st} parallel, the Campanian margin, is characterized by emerged volcanic edifices of Quaternary magmatism such as Ischia and Procida, and by a deep vertical fault extending for 40 km E-W in the Gulf of Gaeta. Morphologically, the 41^{st} parallel does not show evidence of E-W fault features such as high escarpment and block dislocation. The western portion of the alignment shows several N-S trending structural highs associated with the morphology of the northern Tyrrhenian basin. The continental Campanian margin is divided from the abyssal oceanic basin of the Vavilov by a NW-SE escarpment located in the central-eastern portion of the 41^{st} parallel zone. In this area, several bathymetric structures change their displacement from E-W to NE-SW as if affected by an anti-clockwise rotation. The evidence of anti-clockwise rotated sources has been evaluated by Fedi (1990) through observation of

the changes in the magnetic anomaly pattern which suggests that these bathymetric structures are relict portions of the European crust which have been tectonically dislocated. Analysis of Crop Section M-29B leads to the conclusion that the crustal portion is the frontal thrust system of the Sardinia-Corsica block emplaced during the Balearic stage of anti-clockwise rotation (Finetti, 2003) in which the crustal blocks shifted SW during the Miocenic extension of the Tyrrhenian Sea. The allocthonous block instead consists of a lower and upper crust of European fragment (Calabrides) and in the upper portion of ligurides units and Plio-Quaternary sediments. Finally, in the eastern section the thrust block system is superimposed on the Apennine fragment (Mesozoic platform) (Finetti, 2003).

The 41^{st} parallel is a complicated structural-geologic area where the effects of different geodynamic processes are combined. Evaluation of the geophysical features of the 41^{st} parallel allows us to assess the role of this particular lineament on the forming process of the Tyrrhenian area. While it is accepted that the 41^{st} parallel is the transitional zone between two crustal (lithospheric) domains, the evolution of this lineament and its role on the Tyrrhenian opening process is still being debated and much is yet unpublished. A number of authors have developed different hypotheses concerning this area (Savelli and Wezel, 1979; Lavecchia, 1988; Boccaletti et al., 1990; Patacca et al., 1990; Serri et al., 1990; Spadini and Wezel, 1994; Rosembaum and Lister, 2004). Lavecchia (1990) and Boccaletti et al., (1990) interpreted the 41^{st} parallel as a E-W left lateral mega-shear zone induced by asymmetrical extension of the Tyrrhenian Sea. Spadini and Wezel (1994) instead connected the magnetic and free-air gravity lineament of the 41^{st} parallel with the opening of Tyrrhenian basin and with Quaternary inversion tectonics due to intraplate compression. Favali et al.(1993a,b)connected the presumed discontinuity of the Central Tyrrhenian Sea at the E-W Fault system of the Tremiti archipelago considering a common complex deformation belt which has involved the Adriatic Sea, the Latium-Abruzzi Platform and Central Tyrrhenian Sea. Other authors have interpreted the 41^{st} parallel as a lithospheric discontinuity. Patacca et al. (1990) highlighted that the 41^{st} parallel di-

vides two areas with different lithospheric retreats and therefore this alignment must be considered a major lithospheric discontinuity. Serri (1990) also considered this discontinuity of a lithospheric nature dividing two distinct mantle domains in which above the 41^{st} parallel the magma sources are derived from upper crustal rocks or anatectic melts while in the southern Tyrrhenian area the genesis of the magma is dominated by MORB/OIB sources and locally by a transitional MORB/OIB-type mantle wedge. Serri asserts *This magmatism requires two separate, compositionally different subducted slabs: 1) an old oceanic lithosphere in the southern Tyrrhenian sea; 2) a continental lithosphere active in the northwestern portion.* A more recent examination of the Tyrrhenian opening process by Rosembaum and Lister (2004) suggests that the roll back of the Ionian slab is constrained by two major discontinuities, the 41^{st} parallel in the north and the North Sicily Fault in the south. They maintain that the shape of the southern Tyrrhenian basin and the rate of extension is dominated by the presence of the 41^{st} parallel zone.

Although the 41^{st} parallel is correlated to the opening of the Tyrrhenian Sea, its deep crustal setting is not known. An assessment of the magnetic character of the alignment and its surrounding areas such as the Selli Line and Magnaghi-Vavilov basins will provide further insight into its crustal features. This study examines the geometric relationships between the magnetic sources and the tectonic structure of the central-southern Tyrrhenian sea, thus unveiling the nature of the 41^{st} parallel zone.

2 The isostatic setting of the Tyrrhenian Sea - 41^{st} parallel zone

In this chapter the isostatic setting of the Tyrrhenian Sea is evaluated through analysis of free-air gravity satellite data. The gravity features of the Tyrrhenian sea and its isostatic compensation setting were extracted by study and processing of the larger free-air gravity satellite data set of the Mediterranean Sea region. Satellite data obtained from Geosat and ERS-1 missions were used to compile a Bouguer gravity map of the Tyrrhenian Sea, after which a complete Bouguer correction was performed using Parker's method (1972) as a tool enabling an exact evaluation of the gravity contribution from a topographic model of the land. The optimal Bouguer density value for the reduction of the free-gravity data was estimated by two methods: study of the data-set's power spectral density and, secondly, analysis of the correlation between the topography and the Bouguer anomaly by spatial cross plots. Both these methods give the same optimal density of 2350 kg/m^3. Having compiled the Bouguer anomaly map, I then studied the isostatic setting of the Tyrrhenian Sea and drew up a probability map of the Tyrrhenian area where the isostatic effect is believed to play a dominant role. This approach indicates that the Tyrrhenian area is divided by the 41^{st} parallel zone into two domains with different isostatic settings in that the area above the 41^{st} parallel shows an isostatic compensation whereas the southern portion shows an incomplete isostatic equilibrium.

2.1 Introduction

Geophysical observations from satellite data are of major significance when studying large-scale areas of the Earth's surface such as the Mediterranean Sea, which contains in turn the geological sub-domains of the Provencal-Balearic basin and the Tyrrhenian Sea. A large-scale geophysical study of the Mediterranean Sea provides valuable information for the analysis of the geological features of its sub-

regions. Previous literature concerning the Mediterranean Sea consists of a single work, Makris et al. (1998), compiled from ship-borne data acquired between 1965 and 1972, by the Italian Osservatorio Geofisico Sperimentale (OGS) and on-shore data from the Department of Geodesy and Geophysics of Cambridge University gathered in 1973 and 1974 and plotted on the basis of the 1967 normal gravity formula and a standard Bouguer density value of 2670 kg/m^3.

Our new Bouguer anomaly map of the Tyrrhenian Sea was compiled departing from the significant volume of the new free-air gravity satellite data of the Mediterranean Sea. For this purpose only the sub-dataset of the Tyrrhenian Sea was used in order to compile a complete Bouguer reduction using a detail bathymetric dataset of the region being studied. The data referred to was provided by the U.S. Navy, U.S. Department of Defence Naval Oceanographic Office web site [1] and was gridded at 1 minute cell for the Mediterranean Sea, including the Black Sea and Adriatic Sea.

The free-air gravity dataset of the Mediterranean area instead was downloaded from the web site of the Geological Data Center - Scripps Institution of Oceanography - California [2]. This data came from the GEOSAT and ERS-1 missions (Sandwell and Smith, 1997), with a sampling period of 1 minute. The advantages of satellite gravity data, in particular in the wavelength range $\geq$ 24 km, have been well documented by Fairhead and Odegar (2002), confirming that they are in good agreement with the spectral resolution of the bathymetric data. Figures 2.1 and 2.2 show the morpho-topographical setting and the free-air gravity anomalies of the Tyrrhenian Sea, respectively. Since the anomalies of on-shore areas can not be evaluated from satellite data, the gravimetric study is limited to the marine areas only.

The Bouguer reduction was performed after a necessary interpolation of the gravity and bathymetric data into a common grid with a resolution of 2 minutes by using cubic splines. The free-air gravity satellite data belongs to an area extending

[1] $http://www.mel.avo.navy.mil/data/DBDBV/dbdbv\_def.html$
[2] $http://topex.ucsd.edu/WWW\_html/mar\_grav/html$

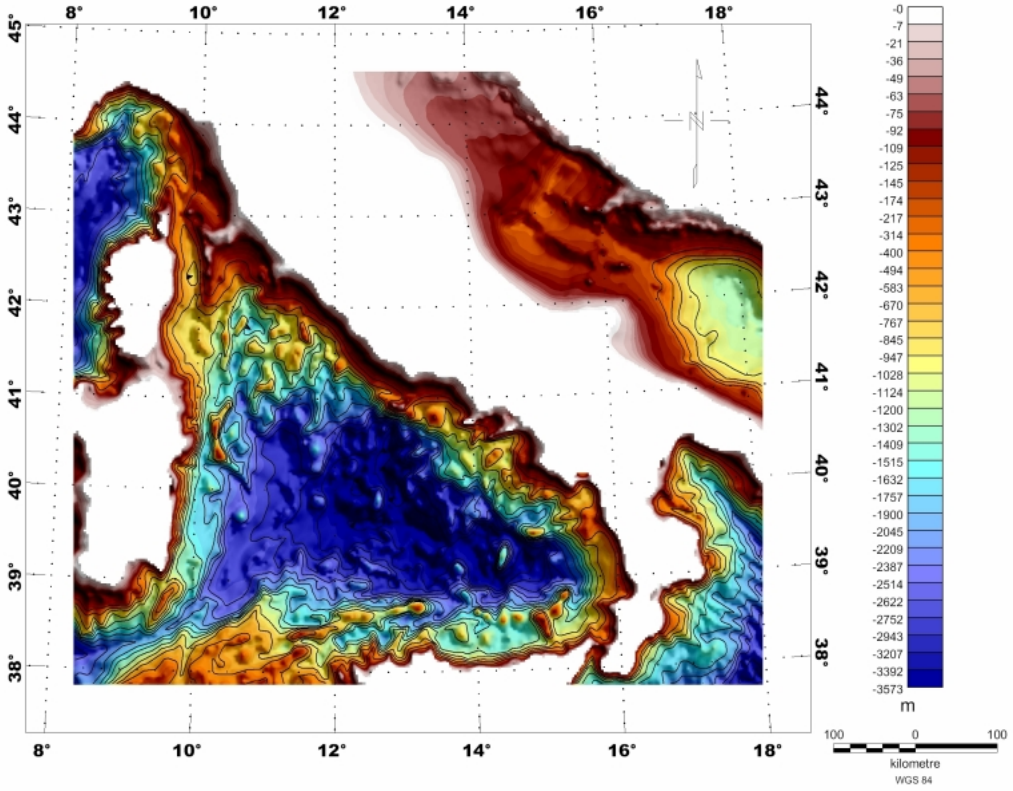

Figure 2.1: Morpho-Bathymetry map of the Tyrrhenian Sea

from 38°N to 45°N in Latitude and from 8°to 18°in Longitude. For evaluating the intrinsic features of this data I applied two Bouguer density optimization methods, obtaining a value of 2350 kg/m^3, the same reduction density as that used to compile the CNR 1992 map of the Bouguer Anomaly of Italy and its surrounding seas based on average surface density and statistical observation. The optimal Bouguer density is identified as an extreme point that minimizes some quadratic function built from gravity data, diverging symmetrically from this minimum, independently of its sign. Subsequently, the area of interest is narrowed to the isostatic setting of the Tyrrhenian region with several considerations on the two Tyrrhenian sub-domains divided by the 41^{st} parallel zone.

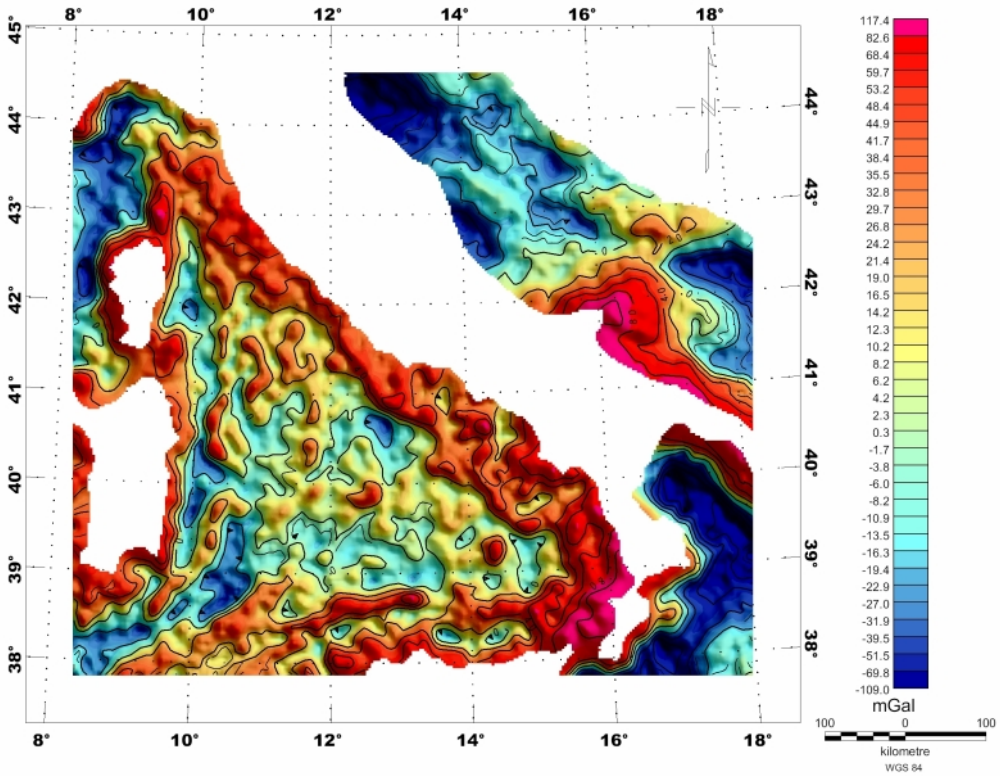

Figure 2.2: Free-Air anomaly map of the Tyrrhenian Sea

2.2 Evaluation of the optimal Bouguer density

The evaluation of the complete Bouguer anomaly was based on the topographic correction alone, departing from the free-air gravimetric anomaly. A complete Bouguer correction requires a method capable of running a detailed Digital Elevation Model (DEM) of the area under observation, without splitting the procedure into simple slab correction and then applying the terrain corrections. In a large area such as the Tyrrhenian Sea, it is preferable to use an analytic procedure able to evaluate the exact topographic contribution in each point of the data-grid, in terms of both processing times and automatization of the procedure. Our procedure of choice was Parker's method (1972), as being particularly suitable for large areas for two reasons: it acts in the Fourier domain, where most data processing is usually

performed, and it converges rapidly on condition that the vertical origin is chosen at an average topographic level (Parker, 1977). The Bouguer correction is calculated with the following equation:

$$\Delta G(k) = 2\pi\gamma e^{|k|z_0} \sum_{n=1}^{N} \frac{(-|k|)^{n-1}}{n!} \mathcal{F}[\rho\left(Z_t\left(r\right)^n - Z_b\left(r\right)^n\right)], \tag{2.1}$$

where

- $\Delta G(K)$is the anomaly generated by a density contrast $\rho(r)$ in the Fourier domain;
- k is the wave-vector with spatial frequencies k_x and k_y; $|k| = \sqrt{k_x^2 + k_y^2}$
- Z_0 is the data observation level
- $\gamma = 6.673$ x $10^{-11} m^3 kg^{-1} s^{-2}$ is the Newton gravitational constant
- $Z_t(r)$ is the sea level, rescaled in proportion to the average depth Z_{av}
- $Z_b(r)$ is the bathymetric level, rescaled in proportion to the average depth Z_{av}
- ρ is the Bouguer density value used for the reduction
- $\mathcal{F}$ indicates the 2D Fourier operator
- n is the expansion order, our analysis was stopped for $N = 5$

In marine areas the Bouguer density value is calculated as the difference between the seawater density ($\rho_w = 1030 kg/m^3$) and the ideal Bouguer density value (target of the optimization method):

$$\rho = \rho_b - \rho_w \tag{2.2}$$

In practical terms the measured topographic effect of the water is replaced with a slab of thickness given by the bathymetric depth characterized by the same density as

the lower crust. The Bouguer gravity G_b is thus obtained from the free-air anomaly G_{fa} as follows:

$$G_b(r) = F^{-1}[G_{fa}(k) - \Delta G(k)], \tag{2.3}$$

which is the Fourier co-transformation of the anomaly. The entire Bouguer reduction is subjected to the chosen reduction density ρ_b. The most universally accepted common value is $\rho_b = 2600Kg/m^3$ which represents the average density obtained with different geological models (Hayford and Bowie, 1912). In particular, as shown by Hinze (2003), the density of $\rho_b = 2670Kg/m^3$ is strongly correlated to the rheologic feature of the crystalline crustal portion with a granitic composition. It is clear that the density value is not correlated to the several and different lithologies of the upper crust portions and in this context the value $\rho_b = 2670Kg/m^3$ is considered a reasonable compromise for the gravity models of the lower and middle crust. The Bouguer anomalies are affected by a strong topographic contamination, which is probably stronger in the case of the continental data sets. The Bouguer-Topography correlation has been studied by several authors: Thorarinsson and Magnusson (1990) and later Chapin (1996) introduced the concept of scaling analysis to reduce the short-wavelength correlation between topography and Bouguer anomaly. Their conclusions on minimizing this correlation followed on from the pioneering work of Nettleton (1939), whose conclusions however did not take into account the large-wavelength inverse correlation effects typical of an isostasy process. Since these two methodologies are however based on the same concept, i.e the reduction of the short-wavelength effects of topography into a gravity dataset, both are useful for the study of the optimal Bouguer density. It is interesting to note that application of both approaches to a large dataset of the Mediterranean Sea produced the same results.

2.2.1 The fractal analysis

The topographic surfaces show chaotic behaviour which is well explained in terms of scaling noise (Mandelbrot, 1967), a term by which the topography is assumed to be scale-invariant, i.e self-affining in different spatial cases. Generally, the scaling features of a particular phenomenon can be evaluated by a study of power spectrum density (in logarithmic scale). Fractal behaviour of the particular phenomenon is highlighted by a linear trend of the power spectrum. The energy of signal decay to the various wavelength with a power-law that is connected to the fractal dimension of the phenomenon. The dimension (D) of a scaling surface can be evaluated by studying the radial power spectrum (azimuthal average calculated over the 2D renumber phase) with the equation:

$$D = \frac{9 + \beta}{2}, \tag{2.4}$$

where β is the slope of the linear trend that fits the decay of the radial spectrum. Figure 2.3 shows the linear behaviour of the radial power spectrum of Mediterranean topography, in which the fractal dimension is $D = 2.77 \pm 0.06$.

The potential field data also shows scaling behaviour as demonstrated by previous works (Gregotski et al., 1991; Pilkington and Todoeschuck, 1993; Maus and Dimri, 1994). The fact that the Bouguer reduction is strongly affected by topography can be observed in the Bouguer anomaly field where the shape of the anomaly is the same as that of the topographic trend. Such similarity is the key to isostasy for the large-wavelength anomalies characterized by negative correlation: a good Bouguer reduction does not show any correlation to topography. The key factor that controls this behaviour is the Bouguer density and an ideal Bouguer density should reduce the positive correlation only for the high-frequency anomalies. Departing from this principle Thorarinsson and Magnusson (1990) evaluated a procedure that minimized the roughness of the Bouguer anomaly surface by varying the reduction density. During a study into the gravity field of two regions of Iceland, the authors

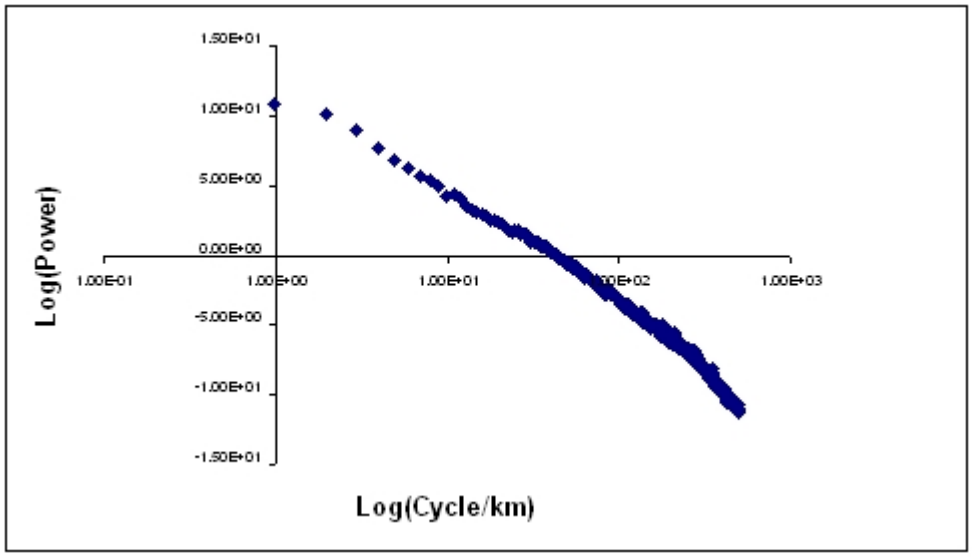

Figure 2.3: Radial power spectrum of the topography data for the Tyrrhenian dataset, Log/Log scale

evaluated the fractal dimension with a variogram analysis of the gravity surface obtaining an average density different from $2670 Kg/m^3$ which was then minimized by the reduction of the short-wavelength effects of topography. Subsequently, Chapin (1996) investigated Bouguer density based on the fractal dimension given by radial power spectrum in the Fourier dimension in a study in which he evaluated a simple Bouguer correction (slab-correction), while neglecting the terrain correction. In this work Chapin evaluated the difference between the linear decay of the fractal dimension with density and the trend observed without minimization. Thorarinsson and Magnusson (1990) had previously studied the fractal behaviour of density and produced a U-shaped curve of the fractal trend. The different results of these two works are due to the terrain correction, in that the topography contribution shows a strongly scaling contamination which affects the high-frequency gravity field. In this sense, an analysis of the scaling exponent vs the Bouguer density reduction may be obtained through a prior complete Bouguer correction. For the Tyrrhenian Sea the complete Bouguer correction is obtained by a DEM of the topography with the Parker equation, and in this case the scaling analysis vs different Bouguer

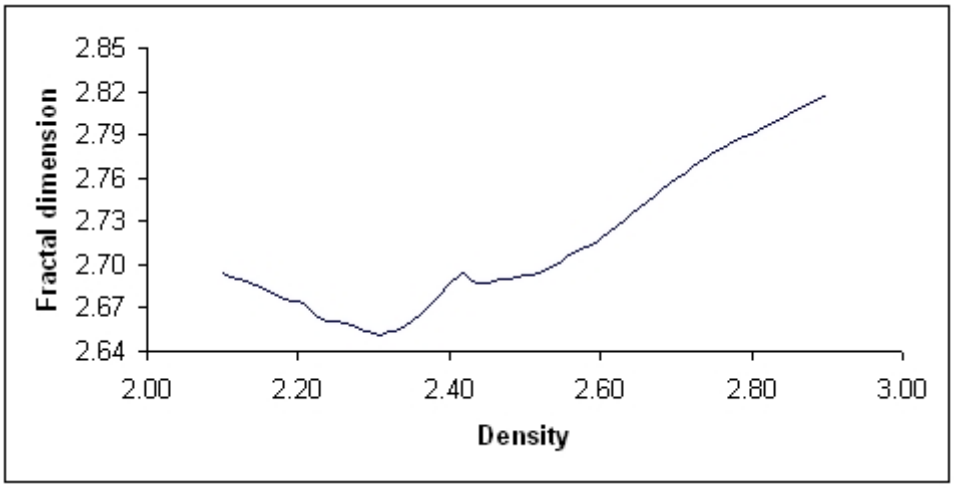

Figure 2.4: Minimization of the fractal dimension at various reduction densities, minimum centered at $2350kg/m^3$

density shows a parabolic trend with a minimum centered to a density value of $2350kg/m^3$(fig. 2.4).

The above result is obtained by an analysis of a range of wavelengths between 45 and 105 km where the Radial Power spectrum trend is linear and stable. This wavelength band is connected to an intermediate depth source less influenced by crustal-mantle discontinuity. In the large-wavelength part, the horizontal trend of the radial power spectrum is associated with non-scaling features as if due to isostatic compensation.

2.2.2 Bouguer-Bathymetry correlation

Since the topography effect can be observed as a scaling contamination of the gravity field mainly in the short-wavelength band, it can be reduced by using the cross-plots of the Bouguer anomaly vs the topography at differing densities.

In the hypothesis of a perfectly rigid crustal support, this correlation would appear stochastic with a null slope. The contribution of isostasy to the gravity data is highlighted by a negative correlation with topography, an effect which is more evident in the large-wavelength bands. Figure 2.5 shows the topography vs Bouguer

cross-plots calculated at various densities and after a high-pass filter $\lambda < 125km$. The cross-plots highlight two distinct groups of data: a first cloud of data (A) that shows a negative correlation presumably associated with an isostatic compensation mechanism, while the second cloud (B) shows a horizontal trend.

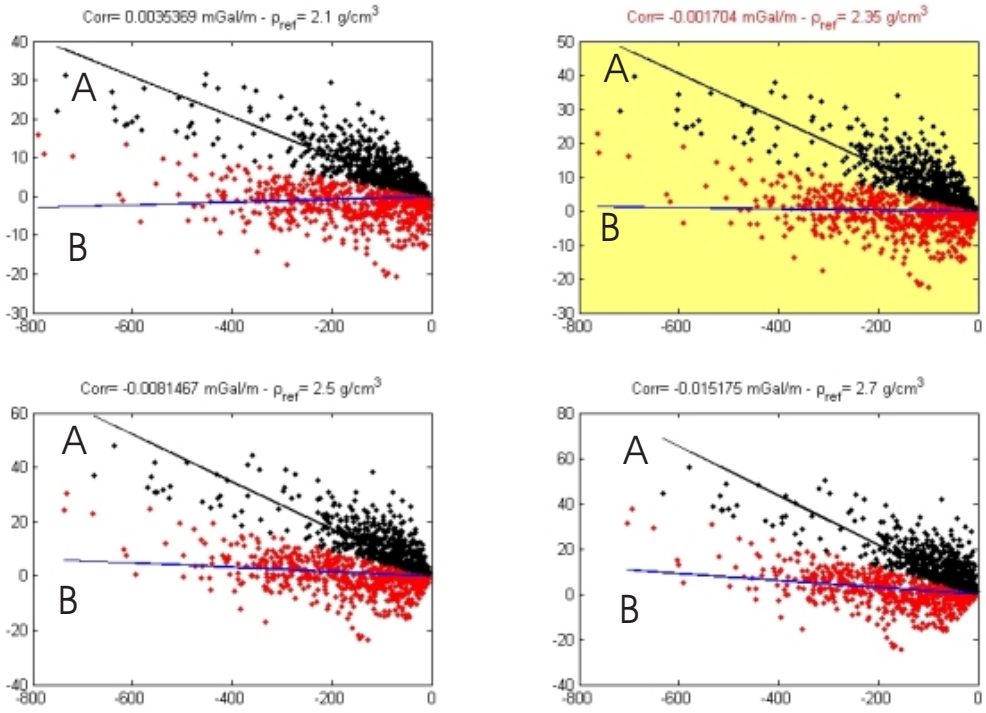

Figure 2.5: Cross-plot of the correlation between Bouguer anomaly and the bathymetry for various reduction densities. Two least squares fits have been performed, the optimal value is $2350kg/m^3$ (plot with red points)

This leads us to conclude that if the correlation with topography is to be reduced, it pertains only to the significant data sub-set B. A minimization of the correlation would produce an under-estimation of the optimal Bouguer density with a flattening of the large-wavelength gravity anomalies, an approach usually employed when studying small regions believed to be crustal supported, and whose result is usually different from the value of the Bouguer density obtained with the scaling approach (Thorarinsson and Magnusson, 1990). This problem may be solved with

a simultaneous least-squares fit of the data by using two linear trends. The linear relationship for the correlation Bathymetry vs Bouguer is:

$$y = mx, \tag{2.5}$$

where y is the Bouguer anomaly, x is the bathymetry value and m is the slope of the cross-plot, which if ideally uncorrelated should be null. For different Bouguer density values the slope of the cross-plot changes with varying $m = m_A$ if the euclidean distance of the point (x,y) from the linear trend A is lower than the distance from the linear trend B; and $m = m_B$ otherwise. By a iterative procedure m_A and m_B values are re-calculated for each iteration, so that the final result is the best estimate of both coefficients. During the simultaneous fit, for each iteractive phase, the errors of fitting between the real data and the fitting line are calculated. The process is interrupted when the misfit-error is smaller than a pre-fixed tollerance (defined by the user). The table 2.1 give the standard deviation values for the four least-squares fitting processes of the dataset B of figure 2.5.

In the case in question, the horizontal distribution for the B-cloud (null slope) was obtained when the optimal Bouguer density value was $2350 kg/m^3$, a value in good agreement with the density value obtained using the scaling approach. Both the methodologies give the same value of optimal Bouguer density, being based on the same principle of minimizing the short-wavelength topographic effect on the gravity data. In the cross-plots analysis I isolated a sub-set of Bouguer data that shows a strong negative correlation with the topography and which is correlated with a large isostatic mechanism. An evaluation of the spatial distribution of this dataset may be of relevance for a regional study of the isostatic setting of the Tyrrhenian Sea.

2.3 Discussion of the results

The scaling approach and the cross-plot analysis highlighted a particular value

Iteration n.	density 2200	density 2400	density 2600	density 2600
1	6.9726	7.7911	8.4672	8.5734
2	6.6968	7.3909	7.7106	8.0888
3	6.2053	6.6671	7.2134	7.6112
4	5.7104	6.2519	6.7947	7.403
5	5.3543	6.0308	6.6264	7.224
6	5.1909	5.8657	6.4769	7.0817
7	5.0595	5.7068	6.3572	6.8487
8	4.7689	5.3742	5.9564	6.5052
9	4.7254	5.3399	5.9371	6.4881
10	4.7213	5.3003	5.8845	6.4471
11	4.7213	5.3003	5.8735	6.4345
12	4.7213	5.3003	5.8735	6.4345

Table 1: List of standard deviation values during the fitting process for the dataset B

of optimal density for the Bouguer reduction of the Tyrrhenian gravimetric dataset. Departing from this information, a revised Bouguer gravity map was plotted using a density of $\rho_b = 2350 km/m^3$ and for which the Bouguer anomalies were low-pass filtered using a cut-off wavelength obtained through power spectrum density: see figure 2.6. While the resulting map provides useful information on the regional variation of the gravity field, it is unable to throw light on the isostatic setting of the Tyrrhenian area.

This map shows a large positive anomaly centered in the South Tyrrhenian basin, in which the amplitude of the anomaly signal decreases from the Southern portion of the basin down to negative values in the zone above the 41^{st} parallel. The shape of the positive anomaly (see contour distribution) in the southern Tyrrhenian portion agrees with the shape of the basin. Around the 41^{st} parallel lies the zero-level of the anomalies, and this level shows a E-W trend like the crustal structures located over the 41^{st} parallel. Northward of this line, the Bouguer anomalies show a negative trend with local positives centered on structural highs of the Northern Tyrrhenian basin. These differences confirm the N-S variation of the crustal-lithosphere system

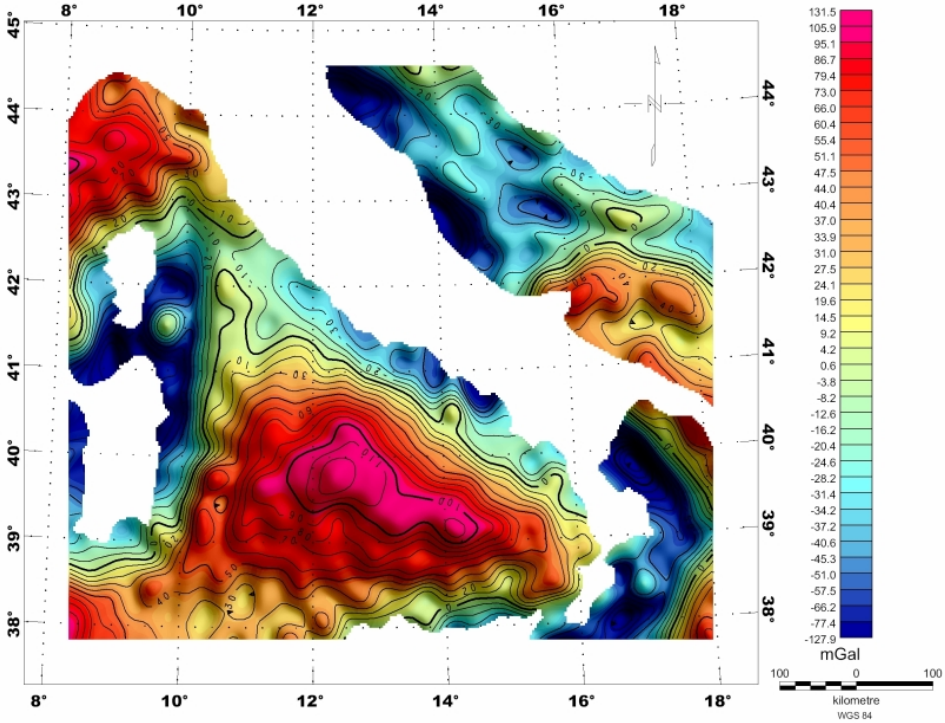

Figure 2.6: Bouguer anomaly map of the Tyrrhenian Sea obtained using the optimal reduction density of $2350 kg/m^3$

of the Tyrrhenian, since the variations in the Bouguer anomaly field can be correlated with a considerable difference in crustal rheologic behaviour between the southern and northern portions. A further profile of the deep crustal setting of an area is obtained by evaluation of the isostatic residual anomaly (Simpson et al., 1986), for example using the method of Karner and Watts (1983). Applying this approach to the Tyrrhenian area, the crustal features may be evaluated by plotting an isostatic setting map. The previous cross-plot analysis highlighted two distinct data sub-sets related to a different correlation between topography vs Bouguer. The first group of data, called A, is believed to derive from regions where the isostatic mechanism is still active, and spatial distribution of this data may be useful for a computation of the isostatic pattern of this region. The actual data distribution was done with a box-counting method in which the Tyrrhenian region was divided into a set of smaller

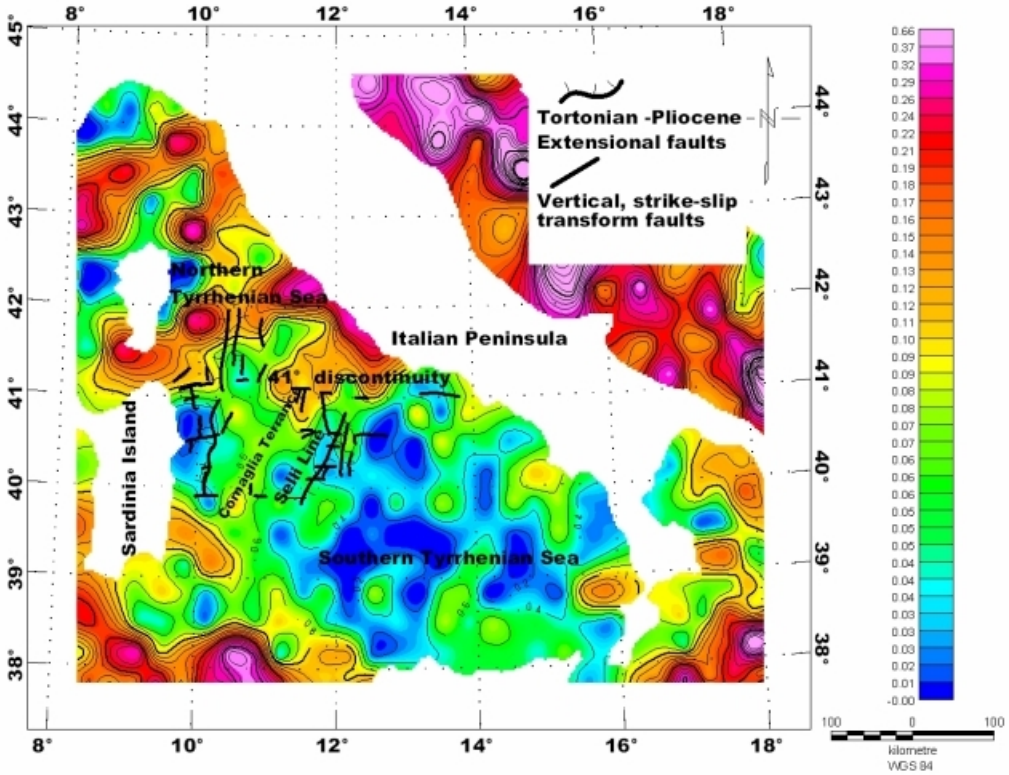

Figure 2.7: Map of the isostatic level of the Tyrrhenian Sea as obtained by the box-counting method applied to the data where isostatic effects are supposed to be active. The counting has been rescaled into an arbitrary range between 0 (minimum probability of isostatic mechanism)and 1 (maximum probability of isostatic mechanism)

boxes. Using an interactive procedure we calculated the number of points on dataset A that fall within each box, and subsequently normalized the total number to a range between 0 and 1 to give a better representation of the isostatic setting. The map in figure 2.7 shows the spatial distribution of this parameter for the Tyrrhenian Sea area, thus giving more information on the deep setting of the Tyrrhenian sea, and on the role of the 41^{st} parallel zone as the boundary between two distinct crustal-lithosphere domains.

The Tyrrhenian region presents low isostatic level values. The low isostatic levels of the Southern portion would confirm that the isostasy is still active, and this behaviour is dominant in the deep basin areas such as Magnaghi-Vavilov and

Marsili. In the Northern Tyrrhenian area instead, northward of the 41^{st} parallel zone the isostatic level are higher (0.25-0.55), which supports the theory that there is also an isostatic division between the two Tyrrhenian domains: the northern portion, where the compensation mechanism is ended, and the southern part in which the isostasy process is evident. The boundary between these two domains shows a E-W trend along the 41^{st} parallel zone, although in the western area the changing point of the isostatic level turns NE-SW in the same direction as the structural element of the Selli Line, a fact which may indicate that these structural lineaments bond two deep lithospheric domains. A further consideration lies in the fact that the Northern Tyrrhenian basin is the older portion where the continental crust is less thinned. In this portion, the process of eastward migration of the subduction system occurred during the Late Oligocene at a low velocity rate (1.5-2 cm/yr) (Facenna et al., 1997). This migration ended in the middle Miocene on the Corsica margin and in the Early Pliocene on the Apennines sector. The Southern Tyrrhenian, on the other hand, is a relative young back-arc basin characterized by several episodes of extensional tectonics and volcanism associated with a SE flexural migration of the subduction system (Royden, 1988; Malinverno and Ryan, 1986) suggesting a thin crustal thickness. These features are confirmed by maximum heat flow values (Della Vedova et al., 2001) and a shallow Moho depth of approx 10 km (Sartori et al., 2004). The isostatic level map would appear to confirm the existence of an up-welling mantle at the base of the crust as suggested by Hoernle et al. (1995), on the grounds that the source of this low isostatic level is the upper part of the mantle (Seber et al., 2001). The incomplete isostatic compensation of the Southern Tyrrhenian Sea is confirmed by a dense distribution of the hypocenters of deep seismicity located around the Aeolian arc and the abyssal basin where volcanic activity still occurs (Vannucci et al., 2004) suggesting a non-equilibrium of the crust-mantle interface.

3 The geomagnetic field

This chapter deals with the peculiarities of the geomagnetic field and its representation, with particular attention to the mathematical notation of the field to better understand and interpret its spatial variations. The time-dependence of the magnetic field is studied departing from its raw measurement and go on to calculate the magnetic anomaly field as the subtraction between the reference field and the real data. Since the anomalous contributions strongly related to the structural setting of the upper-middle crust, accurate evaluation of the shape and magnitude of the anomalies can provide important information on the nature of the sources.

3.1 Representation of the geomagnetic field

At any point of the Earth's surface, the geomagnetic field can be described by a total intensity vector **F**, the magnitude of which is usually expressed in nT (SI-10^-5 gauss). In literature it is commonly accepted that the geomagnetic field consists of three parts: the main field, external field and variations of the main field, where interestingly the external field represents only 1% of the total intensity. This component originates outside the earth and appears to be associated with electric currents in the ionized layer of the outer atmosphere. In a first approximation the geomagnetic field can be derived from a geocentric dipole with a magnetization of $8\text{x}10^{22} Am^2$ inclined approx 11°from the Earth's rotational axis (Telford, 1990). The magnitude value of **F** varies from 30000 nT in the equatorial zone to 65000 nT in the polar areas. The total intensity vector (**F**) can be decomposed into two components **H** and **Z**, which represent the projections of **F** on the horizontal and vertical planes respectively. The angle between the direction of the geographic north and **H** is called declination **D**, whereas inclination **I** is the angle between F and H (fig. 3.1). The relationship between these elements is the following:

$$F^2 = H^2 + Z^2 = H^2 + Y^2 + Z^2 \tag{3.1}$$

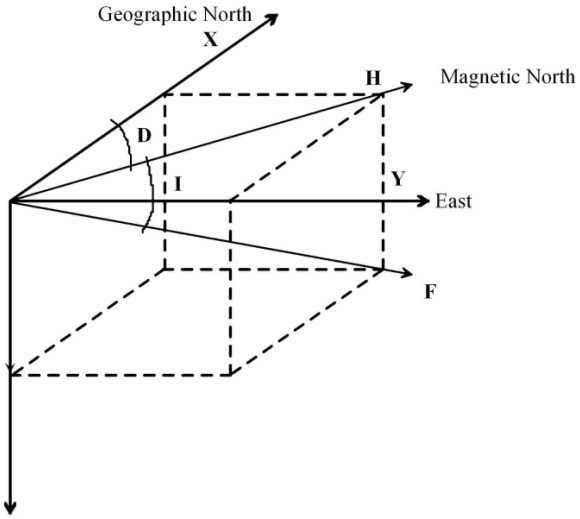

Figure 3.1: Components of the Earth's magnetic field

$$H = FcosI \qquad Z = FsinI \qquad tanI = \frac{Z}{H} \tag{3.2}$$

$$X = HcosD \qquad Y = HsinD \qquad tanD = \frac{Y}{X} \tag{3.3}$$

As illustrated in figure 3.1 the Z-vertical component of F is positive downwards, H is always positive, while X and Y are considered positive Northward and Eastward. In this reference frame, when the F-vector dips downwards in northern latitudes it is called positive pole, whereas in the southern hemisphere it is referred to as the negative pole.

A first mathematical representation of the geomagnetic field was created in the early 1800's by Gauss using a spherical harmonic analysis. The analytic form of the field departs from one of Maxwell's equations.

In a space without discontinuities, magnetic induction has no divergence and the related field ($\mathbf{b}$) is conservative:

$$\boldsymbol{\nabla} \cdot \mathbf{b} = 0, \tag{3.4}$$

the field can be also derived from a potential ϕ:

$$\mathbf{b} = -\boldsymbol{\nabla} \cdot \phi. \tag{3.5}$$

The potential ϕ satisfies the Laplace equation:

$$\nabla^2 \phi = 0, \tag{3.6}$$

where ∇^2 is the Laplacian operator. The solution of this equation can be calculated in a spherical coordinates system with the origin located in the center of the Earth.

$$\nabla^2 \phi = \frac{1}{r^2}\frac{\partial}{\partial r}\left(r^2 \frac{\partial \phi}{\partial r}\right) + \frac{1}{r^2 \sin\theta}\frac{\partial}{\partial \theta}\left(\sin\theta \frac{\partial \phi}{\partial \theta}\right) + \frac{1}{r^2 \sin^2\theta}\frac{\partial^2 \phi}{\partial \lambda^2} = 0, \tag{3.7}$$

θ= co-latitude, λ=longitude; r=radius. the potential ϕ is given by :

$$\begin{aligned} \phi = a \cdot \sum_{n=1}^{\infty}\sum_{m=0}^{n} \Bigg[\left(\frac{r}{a}\right)^n \cdot \left[(g_n)^{m_{ext}} \cos m\lambda + (h_n)^{m_{ext}} \sin m\lambda\right] \\ + \left(\frac{a}{r}\right)^{n+1} \cdot \left[(g_n)^{m_{int}} \cos m\lambda + (h_n)^{m_{int}} \sin m\lambda\right] \Bigg] \cdot \left(P(\theta)_n\right)^m , \end{aligned} \tag{3.8}$$

where a is the Earth's radius , r is the distance of a generic point from the center, n and m are positive numbers with $m \leq n$ called degree and order of the Schmidt Polynomius $P_n^m(\theta)$. Laplace's equation 3.8 contains two contributions to the geomagnetic field: the external components of the Earth and the internal contribution to volume. In equation 3.8 these two components are represented by the Gauss coefficients $g_n^{m_{ext/int}}$, $h_n^{m_{ext/int}}$. The internal contribution is generated by a deep field linked to a geodynamo mechanism and by a crustal field generated by the high magnetized rocks of the crust. The external field is a small portion of the main geomagnetic field (1%), thus its components may be assumed as negligible. Equation 3.8 may be re-written for the internal contribution as follows:

$$\phi = a \cdot \sum_{n=1}^{\infty}\sum_{m=0}^{n} \left(\frac{a}{r}\right)^{n+1} P_n^m(\theta)\left(g_n^m \cos m\lambda + h_n^m \sin m\lambda\right). \tag{3.9}$$

In general, equation 3.9 is truncated at order 10, obtaining the main field connected to the nucleus of the earth. In geomagnetic prospection, the deep magnetic contribution is usually subtracted from the total field for evaluation of the crustal

magnetic sources. The nuclear contribution is obtained with a set of Gauss coefficients abbreviated as IGRF (International Geomagnetic Reference Field), which is periodically calculated by the International Association of Geomagnetism and Aeronomy (IAGA) (Cain et al., 1968; Langel, 1991). The choice of a distinct reference field is dictated by the spatial dimension of the study area. In the case of a regional study the anomaly field should be calculated by subtracting the IGRF, while for smaller areas it can be obtained by removing the local reference field using a local plane, trend or polynomius.

3.2 Time variation of the geomagnetic field

Since the geomagnetic field is affected by spatial and time dependence, interpretation of the anomaly field is based on the connection between anomaly and its local position of the source, hence the time-variation of the geomagnetic field should be eliminated in order to obtain a precise spatial-dependent crustal field. Each time that we measure the geomagnetic field, the data recorded is affected by a time-variation of one of two main groups: internal variations and external variations. The first, known as "secular variation ", is a field fluctuation linked with the Earth's interior phenomena such as the change of the I and D angles of the F-vector. To the external group belongs the short-time variation of the field (less than 10 years) (Telford et al., 1990). A number of effects are listed below:

1. A cycle of 11 years' duration associated with sunspot activity

2. Solar diurnal variation with a period of 24 hours and an intensity of 30-40 nT, varying with latitude and season

3. Lunar diurnal variation with a period of 25 hours and a range of 2-3 nT, this effect being caused by moon-ionosphere interaction

4. Magnetic storms are transient disturbances with a period ranging from a few minutes (bays) to several days. The intensity of these storms can be greater

than 1000 nT at most latitudes and even larger in polar regions, where they are associated with the aurora.

Excluding magnetic storms, in which the amplitude of disturbance is such that magnetic prospecting may be impracticable, the time dependence of the Geomagnetic field can be measured and then subtracted by using a magnetometer known as a base-station located in a fixed position. The base station must be installed near the survey area when the crustal-magnetic signature is low (well away from any magnetic source). This magnetometer samples the field every 0.1-1 sec and records the time-variation of the total intensity field . The magnetic data recorded by the base station is subtracted from the real raw magnetic data to obtain the spatial contribution of the geomagnetic field, thus providing the crustal magnetic contribution of the area studied. Data recorded at different times is interpolated to obtain the same number of observations of the measurement set. In off-shore magnetic surveys, when the effective time variation is unknown, accurate time-reduction may be impeded by unsuitable location of the base-station in that the magnetic observatory is usually installed on the coast near the survey area. Since this type of error is relevant in a high definition magnetic survey, the necessary time-reduction must be resolved by using a differential measurement system (Jones, 1999; Marcotte et al., 1992) or FFT filtering of the F-vector magnitude (Faggioni and Caratori Tontini, 2003). The procedure (called, time-track) is based on an acquisition of the geomagnetic field along the same route at two different times. A marine survey produces a four-channel time data-set [Time (sec), Latitude λ, Longitude ϕ, geomagnetic field amplitude (nT)], vector F is defined as $F = F(t, x, y)$. Alternatively F is acquired from the nearest observatory $F(t)$. By evaluating vector F(λ,ϕ) in the Fourier domain, the time dependence can be eliminated by a subtraction between the F_1 acquired at

time t_1 and the F_2 related to time t_2:

$$FFT1_{(\phi,\lambda)} = FFT1_{(\phi,\lambda,t_1)} - F1_{(t_1)} \tag{3.10}$$

$$FFT2_{(\phi,\lambda)} = FFT2_{(\phi,\lambda,t_2)} - F2_{(t_2)} \tag{3.11}$$

$$\Delta F_{(\lambda,\phi)} = FFT1_{(\phi,\lambda)} - FFT2_{(\phi,\lambda)}, \tag{3.12}$$

where $FFT1_{(\phi,\lambda,t_1)}$,$FFT2_{(\phi,\lambda,t_2)}$ are the geomagnetic fields acquired along the track at times 1 and 2; $F1_{(t_1)}$ and $F2_{(t_2)}$ are the magnetograms at times 1 and 2. This procedure introduces a greater approximation, but ensures time phase control for the geomagnetic signal with a smoothing action to eliminate the higher frequency noise (Faggioni and Caratori Tontini, 2003).

3.3 The magnetic anomaly field

The geomagnetic field is given by a convolution of different contribution such as the internal field, the external variation and the crustal components. The crustal component of the field is evaluated by subtracting the deepest contribution F_{ref} and the time-dependence F_t from the total intensity of the magnetic field of as described by the following equation:

$$\Delta F = F - F_{ref} - F_t. \tag{3.13}$$

Starting from equation 3.13, it is possible to estimate that the magnetic anomaly is caused by the upper portion of the Earth alone, with a spatial dependence. In these terms, magnetization of the crustal rocks represents the main cause of the anomaly field. The magnetic crustal layer is delimited in the lower portion by the Curie isotherm surface, in that the ferromagnetic minerals (Magnetite s.s and s.l) of the basic-ultra basic rocks change their magnetic behaviour over the Curie Point (580°). According to their magnetic properties all materials can be classified into three main groups : diamagnetic, paramagnetic and ferromagnetic.

1. Diamagnetism. A diamagnetic rock has a negative magnetic susceptibility. The intensity of the magnetization induced by the geomagnetic field is in

Rock Type	Susceptibility range	Average Rock Type	Susceptibility range	Average	
sedimentary			**Igneous**		
Dolomite	0-75	10	Granite	0-4000	200
Limestone	2-280	25	Rhyolite	20-3000	
Sandstones	0-1660	30	Dolerite	100-3000	1400
Shale	5-1480	50	Augite	2700-3600	
Metamorphic			Diabase	80-13000	4500
Amphibolite	60	60	Porphyry	20-16700	5000
Schist	25-240	120	Gabbro	80-7200	6000
Gneiss	10-2000		Basalts	20-14500	6000
Serpentine	250-1400		Peridotite	7600-15600	13000
Slate	0-3000	500	Andesite	13500	13500

Table 2: Table of the magnetic susceptibility of various rocks

the opposite direction to the field. The negative charges are oriented in the opposite direction to the induced field. The most common diamagnetic earth materials are graphite, gypsum, marble, quartz and salt (Telford et al., 1990).

2. Paramagnetism. All rock-minerals which are not diamagnetic are paramagnetic. A paramagnetic rock exhibits zero or positive magnetic susceptibility (K positive) where each atom has a net magnetic moment in a zero external field. Paramagnetic elements are Al, Mn, Pt, Th, U, Nb, Ca.

3. Ferromagnetism. A ferromagnetic material has several magnetic domains which may be aligned along and in the opposite direction to the induced field, but the magnetic moment is positive. Ferromagnetic rock has an intrinsic magnetization with a low amplitude: when this rock is placed in an external magnetic field its susceptibility increases. The most common ferromagnetic minerals are Magnetite, Ilmenite and Maghetite.

Tables 1 and 2 below give magnetic susceptibility values for the main types of rocks and minerals.

The magnetic anomalies are generated by a portion of highly-magnetized rocks, called magnetic sources, beneath a lower magnetization layer. The vectorial anoma-

Mineral Type	Susceptibility range	Average	Mineral Type	Susceptibility range	Average
Graphite		-8	Siderite	100-310	
Quartz		-1	Pyrite	4-420	130
Salt		-1	Limonite		240
Gypsum		-1	Hematite	40-3000	550
Calcite	-0.6		Chromite	240-9600	600
Chalcopyrite		32	Pyrrhotite	10^2- 5 x10^5	125000
Ilmenite	2.5 x10^4- 3 x10^5	1.5 x10^5	Magnetite	10^5- 1.6 x 10^6	5 x10^5

Table 3: Table of the magnetic susceptibility of various minerals

lous field F_{an} shows an amplitude smaller than the total field $\mathbf{F}(F_{an} < 10\%F)$ and the same direction as $\mathbf{F}$. The magnetic anomalous field has a dipolar shape and the anomaly shows a positive and a negative lobe. The ratio between the positive and negative lobes is a function of the latitude as a result of the change in inclination $\mathbf{I}$. The rotation of the azimuth formed by the maximum positive and the minimum negative is due to the declination factor. Synthetic anomalies of a set of prismatic cells have been calculated by varying the inclination of the induced field (varying the latitude) (fig 3.2). At equatorial latitudes ($I = 0°$) the anomaly is negative while at our latitude ($I = 55° - 60°$) the anomaly is dipolar with both lobes having the same amplitude. In the polar regions, where vector $\mathbf{F}$ is vertical, the shape of the anomaly is mono-polar. The dipolar behaviour of the magnetic anomaly is a crucial point in the interpretative process. Obviously, the local distribution of an anomaly is not perfectly centered over the source generating it, therefore to obtain a direct relationship between anomaly and generating source it is necessary first of all to change the shape of the anomaly from dipolar to pseudo-polar by calculating the anomaly with a vertical vector of the main as in the polar field. This transformation, called *reduction to the pole*, removes one level of complexity from the interpretative phase because it shifts the anomalies laterally into a position over their respective sources (Gunn, 1975; Blackely, 1995). The Fourier domain form of this transformation is

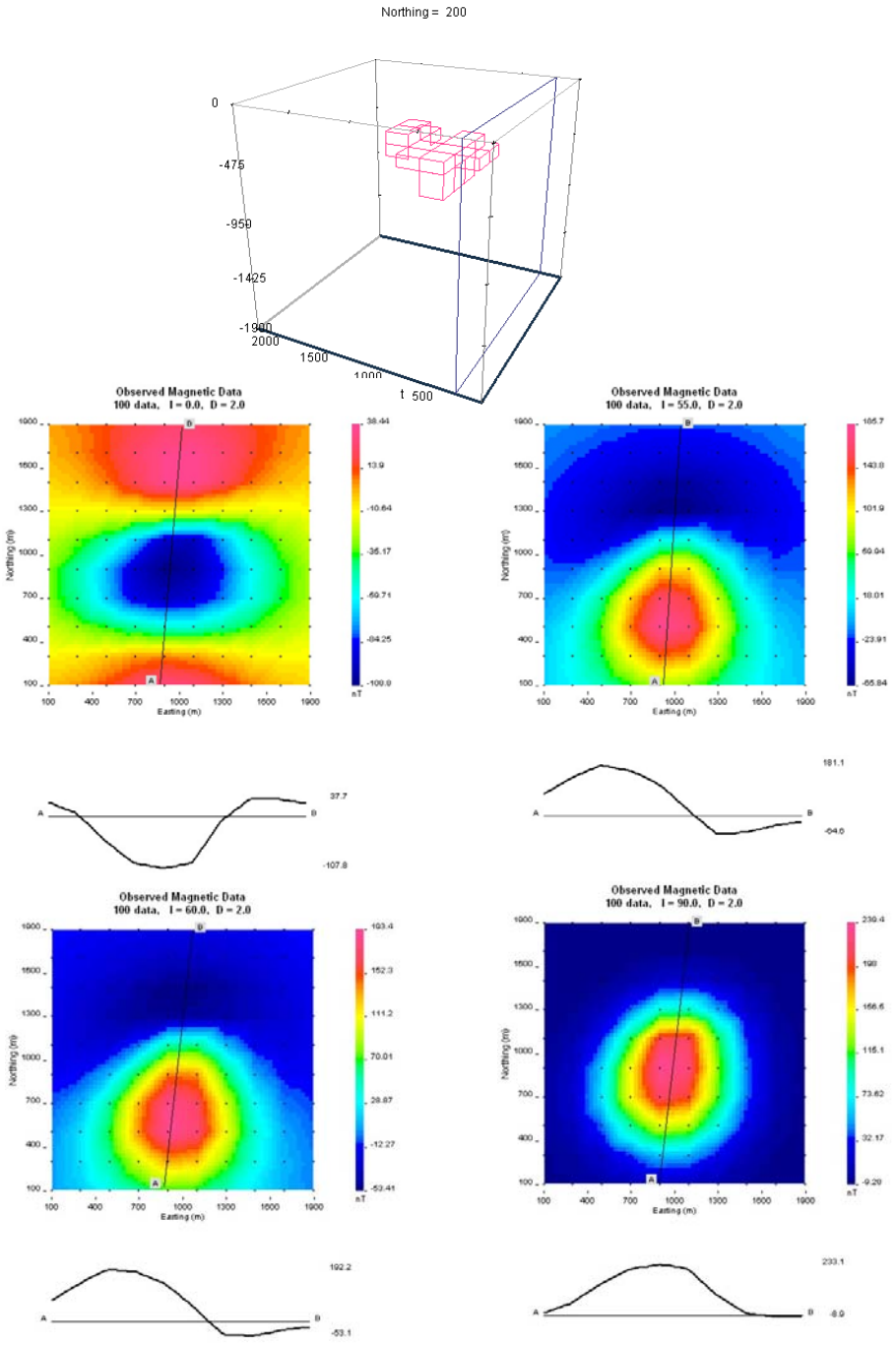

Figure 3.2: Synthetic anomalies calculated at different values of inclination and declination of the geomagnetic field; the generating source is represented by a unique prismatic body

given by

$$R(k_x, k_y) = \frac{k_x^2 + k_y^2}{(i \cos I \cos D k_x + i \cos I \sin D k_y + \sin I \sqrt{k_x^2 + k_y^2})^2}, \tag{3.14}$$

where k_x and k_y are the wave-numbers along X and Y direction, I and D are Inclination and Declination of the induced field, respectively. This procedure is unreliable when applied to low-latitude areas (equatorial zones), since the result of the transformation can appear as a short-wavelength artifact elongated in the direction of the declination. At non-equatorial latitudes, conversely, reduction to the pole represents a valid tool for direct interpretation of the magnetic anomaly field.

4 Description of the magnetic data

This chapter describes the magnetic data of the 41^{st}parallel zone extracted from the larger database of the Italian peninsula and surrounding seas. The phases of acquisition, processing and development of the new Aeromagnetic Anomaly Map of Italy (Caratori Tontini et al., 2004; Eni E &P division) are described in the first portion of this chapter while the later parts deal with the manner in which the raw magnetic data of the Central Tyrrhenian sea was processed by computing its anomaly field and the associated reduction to the pole. As a result this chapter represents the starting point for the entire quantitative analysis of the magnetic features of the 41^{st} parallel zone.

4.1 The Aeromagnetic Anomaly Map of Italy

A new aeromagnetic map of Italy and its surrounding seas was recently plotted by Caratori Tontini et al. (2004). The magnetic dataset used for this map is a sum of the total intensity field data acquired partly by AGIP (Direzione Esplorazione Idrocarburi) between 1971 and 1980 and ENI SpA (Exploration & Production Division) during the years 2001-2002. The previous magnetic cartography of Italy consisted of the aeromagnetic map compiled by AGIP and SGN (1994) and the shaded relief magnetic map at sea level by Chiappini et al. (2000) obtained by using the marine dataset acquired by OGS (Osservatorio Geofisico Sperimentale-Trieste Italy), combined with the on-land dataset of the repeat station network (Caratori Tontini et al., 2004). The old Agip aeromagnetic map was produced for specific industrial-mining use and the raw data was processed using particular methods such as the choice of the geomagnetic reference field. The result of this approach was an anomaly map affected by a linear trend aligned NNW-SSE with an average amplitude of 0.5 nT/Km, a particular effect which may represent an obstacle to structural interpretative studies. Having been developed instead for scientific purposes, the new aeromagnetic map of Italy is a precious tool for a structural/geologic study of the

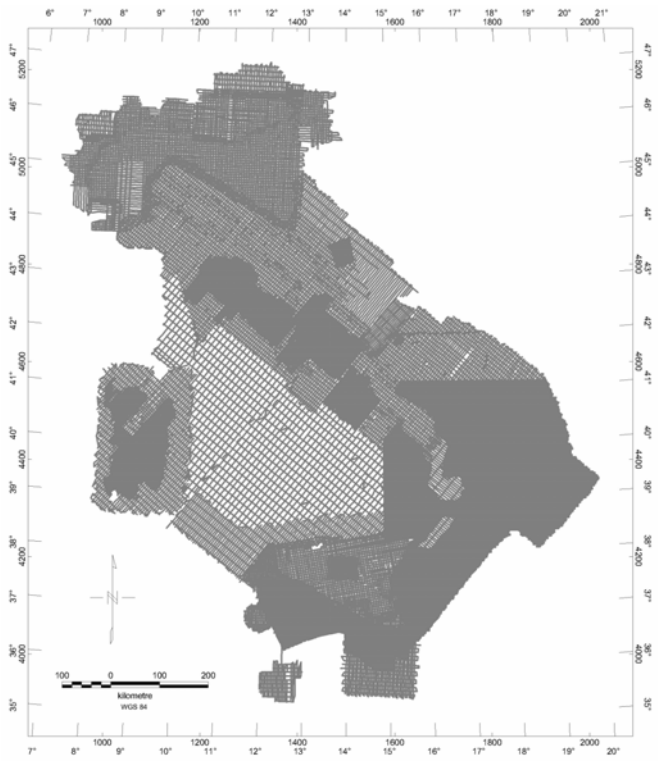

Figure 4.1: Lay-out of the 41 aeromagnetic surveys

Italian peninsula.

The magnetic dataset of the 2004 map consists of 36 databases derived from a number of micro-surveys carried out by Agip during the years 1971-80, combined with five new surveys done in 2001-2002 by Eni and the Consorzio Universitario della Spezia covering the Ancona off-shore, Molise off-shore, NE Calabria on/off-shore, Sicily on-shore and lastly the off-shore portion of Southern Sicily. Between them the old and new surveys covered a total area of 783576 km^2, albeit using different techniques. The flight planning of the 1971-1980 surveys is characterized by a parallel line spaced every 5-10 km and control tie line every 10-15 km, with variable line-spacing according to the different areas covered, and magnetic field data taken every 0.05-0.25 km. The five 2001-2002 surveys give an average parallel line spacing of 2-5 km and 5-10 km for the tie-line, with a sampling step of 0.05 km. The total 41 surveys were performed with a high-resolution (0.01 nT) optically pumped

cesium magnetometer, and each single survey was time-reduced using a local base-station. The flight altitude varied between 1500 and 4000 meters (4800-13000 feet) passing from the Tyrrhenian sea to the Alpine region. Figure 4.1 shows the 41 survey areas with the tracks of the parallel lines and control tie lines. To obtain the residual aeromagnetic anomaly map the raw-data of each database was re-projected to the geomagnetic epoch using the IGRF-1979 reference field. The magnetic anomaly map was then processed with statistical leveling and micro-leveling to avoid errors of intersection and line path effects. Each reading was projected to the common altitude of 2500 m by using an upward/downward BTM projection in the frequency domain (Faggioni et al., 2001). The BTM procedure uses the vertical gradient of the magnetic signal, differentiated for the frequency bands, to project the signal at the same reference altitude using the following equation:

$$\Delta F_c^{L,H}(\phi,\lambda) = \Delta F^{L,H}(\phi,\lambda) + 0.5 \cdot d(\phi,\lambda) \cdot K^{L,H} \cdot \frac{\Delta F^{L,H}(\phi,\lambda)}{|\Delta F_{max}^{L,H}(\phi,\lambda)|}, \tag{4.1}$$

where ϕ, λ are the geographical coordinates; $\Delta F_c^{L,H}$ is the low/high frequency BTM projected anomaly; $\Delta F^{L,H}(\phi,\lambda)$ is the low/high frequency anomaly; $K^{L,H}$ is the low/high vertical gradient; $|\Delta F_{max}^{L,H}(\phi,\lambda)|$ is the maximum value of the anomaly field. Application of this procedure ensures that the 41 magnetic databases are integrated into a single dataset of the aeromagnetic anomaly map of Italy (Fig. 4.2).

4.2 Magnetic data of the 41^{st} parallel

The 41^{st} parallel covers a large area connecting the Campanian coast with northwest Sardinia. To ensure an accurate description of the magnetic pattern of this East-West-running area, the magnetic analysis is focused on area larger than that directly involved. In practical terms, the area studied is constrained latitudinally between 39°30 and 42°00 and longitudinally from 16°00 to 9°00. The magnetic anomaly map of the Central Tyrrhenian Sea is formed by the integration of seven Italian dataset micro-surveys: Southern Tyrrhenian Sea (n. 80-81), Northern

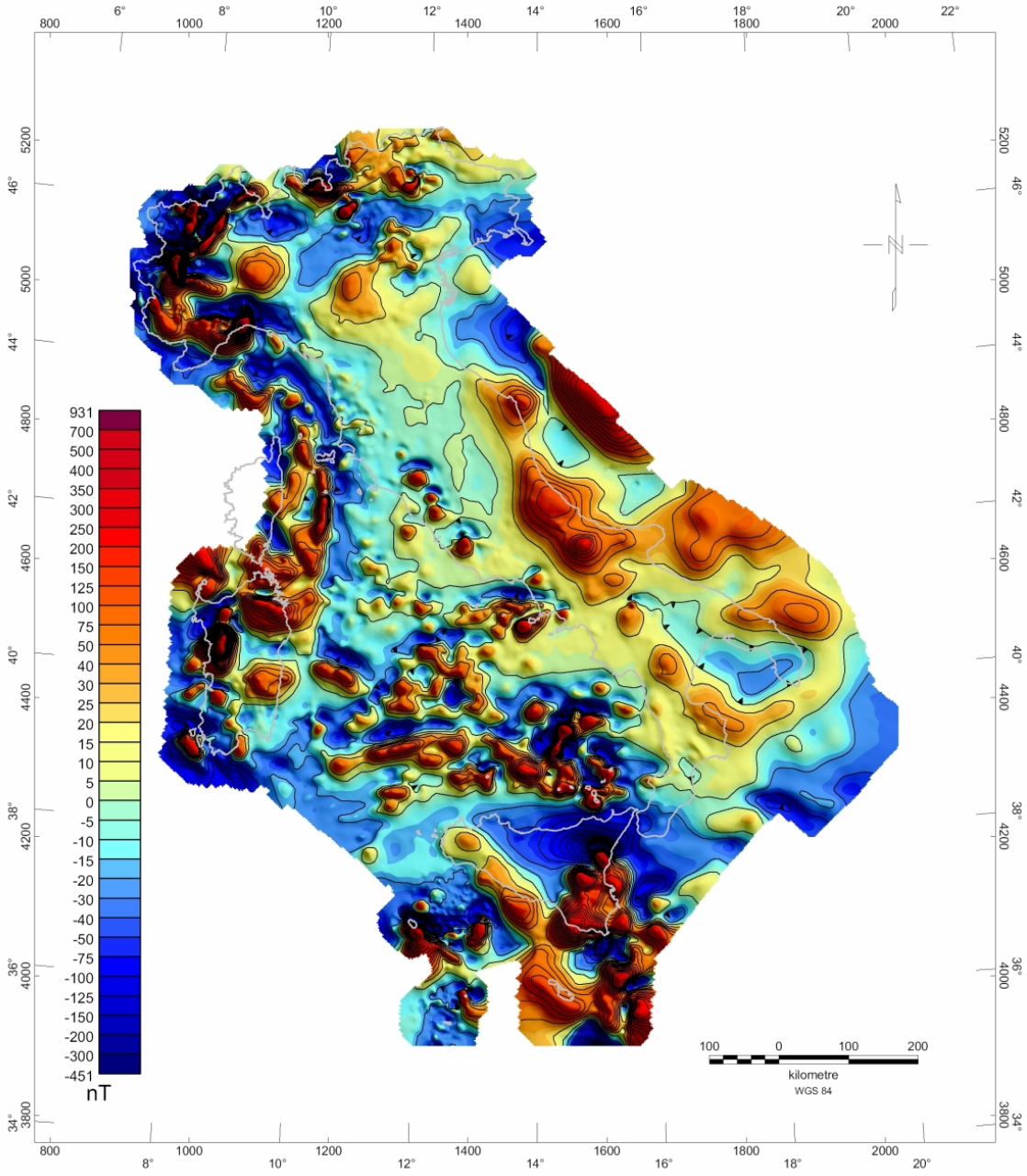

Figure 4.2: Aeromagnetic Anomaly Map of Italy, contour-line every 25 nT, from Caratori Tontini et al.(2004), magnetic data acquired by Agip-Eni

Tyrrhenian Sea (n. 72), Sardinia region (n. 83-85), Campanian-Calabrian coast and a portion of the Southern Apennine (n. 76) and Puglia Region (n. 77)(Fig. 4.3). The result of this integration is given in figure 4.4.

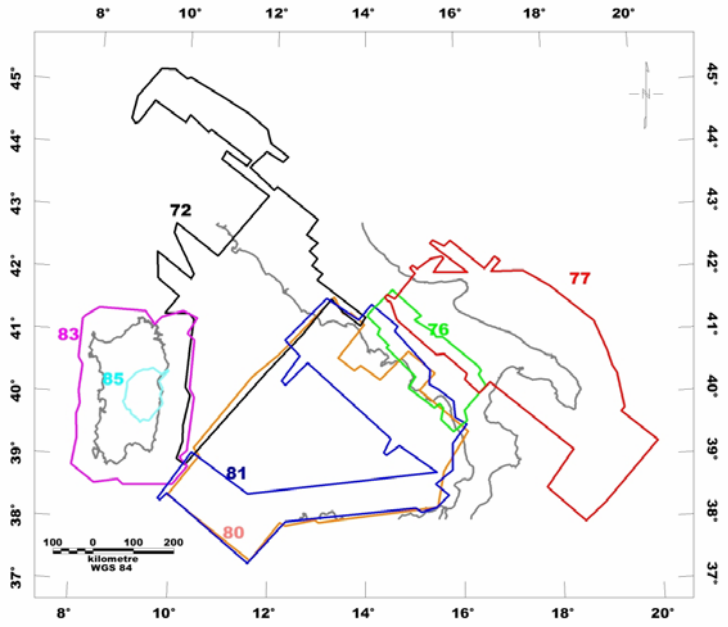

Figure 4.3: Geometry of the seven micro-surveys of the Central Tyrrhenian area

If I observe the frequency contribution of the anomaly field, the Central Tyrrhenian Sea is split into different magnetic domains. The 41^{st} parallel is an E-W magnetic lineament where several high-value anomalies connect the continental area of the Gulf of Naples with the magnetic evidences of the NW Sardinia basement. This lineament may be considered a boundary between two different magnetic regimes: the North Tyrrhenian domain shows a main component of low frequency, whereas the Southern Tyrrhenian Sea is dominated by high-frequency anomalies. In the Southern Tyrrhenian domain, the magnetic pattern is due to the presence of a shallow oceanic crust along with a high density of volcanic edifices. The magnetic anomalies are strongly correlated to the submerged structure of the area in that the two main oceanic basins, Vavilov and Marsili, show a distribution of anomalies compatible with their morphology. Additionally, these two abyssal basins are separated

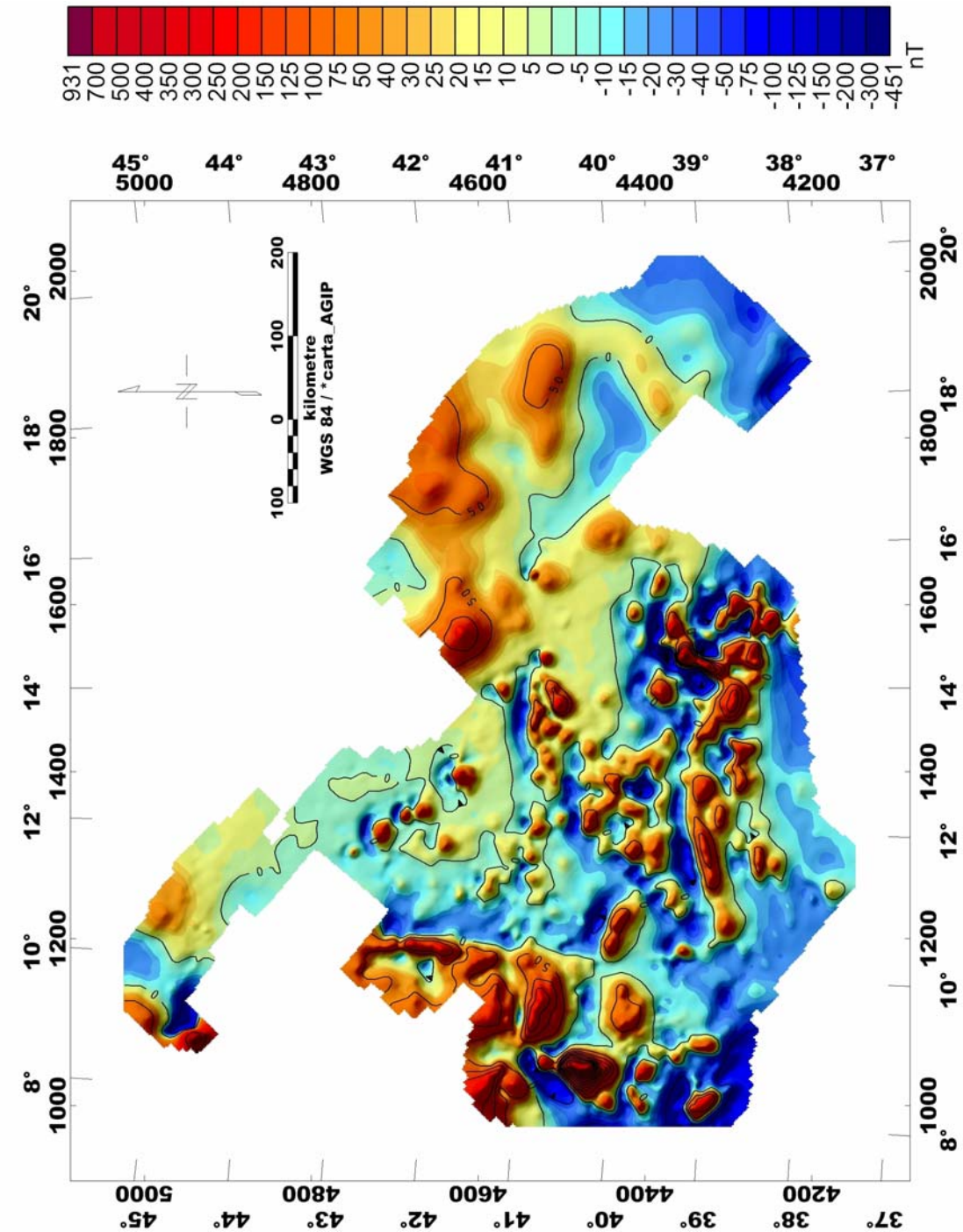

Figure 4.4: Anomaly map of the Central Tyrrhenian Area

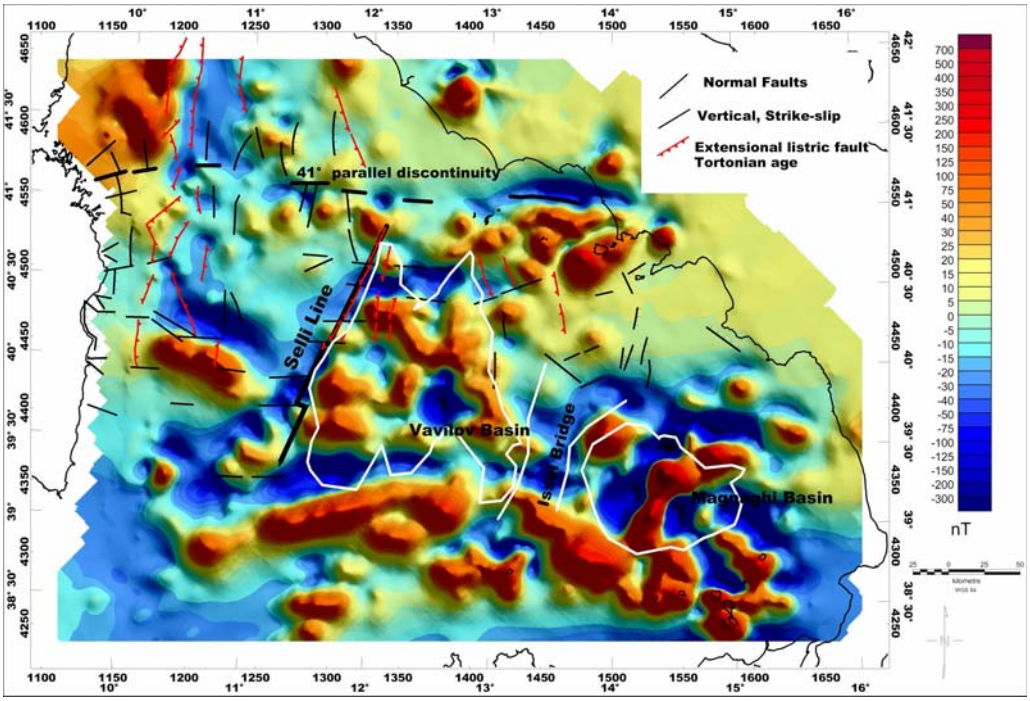

Figure 4.5: Tectonic-structural features superimposed to the anomaly map of the Central Tyrrhenian Sea

by a thick crustal channel known as the Issel bridge, which is characterized by a low-amplitude magnetic signature (Fig. 4.5). The oceanic-related magnetic pattern starts at a point corresponding to a main system of normal faults extending NE-SW, named the Central Faults-Selli Line, a structure which may be considered as the changing point of the extension in the Southern Tyrrhenian Sea. The magnetic anomalies of the 41^{st} are linked partly to buried generating sources and partly to effusive edifices of Plio-Quaternary magmatism, and at the westernmost portion of this lineament there are three separate anomalies with amplitudes ranging from 30 to 100 nT (Fig 4.6 box A) without bathymetric evidence.

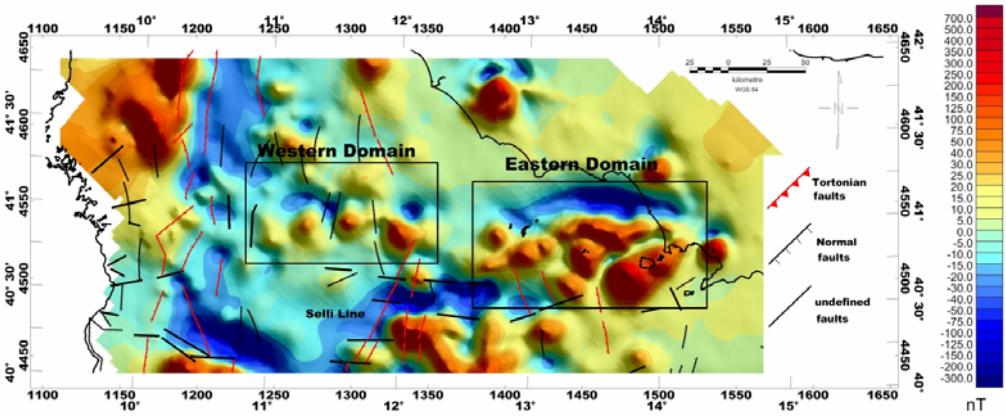

Figure 4.6: Anomaly field of the 41^{st}parallel zone, the black boxes define different magnetic evidences

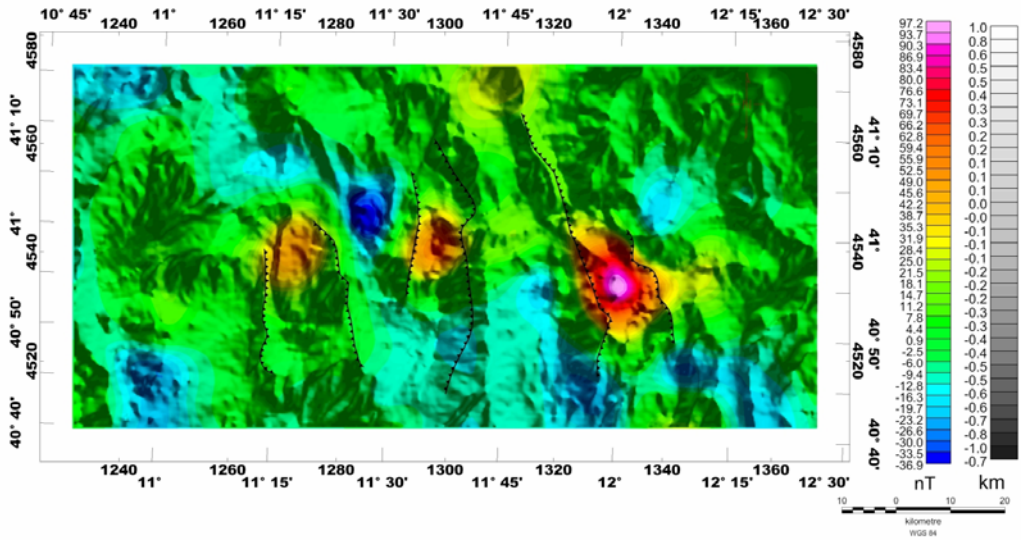

Figure 4.7: Reduced to-the-pole anomaly map of the western portion of figure 4.6; the transformed anomaly field is superimposed on the shaded relief bathymetry map *(ISMAR-CNR data)*

The reduced-to-the-pole anomalies (Inclination I=56.8°and declination D=-1.14°) of these three evidences are located in small basins, separated by a N-S trending structural high (Fig 4.7). The relationship between the anomaly field and bathymetry may be indicative of the depth of the magnetized bodies, and these anomalies can be associated with granitic/granodioritic intrusions of Tortonian age such as the Vercelli Smt (Barberi et al., 1978). In the central-eastern portion (Fig 4.6) of the 41^{st} zone the magnetic anomaly field is caused by high-magnetization rock of calc-alkaline volcanism such as the Pontine Islands (Pliocene-Pleistocene age, Cadoux et al., 2005) and Ischia and Procida islands (Pleistocene). In this area, the magnetic anomaly field has a higher intensity (max 250-300 nT) due to a contribution of sources such as the Campanian district. The 41^{st} parallel lineament shows a non-homogeneous magnetic pattern caused by the different shapes, depths and nature of its sources while the E-W distribution of the sources corresponds to a chronology of the magmatic events linked to the Tortonian-Pleistocene evolution of the Tyrrhenian Sea.

5 Analysis of the Magnetic Signal

This chapter addresses the properties of the magnetic anomaly field and analysis of its signal. The frequency behaviour of the magnetic anomaly is obtained by applying the Fast Fourier Transform to the signal data. Subsequently a spectral analysis is focused on the magnetic data of the 41^{st} parallel zone, with a statistical study of the power spectra and application of the Continuous Wavelet transform. Both these methodologies are useful for a qualitative interpretation of the magnetic structure of the 41^{st} parallel zone, which confirms its role as magnetic boundary.

5.1 The spectral analysis

The aim of magnetic prospection is to obtain the physical parameters of the generating source of the magnetic signal such as geometric features, depth and susceptibility values. The evaluation of each of these parameters requires a suitable method of analysis, and for example spectral analysis provides information about the features of the magnetic signal in the frequency domain such as its differentiating frequency band associated with the vertical distribution of the generating sources. Since the intrinsic characteristics of the magnetic field are not visible from a simple function that works in the spatial domain, the procedure begins with the magnetic signal represented as a series of functions:

$$F(x, y) = \sum_{k=1}^{n} C_k \Phi_k, \tag{5.1}$$

where Φ_k is a generic function and C_k represents the expansion factor. Representation of the magnetic signal in the frequency domain is obtained by applying a Fourier Series. A function $F(x)$ which is continuous in the interval $\frac{-X}{2} \leq x \leq \frac{+X}{2}$ and periodic with period X may be expanded into a Fourier series:

$$f(x) = a_0 + \sum_{n=1}^{\infty} (a_n \cos \omega_n x + b_n \sin \omega_n x), \tag{5.2}$$

where a_n and b_n are the expansion coefficients (Kanasewich, 1977). The amplitude spectrum of any given frequency components is calculated by

$$F_x = \sqrt{a_n^2 + b_n^2}. \tag{5.3}$$

The phase spectrum is

$$\Phi_n = \arctan \frac{b_n}{a_n}. \tag{5.4}$$

In the case of a function which has aperiodic behaviour with a variation confined to a finite-length

$$\int_{-\infty}^{\infty} f(x)dx < \infty. \tag{5.5}$$

Fourier Transform can be represented thus:

$$F(k) = \int_{-\infty}^{\infty} f(x)e^{-ikx}dx, \tag{5.6}$$

K is called wave-number and has units of inverse distance. The relationship between wave-number and wavelength is given by

$$k = \frac{2\pi}{\lambda}. \tag{5.7}$$

Since the Fourier transform is a complex function with a real and an imaginary part, it can also be written as

$$F(k) = |F(k)|e^{i\theta(k)}, \tag{5.8}$$

where

$$|F(k)| = [(ReF(k))^2 + (ImF(k))^2]^{\frac{1}{2}},$$

$$\Theta(k) = \arctan \frac{ImF(k)}{ReF(k)},$$

$|F(k)|$ and Θ are the amplitude and phase spectrums, respectively. The total energy of the function is given by

$$E = \int_{-\infty}^{\infty} |F(k)|^2 dx, \tag{5.9}$$

where $|F(k)|^2$ is called **Power Spectrum**. The inverse formula of the Fourier transform is

$$f(x) = \frac{1}{2\pi} \int_{-\infty}^{\infty} F(k) e^{ikx} dx. \tag{5.10}$$

The Fourier transform can be extended in a function of two variables (x,y) as

$$F(k_x, k_y) = \int_{-\infty}^{\infty} \int_{-\infty}^{\infty} f(x, y) e^{-i(k_x x + k_y y)} dx dy. \tag{5.11}$$

The Fourier Transform has the property of convolution: if an $H(x)$ is obtained as an integral product of two functions $L(x)$ and $G(x)$, $F(H)$ is calculated as a product between $F(L)$ and $F(G)$. Indeed, the deconvolution property is also valid for the inverse Fourier Transform. Working in the frequency domain, the integral operation can be transformed into a simple product.

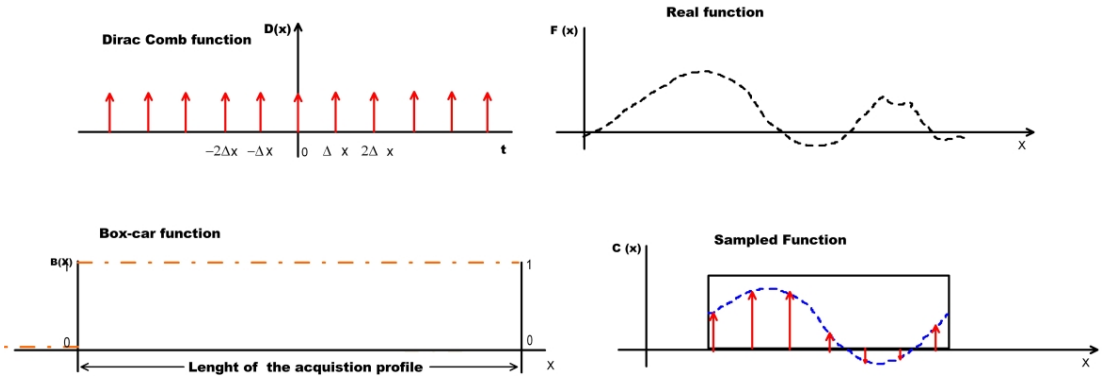

Figure 5.1: Explanation of the process of digitalization of an analogic real function

During a magnetic prospection the geomagnetic field is recorded with a constant (analogic real function) sampling step obtaining as output a discrete sequence of data $F(x, y)$. A single profile of acquisition consists of a finite number of samples spaced at a common distance, known as a sampling step. Analytically, the sampled function C(x) derives from the deconvolution of three functions: the real function f(x), the infinite Dirac-Comb function D(x) and the box-car B(x).

$$C(x) = f(x) \cdot D(x) \cdot B(x). \tag{5.12}$$

The infinite Dirac-Comb function consists of a finite series of Dirac delta functions spaced at the sampling step. The Dirac delta function is 1 on the point sampled, and zero at all other point. The box-car, also known as a rectangular window, is a function with infinity extension that is 1 along the recording profile and zero otherwise (fig. 5.1). The sampling procedure of the magnetic field is an operation of digitization and truncation. The highest frequency evaluable in a power spectrum, called Nyquist frequency, is calculated as $f_{nq} = \frac{1}{2\delta T}$ where δT is the sampling step. This relationship exists because it is necessary to have at least two samples to detect any frequency component. Working in a discrete sampling interval it is impossible to evaluate frequencies above the Nyquist frequency. In the case of a signal with frequencies higher than f_{nq}, their power will be reflected back into the power spectrum over the principal range. In this case the global power spectrum is aliased or affected by aliasing noise, an effect which may be reduced by filtering out the frequencies higher than f_{nq}. The Fourier series can be fast computed by using an algorithm called *Fast Fourier transform-FFT* (Cooley and Turkey, 1965; Good, 1958), which drastically reduces calculation time and which is the most commonly applied routine in geophysical software. In the case of a discrete Fourier series of N data, the Fourier transform is a N^2 process, which can be calculated in $N \log_2 N$ with a considerable reduction of CPU Time. The FFT algorithm has been uniformly applied in all the Fourier transformation processes related to this study.

5.2 Spectral study of the 41^{st} parallel

Spectral analysis of the magnetic signal provides different frequency-band contributions linked to distinct depths-band of the associated sources. The power spectral density shows how the magnetic signal power decays as frequency increases, hence the shape and trend of the power spectrum is directly related to the different frequency contributions. A statistical study of the power spectrum suggests that the passage from low-frequency to high-frequency sources generates a change

of slope on the spectrum (Spector and Grant, 1970) and the wavelength where this effect occurs is called the cut-off wavelength. Considering the case of the area being studied, the statistical analysis of the power spectra may highlight the different frequency features between the North and Southern Tyrrhenian Sea. This study was performed by dividing the areas above and below the 41^{st} parallel zone into a set of sub-regions. The global dataset of of the Central Tyrrhenian area was therefore divided into two matrices: the Northern and Southern Tyrrhenian sea matrices, two large areas showing an anomaly field with a lateral variation of their frequency contributions. In these cases the spectral study takes into consideration frequency contributions uncorrelated with the real magnetic pattern of the area. The regions were therefore divided into a number of sub-matrices spaced 30'x30' and for each of which the power-spectrum was computed. This procedure is shown in the following illustration (fig. 5.2):

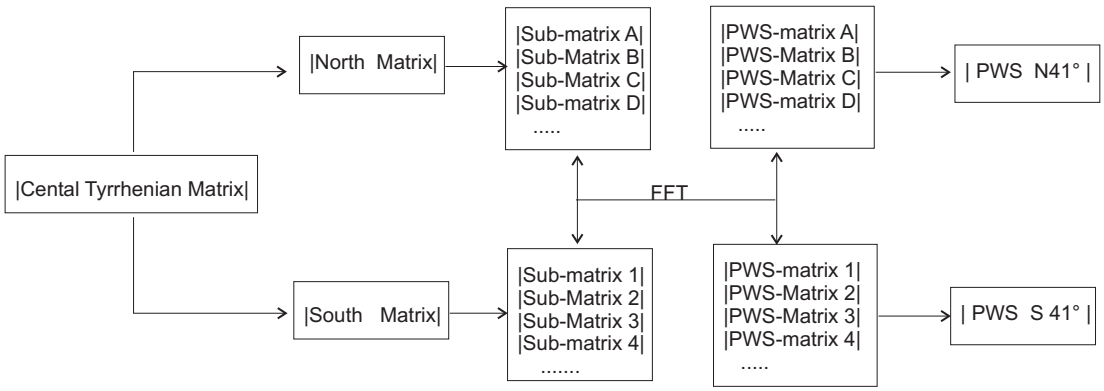

Figure 5.2: Block diagram of the power spectrum study

Evaluation of the slope change of the power spectrum of each sub area (fig. 5.3) provided several cut-off wavelength values (table 5.1), which were averaged separately for the Northern and Southern areas. The region above the 41^{st} parallel zone is characterized by $\lambda = 71km$ (fig 5.4), while the southern Tyrrhenian Sea has a $\lambda = 57km$ (fig 5.5). This result confirms the leading role of the 41^{st} in the magnetic pattern of the Central Tyrrhenian area, as a magnetic lineament dividing

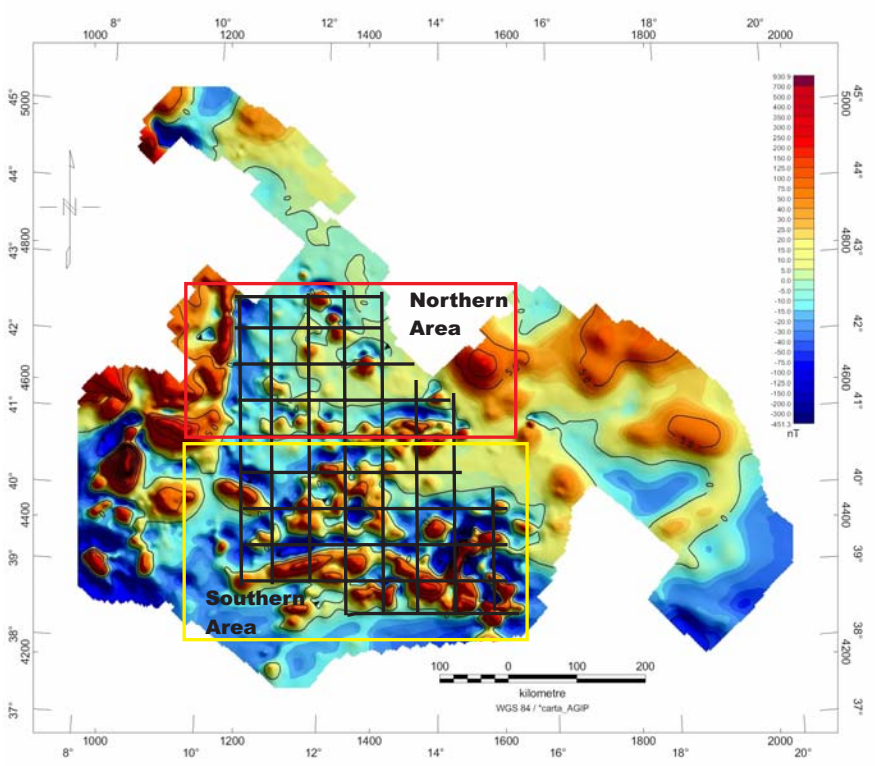

Figure 5.3: Distribution of the sub-areas related to the power spectrum study

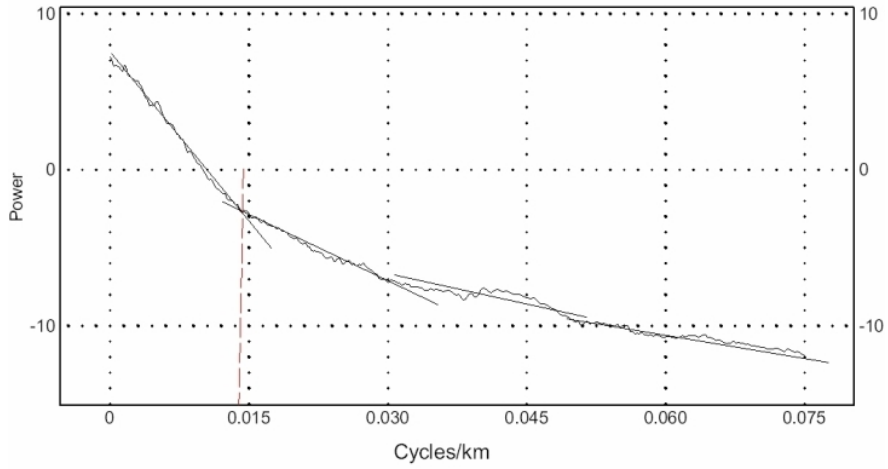

Figure 5.4: Power spectrum of the Northern Tyrrhenian area, cut-off wavelength $\lambda = 71km$

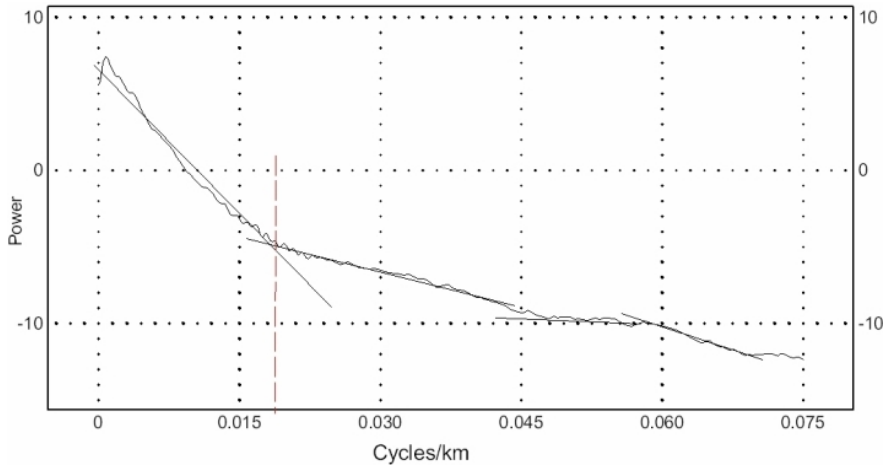

Figure 5.5: Power spectrum of the Southern Tyrrhenian area, cut-off wavelength $\lambda = 57km$

Northern Tyrrhenian Area			**Southern Tyrrhenian Area**		
Longitude	**Latitude**	**value**	**Longitude**	**Latitude**	**value**
10.58.35.0	42.06.25.6	77.00	14.24.48.3	39.25.05.1	47.00
11.35.28.8	41.37.47.2	74.00	11.52.38.4	39.43.25.1	49.00
11.09.20.4	41.18.52.3	67.00	13.54.24.7	39.35.23.7	50.00
12.25.59.8	41.27.14.4	73.00	12.41.03.1	40.04.07.7	54.00
11.48.11.0	41.06.23.2	66.00	14.37.48.2	40.14.44.5	56.00
12.08.36.2	41.15.29.2	71.00	13.10.23.5	39.36.50.5	56.00
13.57.06.7	41.01.12.1	65.00	12.23.31.1	39.15.16.5	57.00
12.56.23.5	40.59.49.8	69.00	13.44.57.8	40.17.31.8	60.00
12.13.41.1	41.39.28.9	74.00	11.08.48.8	39.54.21.9	62.00
10.57.38.8	41.47.07.8	75.00	11.09.22.6	40.28.40.4	63.00
11.48.05.5	41.57.53.4	70.00	10.41.06.0	39.22.17.6	64.00

Table 4: List of the cut-off wavelength values for the sub-regions of the Tyrrhenian Sea

the two domains characterized by different frequency contributions.

The area north of the 41^{st} is characterized by deep sources with a superimposition of scattered and shallower evidences, while the area to the south shows a high-frequency contribution associated with the several magmatic/magnetic sources located over a shallow oceanic basement.

5.3 Wavelet analysis of the 41^{st} lineament

The power spectrum study described above has suggested information about the magnetic patterns of the central Tyrrhenian area, including the fact that the frequency contribution changes in correspondence with the 41^{st} parallel. Spectral analysis is less resolutive for a 2D (X-Y surface) distribution of the magnetic anomaly field in that while this methodology may provide information about the change of magnetic pattern it is unable to determine the correct location of the boundary. To this aim, I proceeded to study the magnetic properties of the 41^{st} by using the Wavelet transform, a procedure which provides spectral variation related to its geographical position. The result of this approach is a function W defined by both spatial distribution (s) and scale (ξ), since scale ξ can represent the main wavelength of the signal at the position s. For each 1D function $f(x) \in L^2(\Re)$ the 1D-Wavelet transform is defined by the following formula (Daubechies, 1992; Foufoula Georgiou and Kumar, 1994)

$$\tilde{W}(a,b) = \frac{1}{\sqrt{a}} \int_{-\infty}^{\infty} f(x) \bar{\Psi} \frac{x-b}{a} dx. \tag{5.13}$$

In the discrete case, the associated transformation uses a discrete value of the parameters a and b. The most common solution is represented by a dyadic grid with $a = 2^m$ and $b = a \cdot n$ with a, $b \in ZxZ$ (Fedi and Quarta, 1998). The Discrete Wavelet Transform is given by

$$\tilde{W}(a,b) = \int_{-\infty}^{\infty} f(x) \bar{\Psi}_{m,n} dx, \tag{5.14}$$

with

$$\Psi_{m,n}(x) = 2^{-m/2} \Psi \frac{x - n2^m}{2^m} = 2^{-m/2} \Psi(2^{-m}x - n). \tag{5.15}$$

The mother Wavelet function Ψ has two main properties: compact support, for a correct localization in space, and a zero-mean (Farge, 1992). In the first order, the choice of this function is connected to the type of transformation. The Discrete wavelet transform is feasible only by using an orthogonal basis, whereas the Continuous Wavelet Transform requires a non-orthogonal wavelet function (Torrence and Compo, 1998). An orthogonal base function provides a power spectrum that contains discrete blocks of wavelet power. This result is due to a number of convolutions at each scale proportional to the width of the wavelet basis on that scale. Conversely, the non-orthogonal wavelet function analysis is redundant on a large scale. This last group is useful for an aperiodic and non-homogeneous dataset (Farge, 1992; Torrence and Compo, 1998). In the case of our study area, the magnetic signal was analyzed in the Wavelet domain on a non-orthogonal basis. In particular, the wavelet mother chosen is the real DOG (Derivative of a Gaussian) function considered capable of isolating peaks and/or discontinuities (Torrence and Compo, 1998).

Consequently the Central Tyrrhenian area was studied using a 1D Wavelet transform. The magnetic anomaly field was sampled by 43 N-S profiles spaced approx 10 km apart with a sampling step of 0.5 km along each profile (Fig.5.6). The data was then transformed in a 1-64 scale range of with a DOG order 2. The profile was divided into n-sections ($n = 2^9$), with the maximum scale 64 representing ($n = 2^6$).

The result of the 1D wavelet transformation is a power spectrum also called scalogram, a 2D diagram giving function W values on differing scales in that geographical position. In this case, the wavelet analysis was performed with using a Matlab Toolbox. Each scalogram of the magnetic anomaly field of the Central Tyrrhenian sea shows a minimum of the spectrum at every scale. The minimum is localized at a km-coordinate of 4530-4545 representing the projected position of the 41^{st} parallel (Fig. 5.7). This scalogram behaviour can be interpreted as the N-S variation of the magnetic signal connected with the local position of a magnetic boundary. For each profile, the minimum wavelet scalogram, or blue-point, is

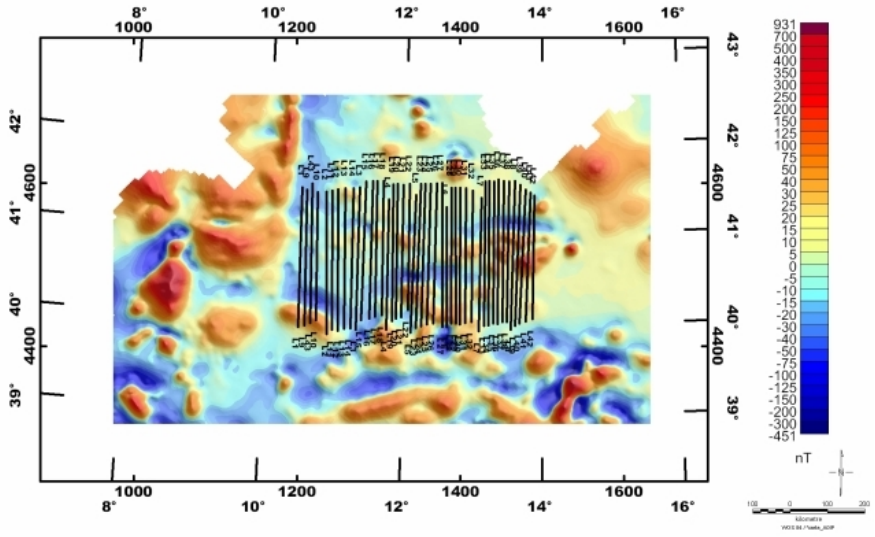

Figure 5.6: Distribution of the 43 profiles used for the wavelet analysis.The line-path overlaps the aeromagnetic anomaly field

plotted (with a clear georeference) on the magnetic anomaly map, thus obtaining a possible planar shape of the discontinuity (Fig. 5.8).

The minimum coefficients are all located along the 41^{st} parallel above the individual magnetic evidences in a distribution pattern which appears to confirm the presence of a magnetic boundary between the Northern and Southern Tyrrhenian basins. Proceeding from these results, a similar analysis was performed using the gravity data with the Bouguer anomaly of the Tyrrhenian Sea as previously described in chapter 2. The gravity data were sampled long the same 43 profiles of the magnetic analysis using the same sampling step. In this case the Continuous Wavelet Transform was based on a DOG wavelet basis on a scale ranging from 1 to 128, and the resulting scalograms show minimum wavelet coefficients located at the km-coordinate of the 41^{st} parallel zone in the same way as in the case of the magnetic data (Fig. 5.9). This result is indicative of a gravity/density differentiation between the North and South Tyrrhenian, since it shows a decreasing trend in the Bouguer anomaly range from the Southern basin to the Northern one. The

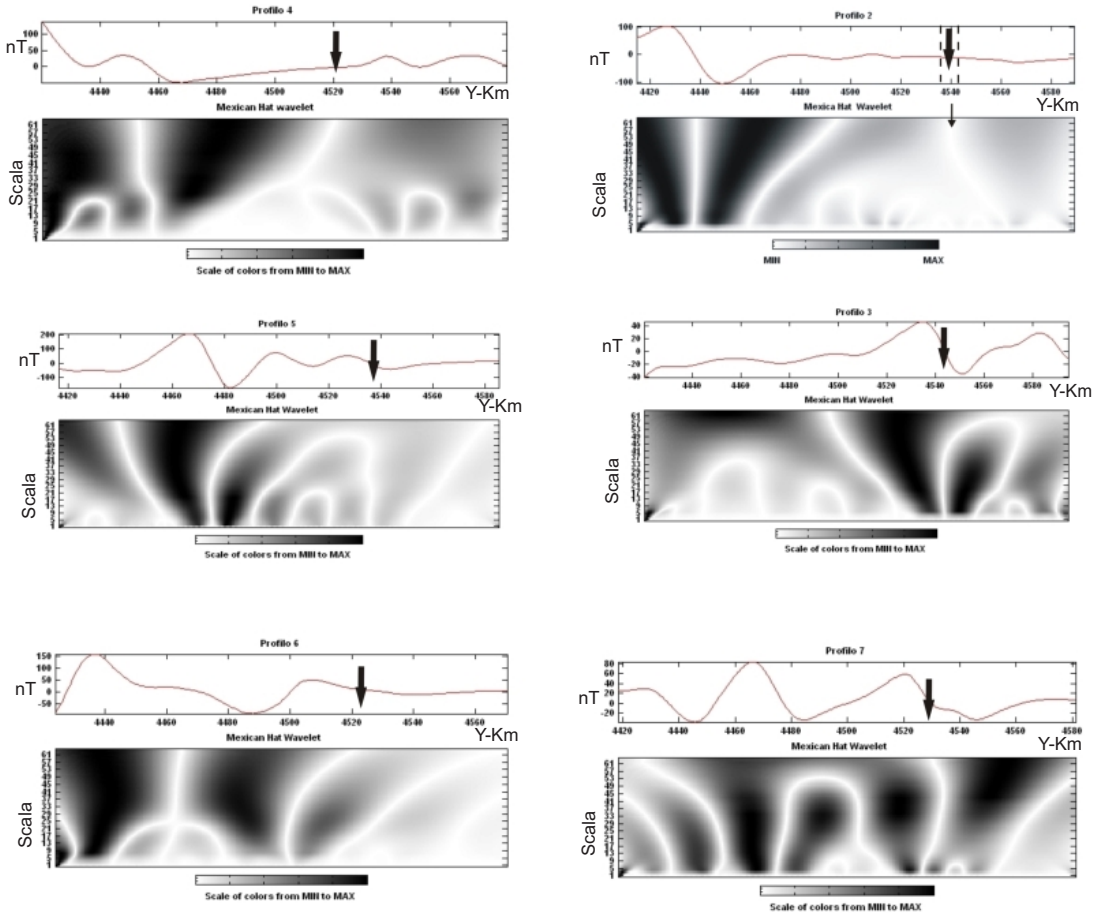

Figure 5.7: Scalograms of the ($n = 6$) magnetic profile (profiles from n.2 to n.7), the wavelet transform is calculated using DOG 2^{st} order with maximum scale 64

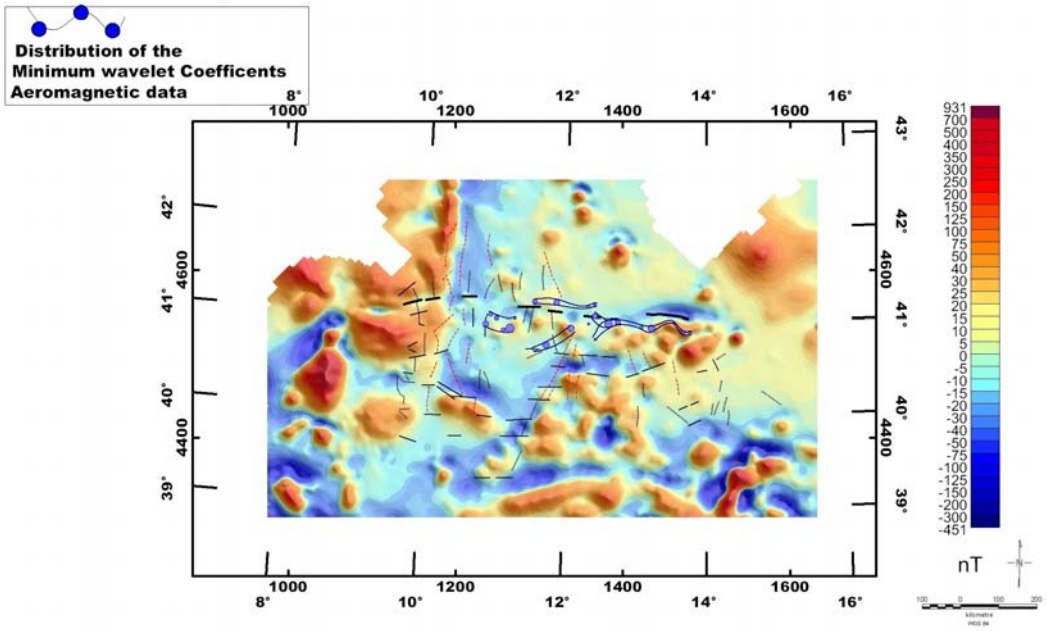

Figure 5.8: Geographic distribution of the minimum wavelet coefficients of the magnetic data superimposed to the magnetic anomaly field

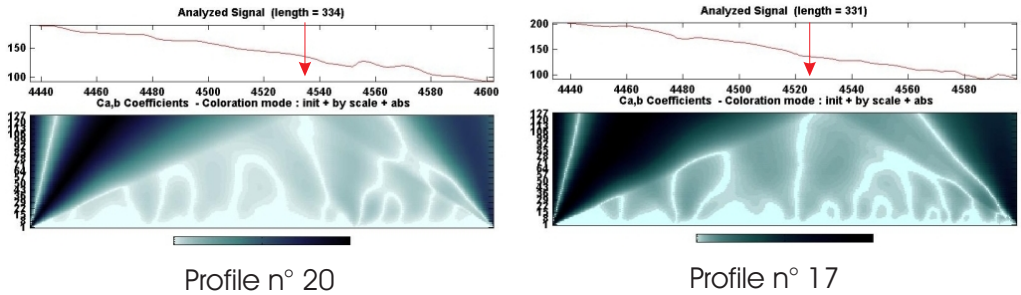

Figure 5.9: Two samples of scalograms related to the gravity data profiles n.17 and n.20

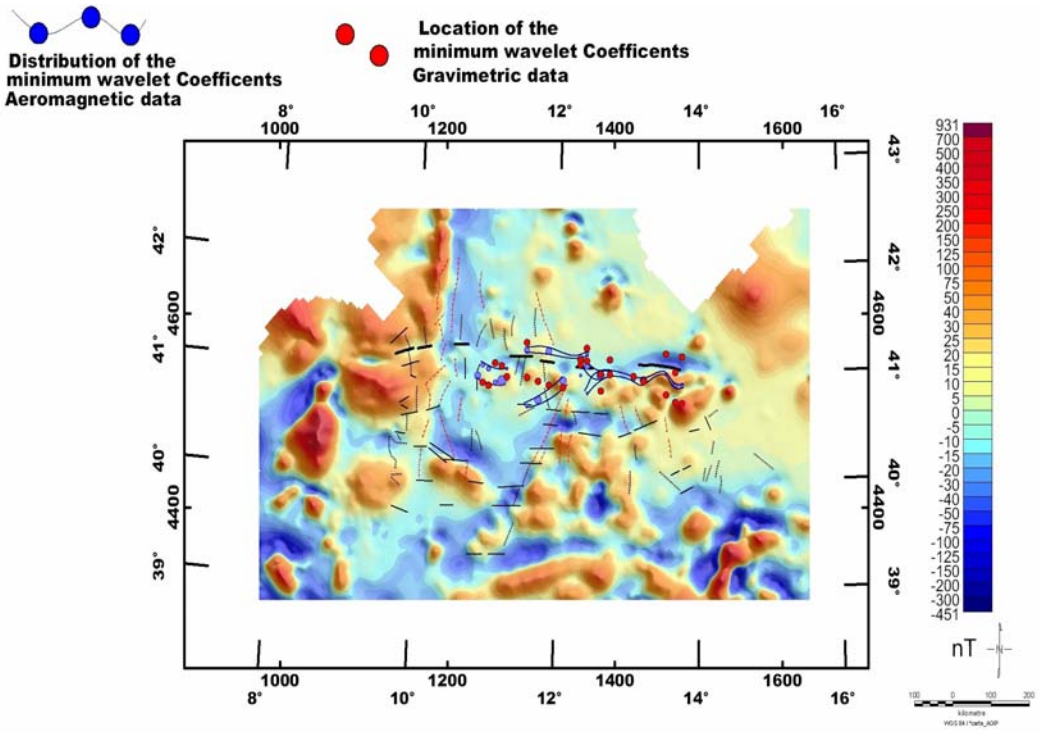

Figure 5.10: Distribution of the minimum wavelet coefficients of the magnetic and gravity data superimposed to the magnetic anomaly field

Wavelet analysis has highlighted a particular gravity behavior of the Central portion of the Tyrrhenian which is not evaluable from the Bouguer anomaly map. Indeed, by mapping the gravity and magnetic minimum wavelet coefficients it is possible to see a correlation between the magnetic and gravimetric boundaries (Fig. 5.10). The wavelet analysis confirmed the presence of a magnetic boundary along the 41^{st} parallel zone with a quantitative evaluation of its planar distribution. The same results are obtained by applying the Wavelet analysis to the gravity data: along the 41^{st} there exists a density/gravity discontinuity. In the light of these results, the 41^{st} represents the changing point of the main magnetic and gravity properties of the Tyrrhenian area, and it may be interpreted as a crustal boundary between the two Tyrrhenian domains.

6 The magnetic basement

The magnetic anomaly field of the Central Tyrrhenian area shows a peculiar distribution, with a clear boundary between two magnetic domains represented by the 41^{st} parallel zone. Following definition of the magnetic discontinuity's geographic location through the Wavelet analysis described in the previous chapter, this section studies the depth distribution of the magnetic sources. More precisely I estimate the upper and lower surfaces of the magnetic basement by using spectral analysis and inverting the shallow heat flow. The resulting better definition of the magnetic crustal portion's shape and thickness is decisive for an inverse study of the magnetic data.

6.1 The concept of magnetic basement

The magnetic anomaly field is a convolved signal due to the superimposition of several contributions. In the case of a delimited area, the anomaly field may be considered as a convolution of some anomalous contributions from all the magnetic sources located in the magnetic crustal portion, known as magnetic basement. The concept of magnetic basement is based on the distribution of magnetic susceptibility and it is commonly associated with high-susceptibility crystalline crustal portions, unlike the low-susceptibility sedimentary units which do not belong to this magnetic crustal portion. Distribution of the top of the magnetic basement is generally assumed to coincide with the base of the sedimentary covers. Although from a magnetic point of view the limit between sedimentary units and magnetic crustal portion is not very well defined, a spectral study makes it possible to obtain a depth range of the low-susceptibility sedimentary covers. The relationship between magnetic and geologic basements is also problematic, an example being the fact that low magnetized metamorphic sequences not forming the magnetic basement may be considered true elements of the geologic basements. As a result it is necessary to study the vertical distribution of the magnetic basement in small clearly limited

areas where the magnetic pattern and its deep geologic features are well defined.

The Central Tyrrhenian area shows geological features associated with the Miocene-Quaternary geodynamic evolution of the basin. Along the 41^{st} parallel zone lies a fault system extending from the continental Campanian Margin to the N-E Sardinia, in an area containing several volcanic structures such as the Vercelli Smt, Cassinis Smt. and Pontine Islands, all of which are imposed on a clear magnetic basement. The shallower volcanic evidences are well isolated in the high-frequency domain while the deeper magnetic portion is less clearly defined. In this case, the top of the basement was defined by a iterative study of the power spectrum (Spector and Grant, 1970), whereas the bottom surface was computed by inverting the heat flow data.

6.2 The top of the magnetic basement

Although a spectral study of the magnetic signal gives information on the generating source it fails to indicate a clear relationship with the geologic setting. The high frequencies are commonly correlated with the shallower sources, whereas the low-frequency contribution is due to the deeper magnetic bodies. The different magnetic portions of the crust are studied in order to distinguish the different frequency bands of the signal. When a spectral study is applied to a bi-dimensional distribution of magnetic anomalies, the resulting power spectrum is called radial average power spectrum. The direct link between the frequency band of a generating source family and its depth is obtained by a statistical study of the radial average power spectrum (Spector and Grant, 1970). By this method it is possible to calculate the top of the source. Spector and Grant (1970) portray the geological body as rectangular prismatic ensembles where each ensemble is characterized by a joint frequency distribution for the depth, width, length and magnetization. The power spectrum of the total magnetic field generated by a single rectangular prism

is given by Bhattacharyya (1966)(in polar frequency coordinates ρ,ϑ):

$$E'(\rho,\vartheta) = \left(\frac{\mu_0}{2}\right)^2 k^2 e^{-2h\rho}\left(1-e^{t\rho}\right)^2 S^2(\rho,\vartheta)R_T^2(\vartheta)R_K^2(\vartheta), \tag{6.1}$$

where μ_0 is the magnetic permeability and k is a magnetic moment/unit depth, S, R_T^2 and R_k^2 are given by

$$S(\rho,\vartheta) = \frac{\sin(a\rho\cos\vartheta)}{a\rho\cos\vartheta}\frac{\sin(b\rho\sin\vartheta)}{b\rho\sin\vartheta}, \tag{6.2}$$

$$R_T^2 = n^2 + (l\cos\vartheta + m\sin\vartheta)^2, \tag{6.3}$$

$$R_K^2 = N^2 + (L\cos\vartheta + M\sin\vartheta)^2, \tag{6.4}$$

where l, m, n are direction cosines of the Geomagnetic field vector and L, M, N are direction cosines of the magnetic moment vector K

The reduced-to-the-pole expression of equation 6.1

$$E(\rho) = \left(\frac{\mu_0}{2}\right)^2 \overline{k}^2 C\left(\rho,\overline{a},\overline{b}\right) T\left(\rho,\overline{t}\right) H\left(\rho,\overline{h}\right), \tag{6.5}$$

where C is the azimuthal average

$$C(\rho,\overline{a},\overline{b}) = \frac{1}{\pi}\int_0^\pi \langle S^2(\rho,\vartheta,a,b)\rangle d\vartheta, \tag{6.6}$$

the parameters T and H are

$$T(\rho,\overline{t}) = \langle\left(1-e^{-t\rho}\right)^2\rangle = 1 - \frac{\left[\left(3-e^{-2\overline{t}\rho}\right)\left(1-e^{-2\overline{t}\rho}\right)\right]}{4\overline{t}\rho}, \tag{6.7}$$

$$H(\rho,\overline{h}) = \langle\left(e^{-h\rho}\right)^2\rangle = e^{-2h\rho}\frac{\sinh(2\rho\Delta h)}{2\rho\Delta h}. \tag{6.8}$$

The ensemble average depth h enters only into the factor $e^{-sh\rho}$ for $\Delta H < 1/h$. The logarithm of this factor approximates a line whose slope is -2h. The depth evaluation of the top of a generic prismatic ensemble is given by

$$h(depth) = -\frac{1}{2}\frac{\Delta \log\left(E(\rho)\right)}{\Delta\rho}. \tag{6.9}$$

The depth evaluation with Spector and Grant model is underestimated (in the case of the high frequency band) because the behaviour of the red power spectrum follows a power law decay connected to the C-factor (Fedi et al., 1997). The plot of log C vs Log ρ shows a curve that decays with a power law ρ^{β}. For large sources $\beta = 2.9$. In these terms, the power spectrum obtained with Spector and Grant's model should be corrected for the factor $\rho^{2.9}$ (Fedi et al., 1997).

$$E(\rho) \cong \left(\frac{\mu_o}{2}\right)^2 \overline{k}^2 \rho^{-2.9} H(\rho, \overline{h}). \tag{6.10}$$

The modified power spectrum provides a correct depth estimation, which is why this approach is applied when estimating the top magnetic basement of the 41^{st} parallel zone by dividing the area of interest into several sub-regions as previously described in chapter 5, figure 5.3. For each sub-area the radial average power spectrum was calculated, and the slope change of each single power spectrum studied in order to estimate the different generating source ensembles. In all cases the depth-estimation was focused to the lowest-frequency sources.

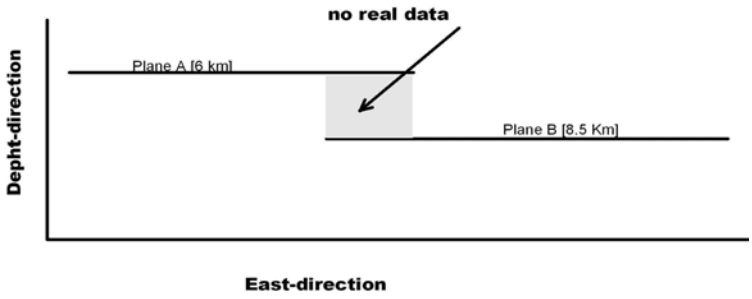

Figure 6.1: Schematic example of a lack of real data between two planes

The depth-value of the top basement was set as the center of the sub-region and the first result of this procedure was a series of planes located at different depths, which however created the problem of a partial overlap between two nearby planes (fig.6.1).

The gap in values between two zones was solved by a geostatistic analysis, a procedure which re-distributes the real data by extrapolating the depth values where no data is available. The stochastic analysis is based on a set of regionalized variables in a method known as multi-space kriging analysis (Cressie, 1990). The spatial continuity degree of a regionalized variable can be explained by a variogram (semi-variance/distance), therefore in the case of a bi-dimensional map the expression of the 2D variogram is the following:

$$\gamma(p,q) = \frac{1}{2\,(m-p)\,(n-q)} \sum_{i=1}^{m-p} \sum_{j=1}^{n-q} \left[z_{(i,j)} - z_{(i+p,j+q)} \right]^2, \tag{6.11}$$

where p and q are the dimensions of the grid size along $i - row$ and $j - column$; m and n are the position of the point. The kriging extracts a set of optimal weights from the variogram and estimates the value of the variable where there is no real data. This step gives us a continuous isobath of the top of the magnetic basement (fig 6.2). Figure 6.3 gives the top basement surface of the 41^{st} parallel zone, where

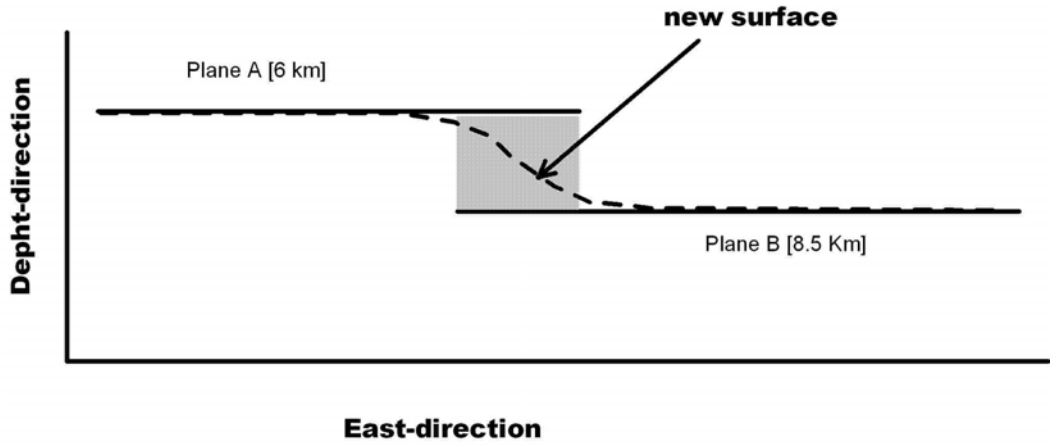

Figure 6.2: Homogeneous distribution of the real data after a kriging analysis

the top shows a homogeneous distribution with depths ranging from 4 km to 8-10 km. Along E-W direction (41^{st} parallel, profile in figure 6.3) the top of the basement is located at a depth of 6-7 km, while near to the Campanian margin the depth of the basement increases (8-10 km). Considering a N-S profile, the top of the basement

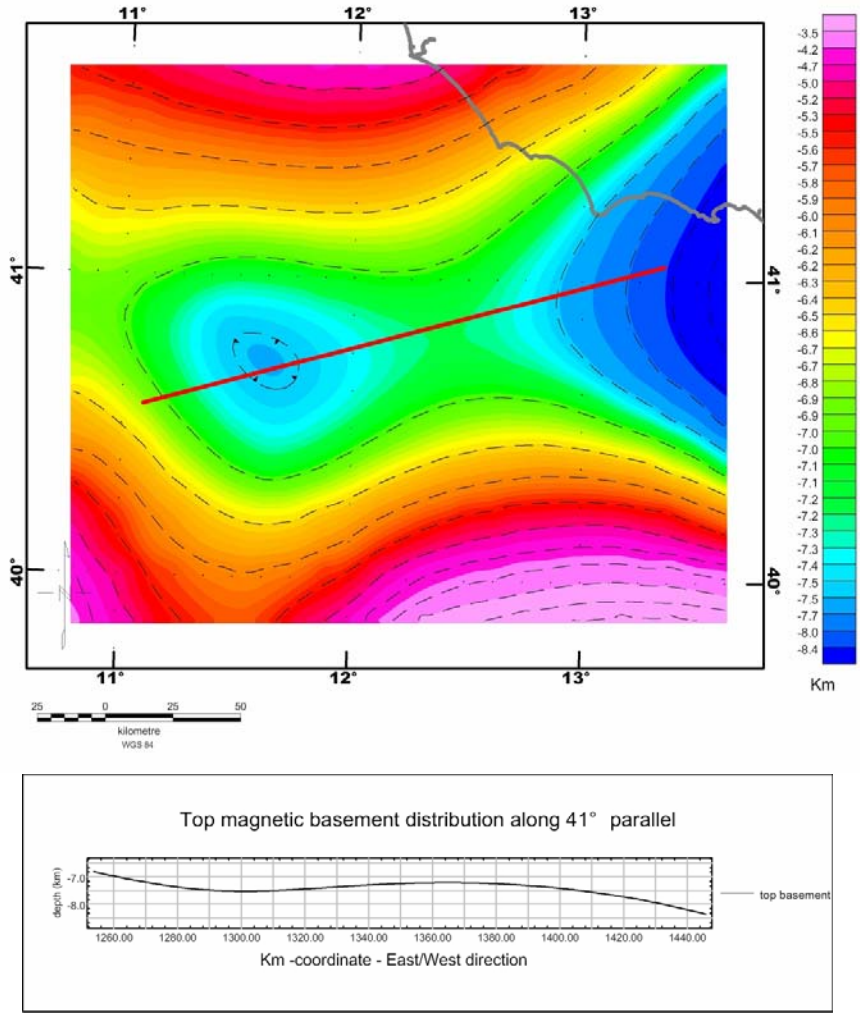

Figure 6.3: (Map) Bidimensional depth-distribution of the top magnetic basement of the 41^{st} parallel zone; (Profile) 1D distribution of the depth of the basement along a E-W direction (red track in the map)

shows a decrease in depth with a minimum of 2-3 km centered on the Magnaghi-Vavilov Basin. In this region, the magnetic crustal portion is shallower due to the

Tortonian stretching of the crust. Around the 41^{st} parallel lineament the depth of the top basement surface increases, whereas above this latitude it decreases slightly down to 5 km. The 41^{st} parallel area may therefore be considered a local magnetic basement along which the top of the basement is moderately deep (middle crustal portion) suggesting the presence of a non-magnetized shallow crustal portion. The geologic-tectonic setting of the study area is characterized by a sequence of thrusts, where several continental blocks are superimposed on the metamorphic-crystalline basement (Finetti et al., 2003).

6.3 The bottom of the magnetic basement

The lower portion of the magnetic basement is calculated according to the Curie Isotherm depth distribution, by which the magnetic signature of the crust decreases in value as the temperature increases. The Curie Point of a material represents the thermal limit above which the magnetic properties change from paramagnetic to diamagnetic: a temperature higher than the Curie isotherm causes the Weiss domains to break, thus generating a random distribution of the electrons (Telford,1990). In geology the value of the Curie isotherm is related to the main ferromagnetic minerals of the crustal portion being studied since the magnetic signature of a rock is generally due to its Magnetite $FeFe_2O_4$ content.

The basic-ultrabasic crustal portions contain ferromagnetic minerals such as Ulvospinel (Fe_2TiO_4), Magnesium-Ferrites ($MgFe_2O_4$) and Spinel s.l $((Mg, Fe)(Al, Fe, Cr)_2O_4)$. Table 6.1 lists the Curie temperature of relevant minerals. If we evaluate the paragenesis of the upper crustal portion, we see that the most widespread ferromagnetic mineral is magnetite s.s, while the other oxides can be considered as secondary minerals. Using this information, the thermal model was computed inverting the surface heat flow data with a fixed temperature value $T = Tcurie = 580°$. In a steady thermal condition, the heat flow is influenced by two main factors: asthenospheric and radiogenic contributions. The first reflects

crustal heating due to a convective movement inside the asthenosphere, while the second is a result of the radioactive decaying of radiogenic elements inside the crust which produces a form of heating defined radiogenic. This model was developed in a steady thermal state on a heat flow dataset derived from the cited Heat Flow Map of Italy and Surrounding Seas (Della Vedova et al. 2001)(fig. 6.4). This surface heat flow distribution is the result of integration and re-processing of data acquired over the last 20 years and the global HF database integrates the measurements of the sedimentary basins (Della Vedova and Pellis, 1980; 1988), rift zone (Della Vedova et al., 1984; 1988; 1993; Della Vedova and Pellis, 1986; Hutchinson, 1986; Burrus and Foucher, 1986; Kastens et al., 1987), mountain bells (Rybach and Jaffè, 1976; Rybach et al., 1977; Pasquale, 1985) and the cratonic areas (Loddo et al., 1982). As a result of these measurements, we now have several HF maps of Italy and its surrounding seas (Mongelli et al., 1991; Cataldi et al., 1995) and the current HF database of Italy incorporates data from more than 500 shallow wells (300 m) drilled for geothermal prospecting (Bellani et al., 1994), 150 geothermal wells (3000-4000 m deep) located in Tuscany and Latium, approx 1850 hydrocarbon exploration wells (7000 m deep) scattered all over Italy and finally 700 marine HF measurements (Della Vedova et al., 1995).

Departing from the surface heat flow data, the Curie isotherm distribution was evaluated according to the thermal gradient (temperature vs depth) using as constraints crustal thickness (from Nicolich and Dal Piaz, 1992; Nicolich, 2001) and V_p distribution (Panza el at., 2003). The p-wave velocity distribution suggests different rheologic features within the crust and this factor is useful to infer the thermal conductivity. In the Central Tyrrhenian area the p-wave velocities range from 4.5 to 4.8 km/s (Panza et al., 2003) and the expected thermal conductivity is $K_{rc} = 2.9 W/mK$ (Pasquale et al., 1990). The radiogenic component of heat flow depends on A_0 as coefficient of radiogenic heat production:

$$A(z) = A_0 \exp\left(\frac{-Z + Z_0}{C}\right), \tag{6.12}$$

Mineral	Magnetic behaviour	T°Curie
Ilmenite	anti-ferromagnetic	-205°
Chromite	Ferromagnetic	-185°
Magnetite	Ferromagnetic	575°
Ulvospinel	anti-ferromagnetic	-153°
Hematite	anti-ferromagnetic-ferromagnetic	675°
Pyrrhotite	Ferromagnetic	320°
Maghemite	Ferromagnetic	675°-750°

Table 5: Curie Point of the main minerals forming the upper crustal portion (from Carmichel 1989)

where Z and Z_0 are the upper and lower crust boundaries and C is the vertical limit of the radiogenic source (8 km from Zito et al., 2003) The radiogenic contribution Q_{rad} is given by

$$Q_{rad} = \int_{Z_O}^{Z} A_z dZ. \tag{6.13}$$

The thermal gradient is obtained by this differential equation

$$\frac{dQ}{dZ} = -A_0 \exp\left(\frac{-Z}{C}\right), \tag{6.14}$$

$$Q(z) = K\frac{dT}{dZ}. \tag{6.15}$$

The final relation between temperature and depth is

$$T(Z) = T_0 + \frac{Q_0 Z}{K_{cr}} - \frac{A_0 C Z}{K_{cr}} + \frac{A_0 C^2}{K_{rc}}\left(1 - \exp^{\frac{-Z}{C}}\right), \tag{6.16}$$

where T_0 is the temperature at depth Z_0, Q_0 is the surface heat flow value and $K_{rc}$is the thermal conductivity. Equation 6.18 expresses the thermal state as a function of depth. The thermal gradient is studied for different values of surface heat flow by using an iterative procedure (fig.6.5). Departing from a fixed temperature value, equation 6.18 is solved using $T(z) = 580°$(Curie point of magnetite) calculating the

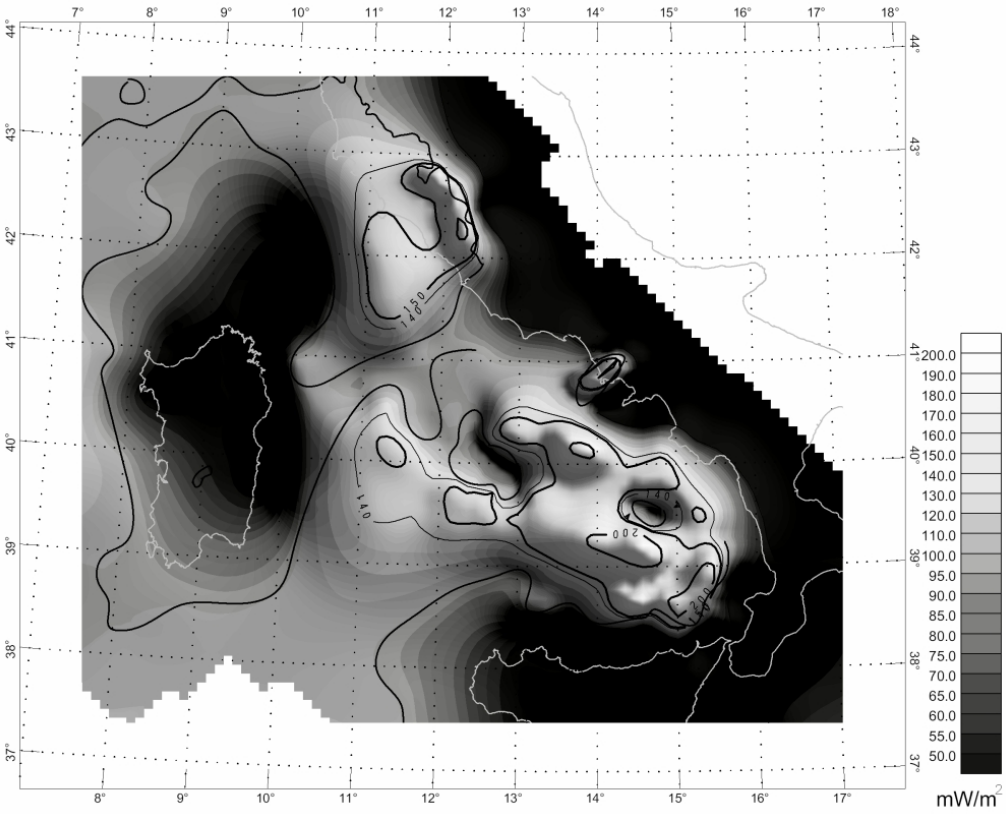

Figure 6.4: Surface heat flow distribution of the Tyrrhenian region redrawn from Della Vedova et al. (2001)

$Z(T_{curie})$ depth of the Curie isotherm. This procedure was applied to each heat flow data point to obtain a 2D Curie point depth distribution referred to as Curie isotherm surface (fig.6.6).

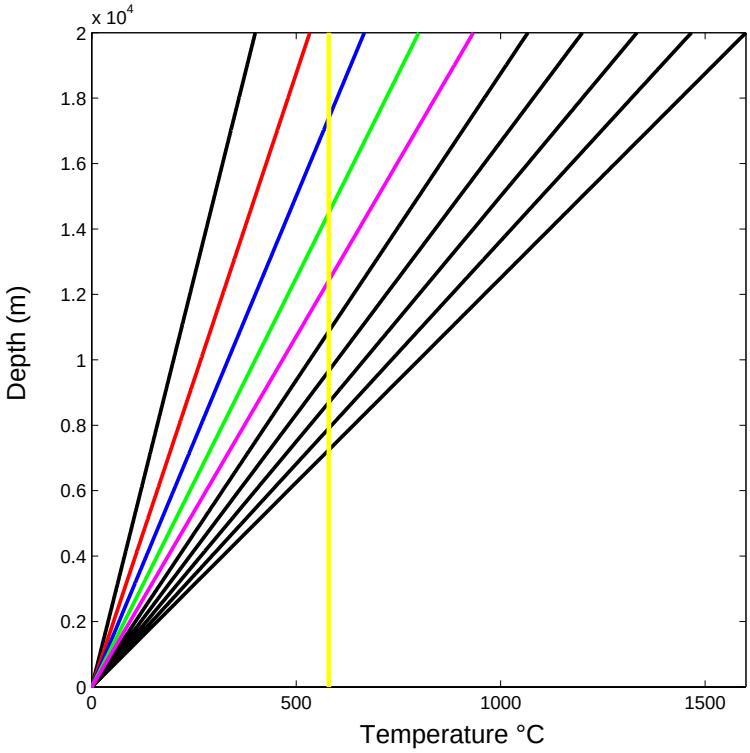

Figure 6.5: Thermal gradient evaluated at different Heat flow values

The Curie isotherm distribution shows good agreement with the Moho discontinuity Map (Nicolich, 2001). The bottom of the magnetic basement is located above the Moho limit ranging from 30 km (Sardinia region) to 7-8 km (Southern Tyrrhenian sea). In the study area, the Curie-depth ranges from 7 to 27 km. The higher depth values are localized in the continental zone between Tuscany and Latium, where there is a large geothermal field. The two Tyrrhenian basins (North and South) are characterized by low HF values and by a shallow Curie isotherm depth (7-9 km). From the thermal point of view the 41^{st} parallel zone shows a peculiarity: along this parallel the magnetic basement becomes deeper(17-18 km) than the Northern and Southern Tyrrhenian sea. This feature may be evidence of a thermal boundary between the two Tyrrhenian domains, and a similar discontinuity is also supported by the seismic data. According to Nicolich (2001) the northern and southern Tyrrhenian domains are characterized by two different mantle domains

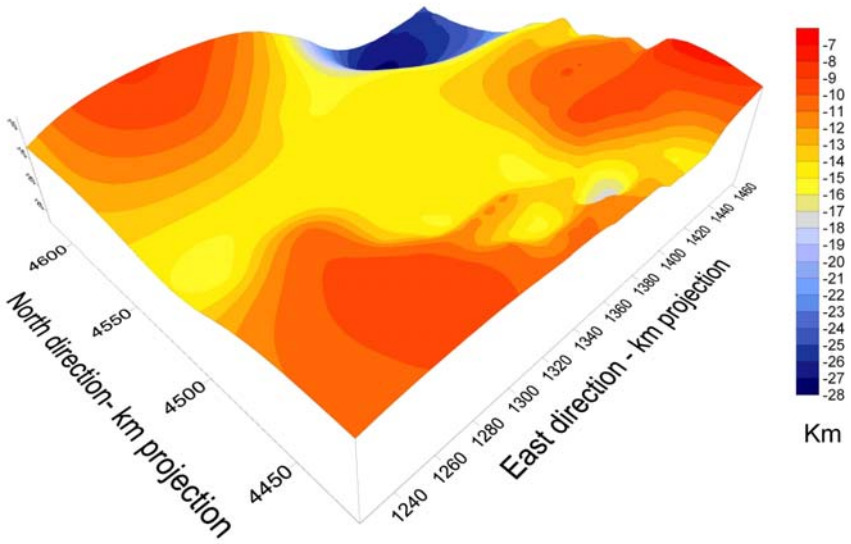

Figure 6.6: Map of Curie isotherm of the 41^{st} parallel zone

and the 41^{st} parallel represents a mantle boundary zone confirming the presence of a lithospheric discontinuity (Lavecchia, 1988; Patacca,1990). Figure 6.7 illustrates the geometric crustal features of the 41^{st} parallel zone. The depth-distribution of the basement follows the Moho-discontinuity trend with local high/low evidences due to thermal anomalies. Both the top and bottom surfaces increase in depth at the 41^{st} parallel latitude, which highlights a differentiation from the general magnetic setting. The definition of magnetic basement geometry represents a constraint for a quantitative analysis of the crustal setting of the 41^{st} parallel.

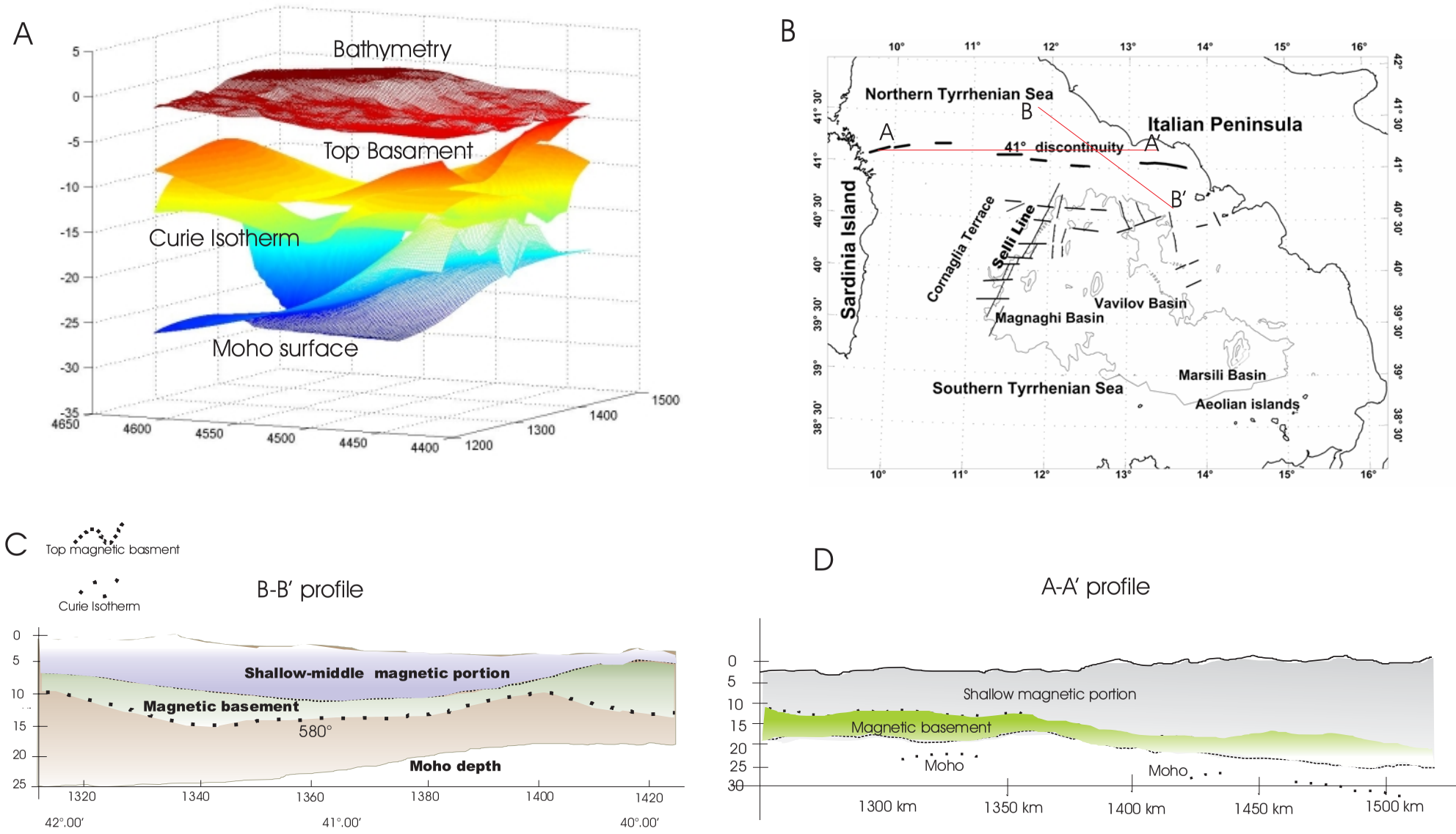

Figure 6.7: A)3D model of the crustal structure of the 41^{st} parallel area; B) Morpho-bathymetry overview of the Tyrrhenian Region, red-lines represent the track-profile of C and D sub-figure; C) profile B-B, crustal features sacross the 41^{st} parallel zone; D) profile A-A', crustal features along the 41^{st} parallel zone

7 The apparent magnetization maps

The bidimensional distribution of magnetized sources can be evaluated by different inversion techniques, one of which is mono-layer inversion. This procedure considers a common layer where all the magnetic sources producing a 2D magnetization distribution are located, and the final result is an apparent magnetization of the study area. The aim of this method is to highlight the geometric relationship of the several magnetic sources in order to provide an integrated study correlating the magnetic evidences with the geologic-structural setting of the area. To this aim, I performed a bidimensional inversion of the magnetic anomaly field of the 41°parallel, in which the mono-layer inversion was constrained to a specific crustal portion where the bottom surface is represented by the magnetic basement. The procedure was applied to both the 41^{st} parallel and to the Magnaghi-Selli line region, and the recovered model highlights a connection between the two areas represented by a common NW-SE magnetization trend.

7.1 The mono-layer inversion process

The aim of an inversion process is to obtain geometrical information on a source departing from a set of measured data. A magnetic anomaly can be modeled through an infinite set of sources with different dimensions and depth positions. The ambiguity of solutions is called the *problem of non-uniqueness*for the inversion process, and one solution to this problem may be to assume a uniform magnetization of the source or that the body is infinitely extended in one direction. A second approach may be to define the geometric set of solution determining the maximum depth of any realistic source. Although these assumptions may reduce the number of permissible solutions the fact remains that the solution is still non-unique. Starting from this point the inverse technique is a good method for interpretation of the potential field but it may be unusable without *a priori* information on the source. The choice of the inversion method is based on the information one wishes to obtain,

in that a general model that takes into consideration the vertical and planar distribution of the sources is non-feasible. It is possible to define a bidimensional model able to evaluate the magnetization on a X-Y plane but without vertical resolution. A 3D inversion process instead defines a depth position of the source but with a delimited lateral distribution of the sources. This chapter describes how we produced an apparent magnetization map using a 2D inversion algorithm. In general terms, the 2D model was computed starting from the information regarding the magnetic pattern of the study area including depth of the magnetic basement and the spectral features of the anomaly field (link between source and frequency bands). Assuming a uniform distribution of magnetization inside the sources ensemble, for each area of interest the shallowest source was isolated from the deepest by a preventive spectral analysis. The maximum depth (Z_{HF}) of the high frequency sources was defined by applying Spector and Grant method (corrected by Fedi et al, 1997) to the power spectrum. The high-frequency sources lie between the bathymetric surface and a plane located at Z_{HF} depth. The low-frequency sources instead are confined between the Z_{HF} plane and the bottom surface of the magnetic basement. The two crustal domains were then divided into a prismatic set, through which their magnetization can be determined by a linear approach, since the relationship connecting the observed magnetic anomaly field $\mathbf{\Delta F}$ with the magnetization m of each single prism is linear

$$\Delta F_i = \sum_j K_{ij} m_j, \tag{7.1}$$

where the summation over index j expands the observed datum indexed as i at the superimposition of the contribution given by each prism. The magnetic field generated by a prismatic body derives from Bhattacharyya (1964)

$$K(r) = \frac{\mu_0}{4\pi} \int_v \nabla\nabla \frac{1}{|r - r'|} \cdot m \equiv \mu_0 T \chi H_0, \tag{7.2}$$

where μ_0 is the magnetic permeability, H_0 is the induced field, χ is the susceptibility and T is a geometric factor for a cuboid structure. The T factor is explained in detail in appendix A.

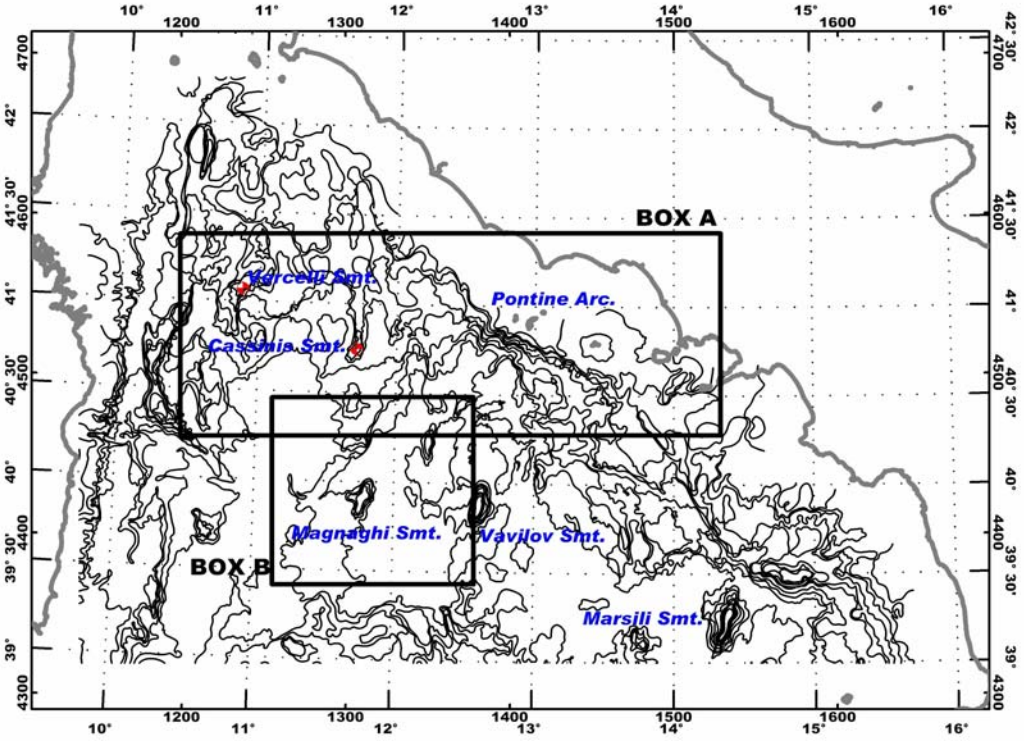

Figure 7.1: Bathymetry map of the Tyrrhenian Sea, the two black boxes define the studied area of the 2D inversion

The inversion procedure consists of a discretization of the crustal volume in a set of prismatic structures. We defined a prismatic cell mesh with a defined grid cell size compatible to the number of real data (for a CPU time computation), in which the mesh should be larger than the area of the anomaly studied. I used a Matlab routine (appendix B) to calculate the magnetic anomaly field generated by the prismatic set, and subsequently compared the recovered anomaly field with the real measured anomaly. The magnetization value is obtained through minimization of the sensitivity matrix M_s using a minimum quadratic norm.

$$\frac{1}{2}|M_s \cdot x - M_r|_2^2, \tag{7.3}$$

with

$$M_s \cdot x = M_r, \tag{7.4}$$

where M_s is the sensitivity matrix, M_r is the data matrix, x is the magnetization.

In the algorithm one can define the upper and lower magnetization values using a vector l_b and U_b, $L_b < x < U_b$ introducing the positivity of solution ($l_b = 0$). This inversion process was applied to different areas: the Selli Line- Magnaghi region (box 1 of fig. 7.1) and the northwest Campanian margin along the 41^{st} parallel (box 2 of fig. 7.1), and for each area a different prismatic model was used for the crustal portion being studied.

7.2 The apparent magnetization map of 41^{st} parallel zone

7.2.1 A geologic framework

The 2D inversion process was applied to the central Tyrrhenian zone, an area longitudinally extending E-W from the Continental Campanian Margin 14°30'to 10°30'and in N-S direction from 41°30'to 40°00'(fig. 7.2). This zone is characterized by the

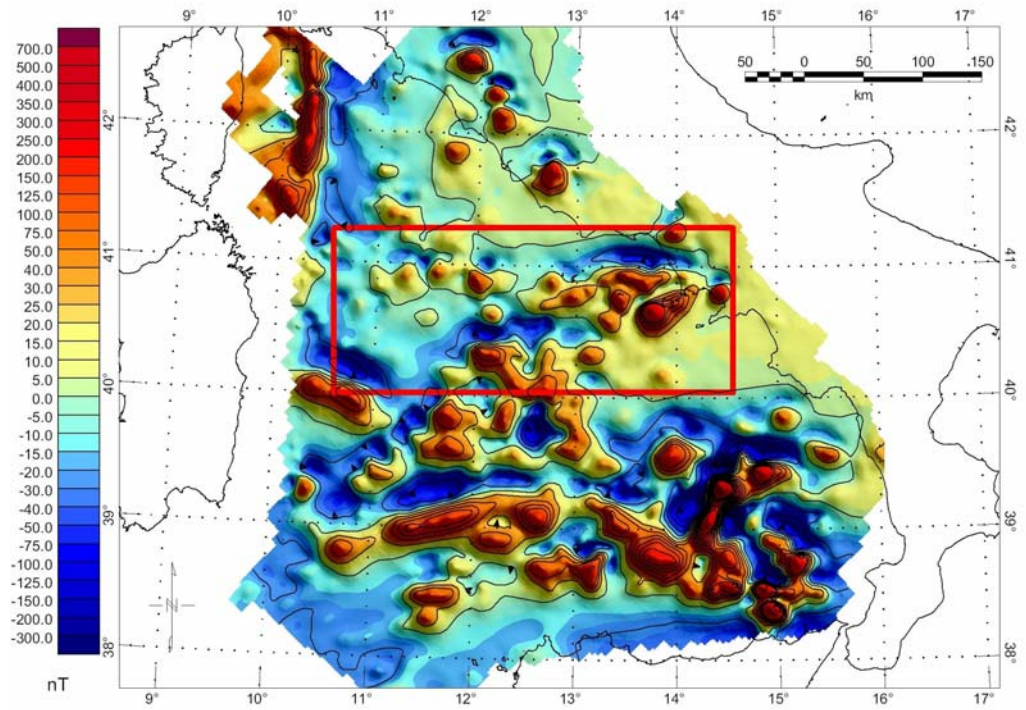

Figure 7.2: Map of total intensity anomaly field of Tyrrhenian Sea, the red box delimited the area object of inversion study

depressional structure of the Campanian margin, volcanic emerged bodies of the Pontine islands and the structural evidences of the Selli line. The Continental Campanian margin may be interpreted as a depressed morpho- structure extending NE-SW and bordered by NE-SW and SE-NW fault systems, and its structural setting is related to the Miocene-Pliocenic deformative phase (Bruno et al., 2000). Starting from the Miocene to Pliocene, the Campanian margin was deformed by a compressive movement which also generated strike-slip fault systems extending ENE-WSW (Hyppolite et al., 1994). Evidence of an extensional tectonic is given by several NW-SE normal faults dated late Pleistocene. On the Latium-Campanian margin, instead, the subsidence phase commenced during the Pliocene; this deformative action migrated in a SE direction during the Pleistocene with deposition of sedimentary units (Ippolito, 1973). In the offshore area are located several volcanic bodies such as Ischia and Procida islands, which are associated with the Quaternary volcanism of the Campanian region. Around the central-eastern portion of the 41^{st} parallel is located the Pontine archipelago, a group of islands which derive from Pliocene-Pleistocene volcanism, and whose products possess a chemism related to different magmatic sources. The presence of OIB-type rock and calc-alkaline products suggests the action of different geodynamic processes due to the fact that the subduction phase was complicated by an extensional movement (Cadoux et al., 2005). In its westward portion the study area is characterized by the Vercelli Smt, a Tortonian granodioritic complex. The 41^{st} area shows a complex structural setting generated by a multiphase evolution with superimposition of deformative events. In morphological terms this region shows a pattern dominated by the Campanian escarpment where the bathymetric level drastically decreases by 2000 meters. A number of morpho-bathymetric structures change their main displacement from E-W (near the Campanian coast) to NE-SW (central Tyrrhenian Sea) compatible with an anticlockwise rotation (fig. 7.3), and this feature agrees with a magnetization trend that connects the 41^{st} parallel zone to the Selli line region.

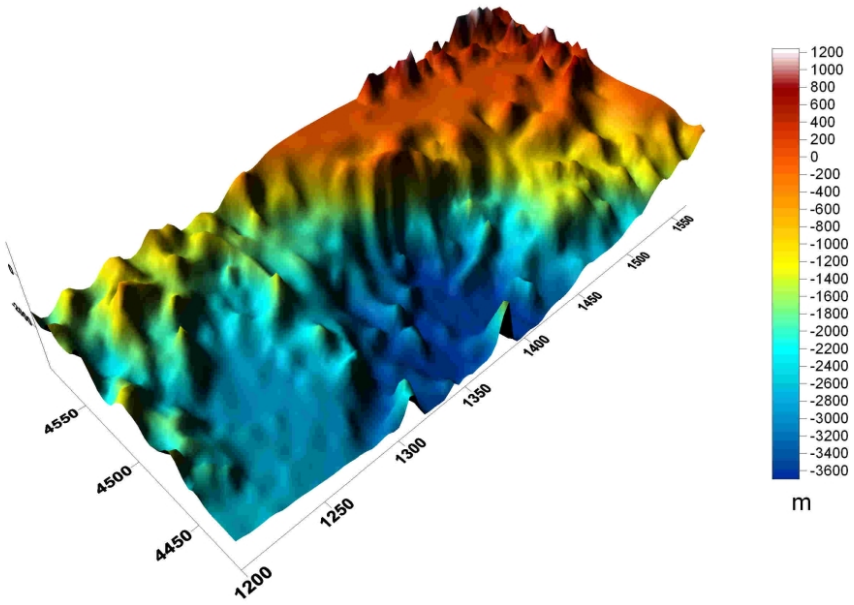

Figure 7.3: 3D surface of bathymetry of the Central Tyrrhenian area

7.2.2 The inversion model

The magnetic anomaly field shows a pattern related to the local submerged structure of the area, in which the volcanic edifices and intrusive complexes generate a high frequency magnetic signal, and this spectral contribution is superimposed on a high wavelength component of deep origin. In this area the magnetic basement is of considerable thickness, with a maximum depth of 20-22 km in the eastern sector. The quantitative evaluation of magnetic basement distribution was performed considering the ensemble of generating sources without an analysis of the shallowest local sources linked to the smaller volcanic evidences. In the actual analysis I also took into account the highest frequency sources. The radial power spectrum of the magnetic anomaly field shows a pattern well defined by two main families of magnetic sources. The slope of the spectrum changes at 0.026 Cycles/km corresponding to a wavelength of $\lambda = 37km$ (fig. 7.4). Since this wavelength divides the high-frequency sources domain from other deeper domains, it was from this cutoff-

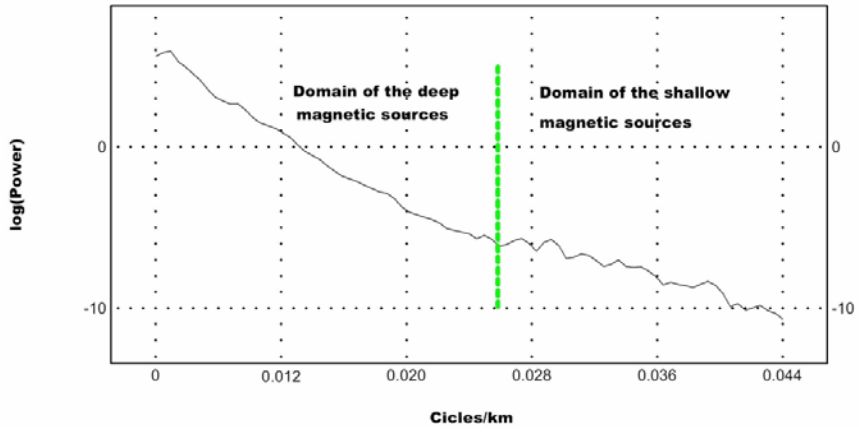

Figure 7.4: Radial Power Spectrum of the Central Tyrrhenian anomaly field, the green dashed line indicates the cutoff-wavelength

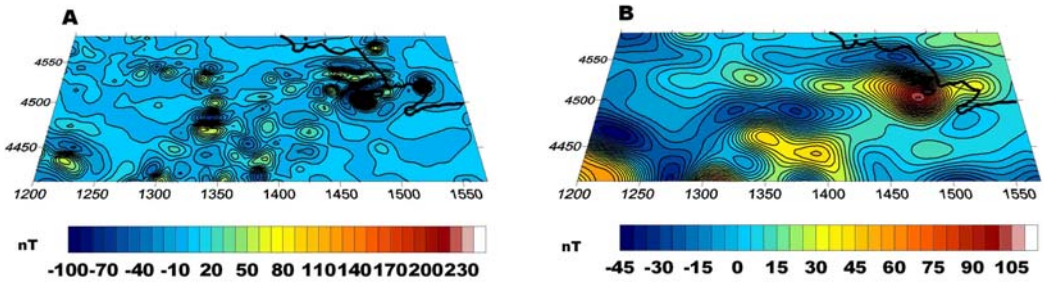

Figure 7.5: Low and High frequency fields of the Central Tyrrhenian anomaly pattern

wavelength value that I filtered the total intensity anomaly field of the study area to obtain the high and low frequency fields (fig. 7.5). The mathematical operator used for this operation was a Butterworth low-pass 8 order filter of Geosoft Oasis Montaj suite software that allows a smooth transition between high and low frequency bands. The low-frequency field shows two main directions of distribution of the anomalies: the first in an E-W direction related to the deepest intrusive source of the 41^{st} parallel, while the second is a NE-SW trending anomaly which places the eastern evidence of the 41^{st} parallel together with the magnetic structure of the Southern Tyrrhenian abyssal basin. The high-frequency anomalies show a scattered distribution without a clear connection with the area's geology. The Spector and

Grant method (after deconvolution for $\beta^{2.9}$, Fedi et al., 1997) suggested a depth of 8 km for this source ensemble. The prismatic model used to model the shallower sources is formed by the bathymetry surface as top and a horizontal plane located at a depth of 8 km as bottom. The low-frequency crustal domain was modeled by using a prismatic set defined at the top by the horizontal plane located at 8 km and at the bottom by the Curie isotherm surface (see previous chapter) (fig. 7.6).

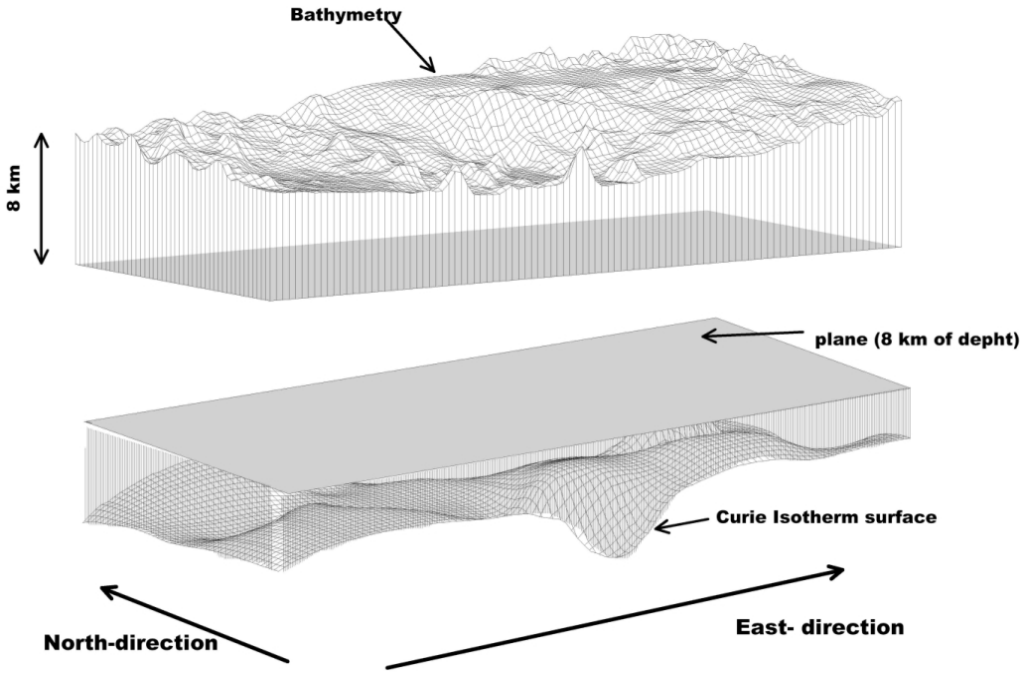

Figure 7.6: 3D vision of the prismatic model related to the high and low frequence source domains

Each prism forming the prismatic set has a square base measuring 2 x 2 km and an unknown magnetization value: the results of the two inversion phases can be seen in figure 7.7. For both recovered models a map of those vectors capable of underlining the main directions of magnetization distribution was elaborated. The vectors follow the directions given by the distribution of magnetization and a length proportional to the value of magnetization. The apparent magnetization of the high-frequency field shows a complex pattern of magnetic sources, with magnetization

values varying from -0.1 to 1.2 A/m. Observing this recovered model one can see a distribution of magnetization running NE-SW complicated by several isolated magnetic evidences.

The low-frequency recovered model shows a clear distribution of magnetic sources in which the magnetization values range from -0.1 to 0.6 A/m. The magnetization pattern is dominated by two main directions: a first (T1) running E-W along the 41^{st} parallel and a second (T2) oriented NE-SW and characterized by high readings (0.4-0.5 A/m). This high-magnetized trend connects the volcanic structures of the Gulf of Naples and the submerged edifices of the Central Tyrrhenian Sea with the Vavilov abyssal basin (fig. 7.7). The associated vector map illustrates this pattern clearly, in that connection of the longest vectors (highest magnetization values) produces the two main directions T1 and T2. These characteristics point out a magnetic structure able to connect the oceanic portion and the continental Campanian margin. The NE-SW magnetized trend is compatible with the deformation which occurred as the Southern Tyrrhenian opened. During the Pliocene an extensional movement occurred with a main NW-SE trending direction, and the crustal stretching and distribution of the main volcanic/oceanic structures (seamounts) show a NE-SW elongation compatible with the magnetized trend described above. In this context it is possible to associate the NE-SW magnetized pattern with the extensional phase, and the fact that the magnetization pattern involves a larger area than the oceanized region suggests a development of the rifting process in the deep crustal portion.

7.3 The apparent magnetization of the Selli-Magnaghi region

The Selli Line is a normal fault system located between two main crustal domains: the Sardinia continental block and the Southern Tyrrhenian oceanic crust. As pointed out by previous authors this fault system may be considered as the boundary between the "*northwestern rifted and southern oceanized areas*" (Van Dijk

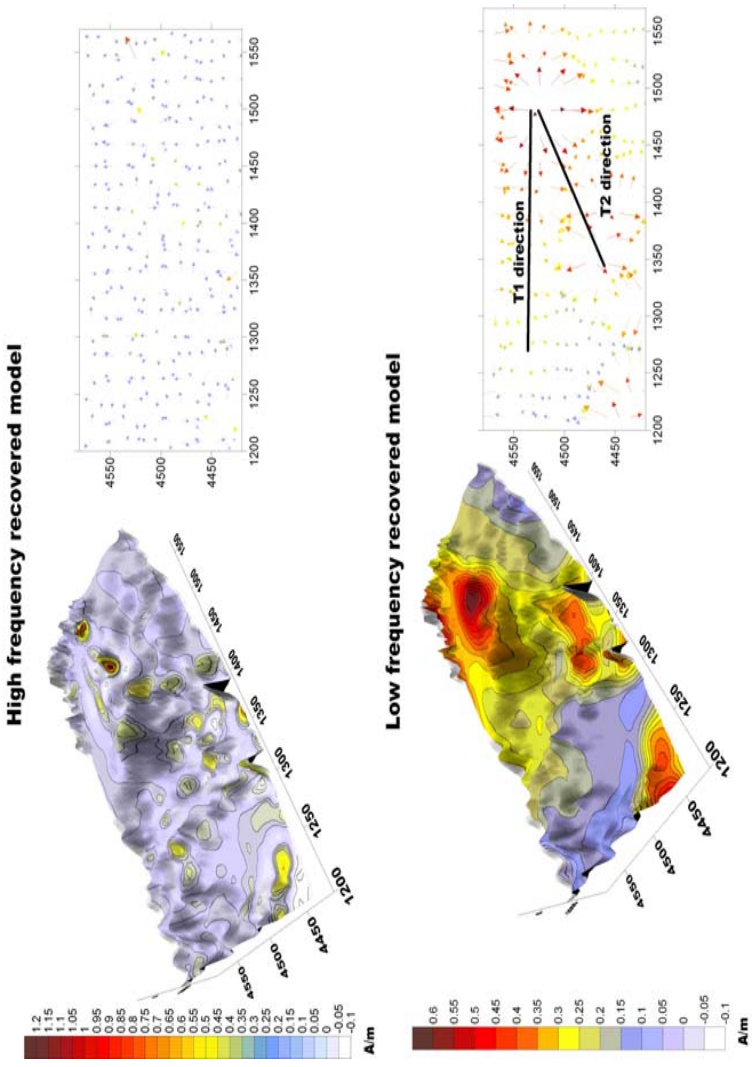

Figure 7.7: (A) High frequency recovered model by 2D inversion process; (B) Vector Map of the apparent magnetization of the high-frequency model; (C) Low-frequency recovered model; (D) Vector Map of the apparent magnetization of the low-frequency model

and Scheepers, 1995 and Finetti and Del Ben, 1986). The position, distribution and magnetic pattern of this structural element highlight features common to the 41^{st} parallel as analyzed in the previous subsection. Below the magnetic crustal evidences of this area are studied using a 2D inversion approach.

7.3.1 The Selli-Magnaghi region

The Selli-Magnaghi sub-region is located westward of the Central Tyrrhenian Basin. The quantitative analysis of the aeromagnetic data focused on the set of structural evidences located between the western rim of the basin delimited by a tectonic lineament known as the Selli line and the Gortani ridge bordering the western limit of the Vavilov Basin (Fig.7.8). The formation of this oceanic portion began during the

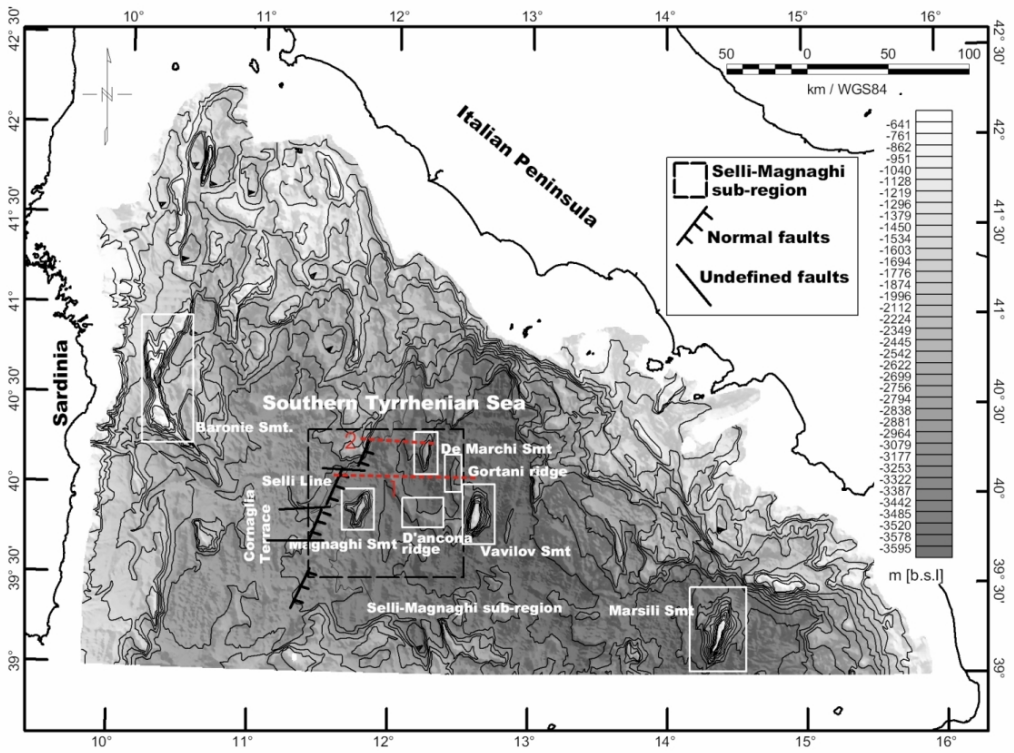

Figure 7.8: Bathymetry (*ismar-bologna, CNR*, contour line every 250 m) and main morphologic evidences of the Tyrrhenian Sea. The box enclosed by the dashed line shows the Selli-Magnaghi sub region subjected to the magnetic modeling; the red lines are the tracks of the seismic profiles

initial spreading phase of the Tyrrhenian Sea (Doglioni et al, 2004), while the roll-back in the Southern Tyrrhenian Sea started during the Late Tortonian (Malinverno and Ryan, 1986; Patacca et al., 1990), although the period when the Selli fault formed is not well defined. The submerged volcanic edifices of the abyssal western domain, such as Magnaghi and Vavilov, were generated from 3.4 Ma to 2.6 Ma ago (Robin et al., 1987; Savelli and Schreider, 1991), so if we consider a continuous evolution of the basin along a SE trend, we conclude that the origin of the Selli-Magnaghi sub-region started between the Messinian and the Late Pliocene.

The oceanic domain of the Magnaghi basin is separated from the Sardinia margin by the Cornaglia terrace, which consists of a N-S trended system of grabens originating during the Late Miocene rifting regime (Van Dijk and Scheepers, 1995). This structure represents a shallow portion of the passive margin of Sardinia, and has a flat morphology, with an average depth of 3000 m, in the area between the Baronie seamount and the Selli line (Sartori et al., 2004). The Selli line, which represents the very western border of the Central Tyrrhenian basin, consists of a NE-SW system of SE dipping listric faults interrupted by strike-slips of post-Tortonian age (Bigi et al., 1990). The Selli fault system dislocated large sedimentary portions of variable age from Post-Messinian to Quaternary, and is closely connected with sub-horizontal reflectors bounded by the Moho discontinuity level (Sartori et al., 2004). The main volcanic edifice of the region is the Magnaghi Seamount, which runs NNE-SSW at a depth ranging from 2800 m at its bottom to 1880 m at its top and whose lava products sampled as ODP site 650 show an alkaline-calc-alkaline basalt affinity (Serri et al., 2001). K/Ar dating of these samples also suggests that their age is 2.7-3.0 Ma, during the period of normal and reverse polarity C2A.1-C2A.2r as indicated by Schreider (1993). Near the Magnaghi seamount, in addition to the submerged volcanic structure Vavilov we find the ridge structures known as D'Ancona and Gortani.

The Gortani ridge show a N-S trend and is located westward of the Vavilov basin. This structural lineament is mainly characterized by igneous products of

MORB (Middle Oceanic Ridge Basalt) affinity as shown by ODP drills (ODP site 655) (Beccaluva et al., 1990; Serri et al., 2001). K/Ar dating (Leg 107) of the Gortani ridge shows a late origin of approx 4.3 Ma (Kastens,1988), and detailed magnetization samples have shown that its composition is the result of superposition of alternate positive and negative magnetized sources, compatible with magnetic polarity variations during its genesis (Gilbert Chrone, Cochiti and Nunivak sub-chrones) (Kastens, 1988).

The D'Ancona ridge instead is an arc-shaped structure located between the Magnaghi basin and the western limit of the Vavilov seamount. The nature of this structure has not yet been agreed on in literature: the most recent model proposed by Sartori et al. (2004) hypothesizes the D'Ancona ridge as a complex element of serpentinized mantle tectonically superimposed by thin intervals of stretched continental crust. The Selli-Magnaghi region thus shows distinct magnetic anomaly sources, and their modeling can suggest important information about the transition from a continental to an oceanic domain.

7.3.2 The magnetic pattern of the Selli region and its model

A clear evaluation of the magnetic properties of the Selli line requires observation of a larger area such as the Southern Tyrrhenian Sea, since this area presents very specific magnetic characteristics including those of the volcanic structures of the basin which show intense magnetic anomalies sometimes exceeding 300 nT. Some characteristics of the Tyrrhenian Sea are illustrated in the magnetic map in figure 7.9, especially the Vavilov and Marsili oceanic basins and the western limit of the Cornaglia terrace, which is characterized by a negative linear trend, and the Selli-Magnaghi sub-region enclosed by the box. The magnetic data was windowed to the box, tapering the border values with a Hanning window. Spectral analysis was performed by studying the slopes of the radial spectrum on a semi-log scale, as done by Spector and Grant (1970), following deconvolution of the power-law decay affecting the low-frequency domain of the spectrum (Fedi et al., 1997, Maus and Dimri, 1994). This analysis, as

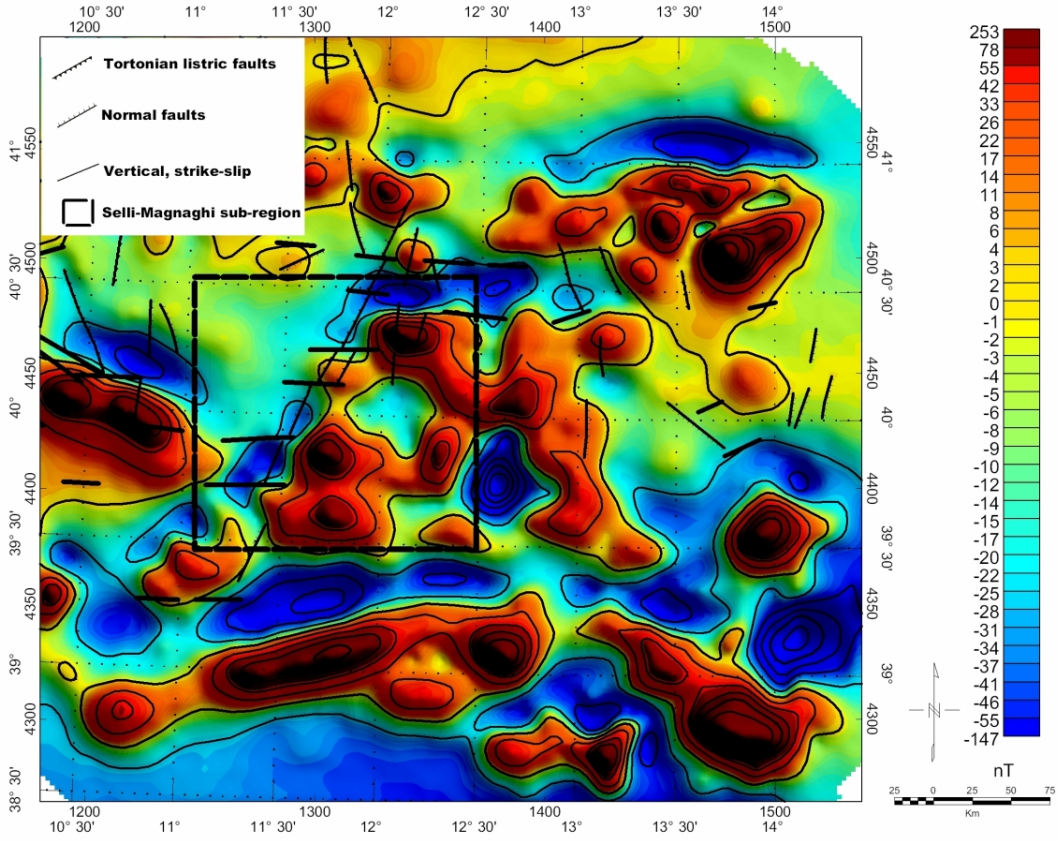

Figure 7.9: Total-intensity anomaly map (contour lines every 25 nT) and main morphological evidences of the Tyrrhenian Sea

shown in Figure 7.10, highlighted two distinct spectral domains separated by a cut-off wavelength of approx 25 km. The average depth-to-top of the Spector and Grant ensemble linked to the low-frequency field indicates a depth of 5.5 km. The inversion process was thus differentiated according to a prismatic model (fig. 7.11) in which we subdivided the crustal section lying beneath the magnetic anomaly field by using a double set of vertical prisms assumed to have uniform magnetization. The upper level is enclosed between the top corresponding to bathymetry level and the bottom given by a constant plane at 5.5 km depth, which spectral analysis has shown to be the average interface between deeper and shallower sources. The lower level of prisms, which aims to recreate magnetization distribution of the deepest sources, has

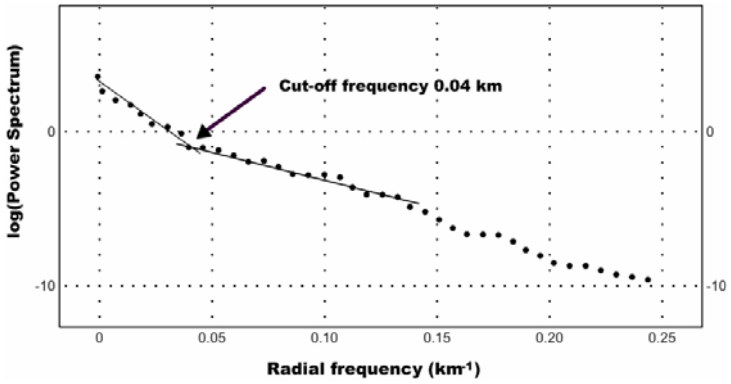

Figure 7.10: Radial power spectrum of the magnetic anomaly field of the Selli-Magnaghi sub-region

its top at the constant level of 5.5 km and its bottom at a constant depth of 10 km determined by the evaluation of the local depth position of the Moho discontinuity (Sartori et al., 2004). This approach allows us to create a magnetization model of the shallower sources by inverting the high-frequency magnetic anomaly, while the magnetization distribution of the deepest sources is obtained by inverting the low-frequency field. The data was filtered at the cut-off wavelength of 30 km by with a Butterworth filter. A grid of 50×50 square cells sized 2 km was extracted and the magnetization model was built by using the same number of prisms lying beneath each cell of the data grid. The magnetization was determined by a linear approach, since the connection between the observed recovered anomalies from the prismatic sources had previously been defined in the equations (7.1-7.2).

In this area the Curie isotherm is not well defined because the surface heat-flow distribution is affected by radiogenic contributions, intrusion components and convective effects (water circulation), therefore the associated heat equation is more complex than the equations given in chapter 6. For this reason, we chose the depth-Moho distribution as bottom surface. Although it is probable that the top of the upper prismatic crustal model should be corrected for the sediment thicknesses that are almost non magnetic, we were unable to find in any literature for the Selli-

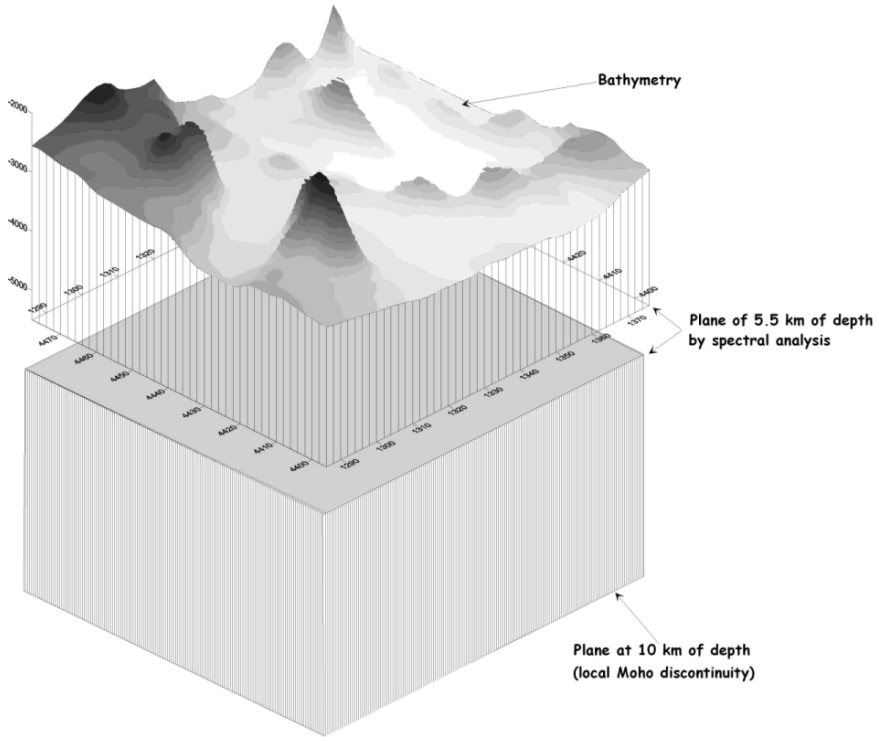

Figure 7.11: The prismatic model of the Selli-Magnaghi sub-region

Magnaghi sub-region a dataset able to describe these contributions with a resolution comparable with that of the bathymetric and aeromagnetic data. We however estimated that their contributions are not excessively influential, since the Tyrrhenian Sea is characterized by a regime with very thin crustal thickness and the outcropping volcanic structures are not covered with sediments. The magnetization model however is probably under-estimated since by introducing these effects we reduce the dimensions of the prisms, but we believe that our considerations on the shape and geometry of the sources will in any case be justified by the model.

Deepest sources from the low-frequency field

The low-frequency domain is associated with the spectral contribution of an ensemble of deep magnetic sources generated by the deepest geological features. By

evaluating the slope of the average radial power spectrum it is possible to locate the depth of the deep ensemble at approx 5.5 km. The study area is characterized by a strong depletion in crustal thickness related to an eastward roll-back movement following the oceanic stage. In this particular context it is possible to assert that the low-frequency spectral contribution is connected with the ensemble of the magnetic sources typical of the geologic-magnetic basement. Figure 7.12 shows the low frequency field (upper plane) and the relative apparent magnetization map (lower plane). The higher values of low-frequency anomalies are located on the Magnaghi structure, on the De Marchi Smt. and on the Vavilov basin. By evaluation of the general distribution of the low-frequency field it is possible to observe that the region of the Vavilov Basin and De Marchi Smt. is characterized by common deep magnetic features while the Magnaghi region shows a magnetic pattern which is unlike the general setting. The low-frequency contribution was inverted and the resulting apparent magnetization value was superimposed on the bathymetry. The magnetization values vary from -0.2 to 3 A/m.

The Magnaghi Smt. shows a deep magnetic source characterized by strong magnetization values (about 2.2 A/m) located under the volcanic structure. This source has an elliptic shape 40 km longitudinally by 25 km in latitude, and the shape of this source can be indicative of a basement structure connected to the Magnaghi basin where the volcanic edifice is superimposed. The Western region of the Vavilov basin shows a pattern characterized by positive magnetization with low values (0.6-0.8 A/m) heavily dislocated. The magnetic source of the Magnaghi area and of the Vavilov basin are connected by a similar distribution of N-S magnetization. Concerning the link between the oceanic formation and the magnetic sources, this magnetization pattern can suggest a common process of oceanic crust formation of these two basins.

Similarly, the De Marchi Smt region shows a distribution of high-value magnetic sources (approx 1.4-1.6 A/m) striking E-W. The geometrical features of this magnetic source pattern are closely connected with a unique tectonic setting dis-

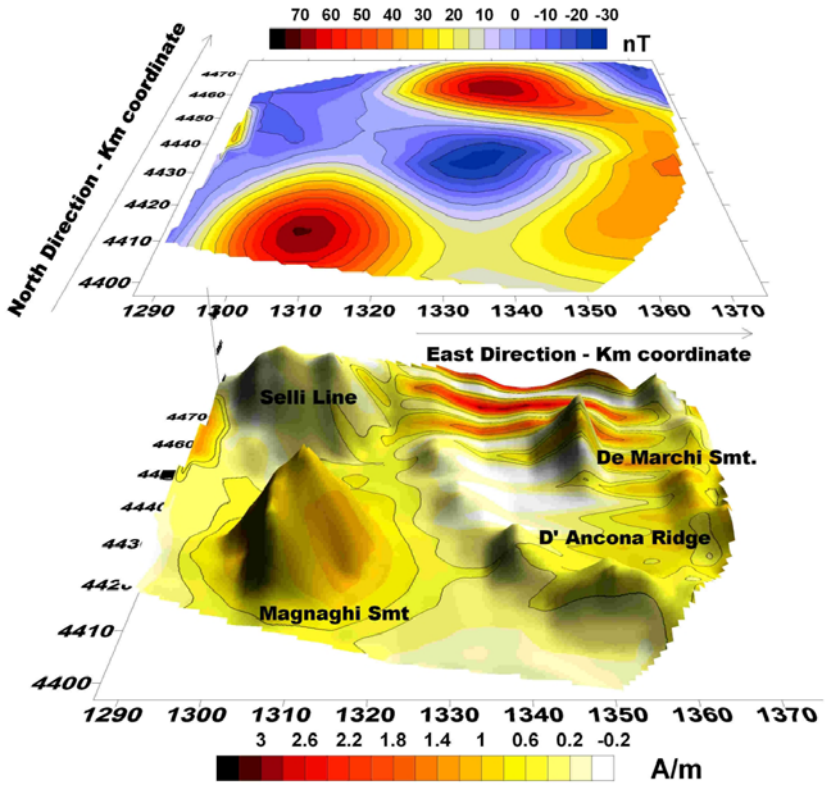

Figure 7.12: Low frequency field, contour every 15 nT; Apparent magnetization map of Selli-Magnaghi sub-region

tinct from the general setting. The De Marchi Smt is bordered to the westward by the Selli fault system, which is partially broken by several vertical faults with an E-W direction (Bigi et al., 1990). It is possible that the magnetic sources of the De Marchi region are dislocated by these E-W faults and that the E-W fault system may be associated with renewed activity of E-W tectonics after the formation of the Selli Line and during emplacement of the De Marchi Smt.

Shallowest sources from the high-frequency field

The contribution of high frequency is connected with convolution of the spectral density associated with every magnetic source located above the 5 km depth limit. The sources giving the high frequency field are all the shallower products such as lava flow of the sin-rifting process and portions of exhumed and serpen-

tinized mantle. The high frequency field and the relative apparent magnetization model are shown in figure 7.13, which illustrates the non-homogeneous distribution of magnetization with values ranging from -0.2 to 2 A/m.

The sub-volcanic structure of the Magnaghi Smt. shows two distinct magnetized areas located over the western and eastern sides of the volcanic edifice, with the western part giving magnetization values of approx 0.5-0.6 A/m in contrast with the lower magnetization of eastern side (0.1-0.2 A/m). This different magnetization pattern is the result of the chronology of its creation: the Eastern side of the Magnaghi Smt was formed during a magnetic field polarity inversion (Gauss' Epoch), and in all probability the low magnetization value is due to a convolution of some contribution of positively and negatively magnetized lithotypes. The western face instead was formed during a positive polarity stage of the main Magnetic field (Brunes). The high frequency model of the domain confirms the significance of volcanic products inside the Magnaghi basin and these magnetic features can be associated with lava flows or other effusive structures embedded in Plio-Quaternary sediment units (Sartori et al., 2004).

The structural setting of the area has been inferred by analysing two seismic profiles (Sartori et al., 2004) crossing E-W over the Selli Magnaghi area (profile-tracks in figure 7.8). The cross-section of figure 7.14 (seismic profile number 1) concerns the crustal features of the Magnaghi basin between the Selli fault and the Gortani Ridge. The magnetic anomaly readings (high frequency domain) and the relative magnetization values show a positive trend over the Magnaghi basin, and these features have confirmed the existence of effusive materials characterized by a magnetic signature which extends for kilometers. A second seismic profile located between the Selli fault and the De Marchi Smt (40°15'latitude)(fig.15) was analysed. The seismic section shows the existence of two lenticular seismic structures located in a shallower position under the synrift upper Messinian sequences, which are interpreted by Sartori et al.(2004) as volcanic intrusions. Both the magnetic anomaly and the magnetization were sampled along the seismic trace observing a

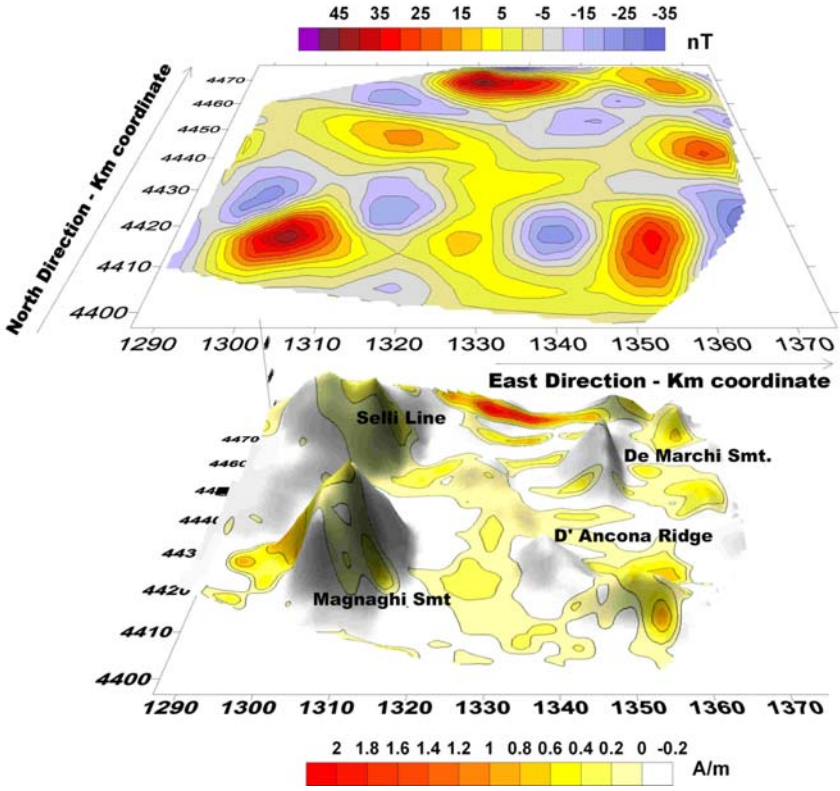

Figure 7.13: High frequency field, contour every 15 nT; Apparent magnetization map of Selli-Magnaghi sub-region

general positive trend of magnetic anomaly along all the seismic sections whereas the magnetization profile highlighted two positive peaks located over the two seismic bodies. These features confirm the volcanic-intrusive nature of the two bodies. The D'Ancona Ridge structure is characterized by several scattered magnetized sources connected to the high frequency band without a deep magnetic component. Since the lack of magnetic roots and an undefined shape of magnetic anomaly may highlight a different crustal nature, I believe that this ridge consists of a tectonically deformed portion of continental crust lying in a general oceanic basin.

7.4 Final model

The analysis of two distinct spectral bands has shown two distinct ensembles

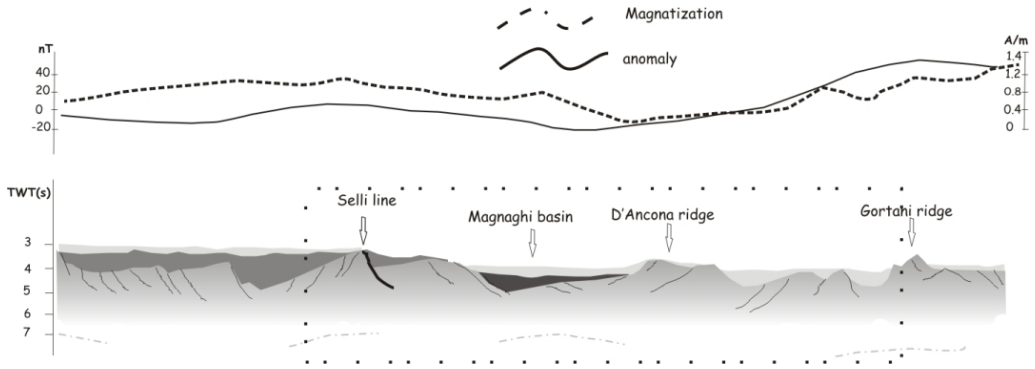

Figure 7.14: Seismic profile 1 (red-track in figure 7.8) related the crustal features of the area between Selli and Gortani ridge(after Sartori et al 2004)

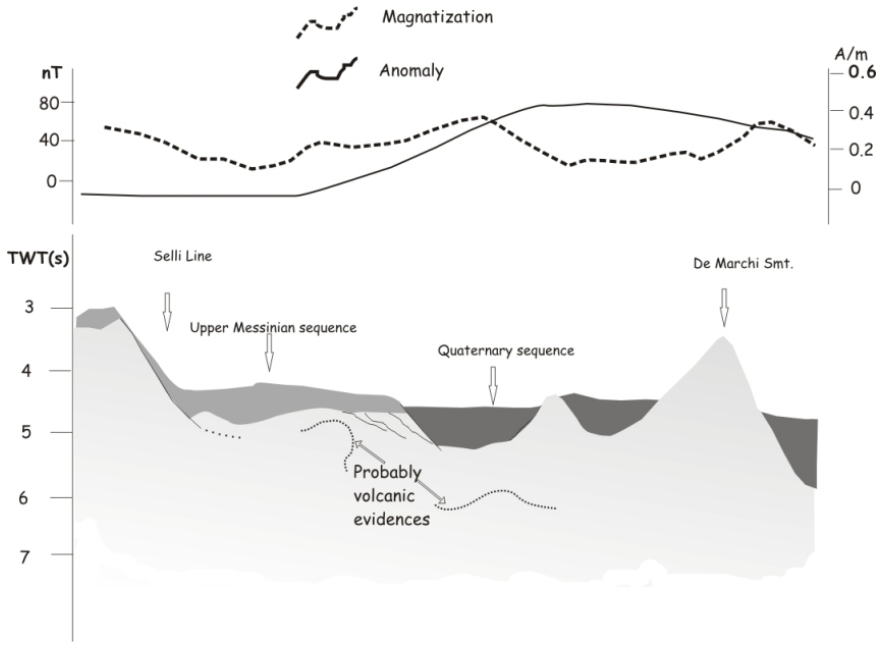

Figure 7.15: Seismic profile 2 (track in figure) related the crustal features of the area between Selli and De Marchi Smt.(after Sartori et al 2004)

of magnetic sources. The distinct signal for each spectral band was inverted to obtain two models, and the final model (fig. 7.16) was created by merging the two distinct models. On the same topographic base, three layers were plotted where the magnetic sources were differentiated by their depth. The first layer shows the shallower magnetic sources connected to the volcanic effusion of the sin-rift stage, while the second layer shows the deep magnetic body (depth $>$ 5.5 km) of the magnetic-geologic basement of the main sub-volcanic structures Magnaghi and Vavilov. The last layer shows the magnetic evidences not associated with the structures of the oceanic stage, since I consider these evidences as sources connected with the pre-rift geological setting such as structures of a pre-Tortonian basement and relics of Thetyan ophiolites (Sartori et al., 2004).

In conclusion, the Selli Line - Magnaghi region is an area where different crustal rocks are superimposed. The results of the 2D inversion suggest a magnetized pattern compatible with a crustal setting associated with the deformative structure of the rollback movement, with the Selli Line playing an active role in this phenomenon. The properties of the Selli region may be summarized as follows:

1. The Selli Line is a NE-SW trending normal fault system which divides two crustal domains, the Sardinia block and the southern Tyrrhenian abyssal basin;

2. The low frequency anomaly field is dominated by the submerged volcanic edifices Magnaghi and Vavilov. From a magnetic point of view the Selli fault system is the westward limit of the Magnaghi basin representing the starting point of a possible oceanic crust formation;

3. The shape of the Selli faults is complicated by several E-W vertical faults of unknown age (presumably post-Messinian). The magnetic domain associated with these E-W structures suggests their deep distribution in depth;

4. The magnetic pattern of the D'Ancona Ridge is compatible with a continental rotated crustal block lying in an oceanic basin. This evidence highlights a

crustal pattern typical of an extensional portion.

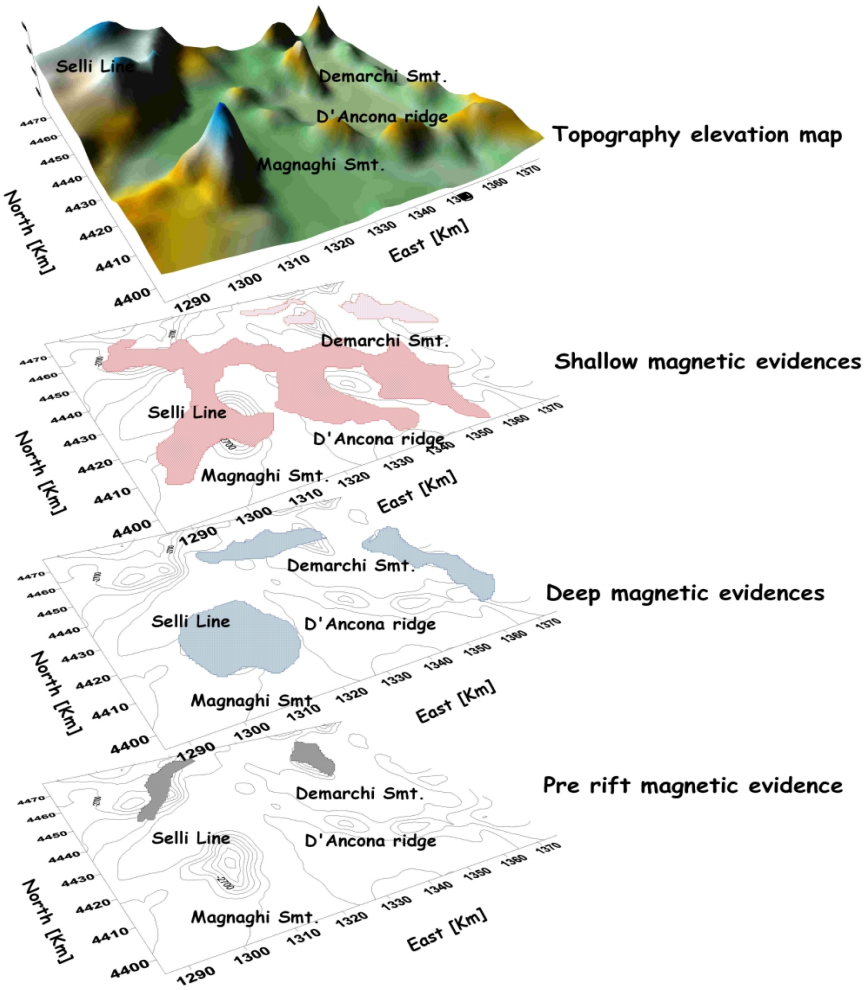

Figure 7.16: Final model of the magnetized structures of the Selli region. The layers are representative of different geodynamic stages

The 2D inversion process evaluated the bidimensional distribution of magnetization of the 41^{st} parallel area and the nearby Selli line region. The two zones show a different distribution of the total intensity anomaly field but a common low-frequency content. The inverse model of the high-wavelength component of the 41^{st} highlights a main NE-SW direction of magnetization connecting the continental structures to the abyssal oceanic features. Both the 41^{st} parallel zone and the Selli Line region

are characterized by a magnetic pattern extending E-W, a feature which may be indicative of a common deformative movement acting at different times. With the results of the inversions I was finally able to hypothesize a link between the two regions generated by opening of the Tyrrhenian sea. The 41^{st} and the Selli Line region are connected by a common NE-SW magnetized pattern suggesting a common deformative event which involved the two regions. Both these crustal structures played an active role during Southern Tyrrhenian Sea opening. To ascertain better geological and geophysical data both the regions will be subjected to a 3D inversion able to evaluate the depth distribution of the sources.

8 The 3D inversion process: methodology and synthetic tests

In this chapter we describe a new algorithm for inversion of 2D surface potential field data to create a 3D model of the physical parameters describing the source. Although this algorithm can also be tested on gravity data, in this study it was applied to the magnetic data in an application with which the solution of the inverse problem is obtained by using a depth-weighting function to regularize the sensitivity matrix. The main novelty of this method is a first-stage optimization that gives information about the depth-to-the-bottom (dtb) of the generating source. After completion of the inversion procedure, the algorithm was tested on some synthetic anomalies. Much of the information in this chapter comes from a new publication: **Caratori Tontini, F., Cocchi, L., Carmisciano, C.** 2006. *Depth-to-the-bottom optimization for magnetic data inversion: the magnetic structure of the Latium volcanic region, Italy. Journal of Geophysical Research.*

8.1 The DTB inversion algorithm

8.1.1 The inverse problem

The quantitative estimation of the physical parameters of the source generating an observed potential field anomaly is an inverse problem. Functionals relating a particular distribution of magnetic susceptibility or density to the observed anomaly are usually not analytically invertible, and furthermore, even after linearization, the number of unknowns often exceeds the number of observations. Inverse problems of this kind are characterized by instability and non-uniqueness of the solution (Tikhonov and Arsenin, 1977; Tarantola, 1987; Menke, 1989).

The theoretical or inherent ambiguity has been known since the Gauss' epoch as a trivial consequence of the Laplace equation (Blakely, 1995). Algebraic ambiguity is another major concern, since we follow the frequently used procedure which

consists of subdividing the region presumably containing the source into a set of prismatic volume pixels (voxels). The relationship connecting the density or magnetization of each voxel with the observed datum is thus linear and can be represented with a sensitivity matrix which, being always rank-deficient, has a multi-dimensional null-space. The solution to this problem is an affined vector space, in that a particular solution can be perturbed by a vector which spans the null-space of the matrix (also called its annihilator) without changing the resulting anomaly. A further experimental ambiguity is due to geological or experimental noise in the data, which always affects the resolution of the model and may generate spurious sources. The forward model may be unable to represent the source accurately. Think of a spherical source meshed by prismatic voxels, there is a problem of incompatibility of the system of equations rather than ambiguity. As a consequence of these ambiguities and incompatibilities optimal solutions may arise at any depth, which accounts for the widely-perceived notion that potential-field data lacks depth resolution and the inverse models are often represented by too-shallow solutions. In order to obtain realistic models it is necessary to introduce additional information, otherwise known as *a priori* information, in the statistical (Bayesian) sense, or as regularization in the meaning defined by Tikhonov and Arsenin (1977). It is interesting how these approaches have been interpreted as different alternatives (Scales and Snieder, 1997), yet they seem genuinely compatible under certain restrictive assumptions (Ho-Liu et al., 1989; Yanovskaya and Ditmar, 1990; Simons et al., 2002).

There exist several approaches that deal with the problems of non-uniqueness of potential-field inversion (Boulanger and Chouteau, 2001; Silva et al., 2001), such as minimization of the total volume (Last and Kubik, 1983) or of the moment of inertia (Guillen and Menichetti,1984) of the source, which allow creation of compact models by avoiding source dispersion. Barbosa and Silva (1994) instead obtained compactness along several axes by introducing *a priori* information on axis length. Caratori Tontini et al. (2003) developed a model based on the envelope of the source by using a set of 3D Gaussian functions. Fedi and Rapolla (1999) studied a multi-

layer 3D data-set, obtaining solutions at the correct depth by including the vertical variations of the magnetic field. In their very interesting paper Li and Oldenburg (1996) introduced a depth-weighting function to counteract the spatial decay of the kernel function with depth, giving increasing weight to voxels at increasing depths. Together with global smoothness constraints these authors obtained compact solutions and reduced the dispersion of the source along the three spatial directions, recovering thus a model with a *minimum structure*. Depth-weighting has given meaningful results and has been successfully applied to other inversion algorithms (Pilkington, 1997; Boulanger and Chouteau, 2001; Portniaguine and Zhdanov, 2002; Zhdanov, 2002; Pignatelli et al., 2006), since it allows the user to obtain solutions at the correct depths even in the case of vertically dislocated sources.

The new algorithm introduced in this chapter is based on Li and Oldenburg (1996) study. The vertical resolution is performed using a depth-weighting of the model norm without additional constraints in order to reduce to a minimum level the amount of re-required *a priori* information. This gives rapid access to first-order approximation solutions which can however provide important information on the susceptibility distribution, structural trends of the source and depth distribution, especially concerning bottom characterization. Depth-weighting alone however is unable to give a solution with a correct depth-to-the-bottom (dtb) of the source, therefore additional information is required. As far as we know, the exact introduction of the dtb parameter in the framework of 3D linear inversion has not been directly investigated by previous methods, while often the depth-to-the-top is accurately found as happens when using a standard depth-weighting distribution. Resolving the dtb however is important not only because it may define the magnetic basement, but also because it permits the definition of an appropriate mesh for inversion with the minimum vertical extension. The depth-shape distribution was modified by combining a depth-weighting function based on a power-law decay, with a function that allows closure of the solutions at the bottom depth. This also demonstrates that when the Tikhonov regularization is adapted with a meaningful

depth function, potential-field data can provide dtb information without imposing additional constraints or requiring further *a priori* information.

8.1.2 The inverse model

The organization of both data and voxels is crucial to achieve rapid regularization of the solution with a depth-weighting function. The observations (real measured data) were grouped in a column vector **d**, while the parameters that are the target of the inversion are identified by the vector **p**, which consists of the magnetic susceptibility of each voxel, within a 3D mesh-grid presumably containing the true source. The elements of the vector **p** are ordered in function of increasing depths, in the direction of the mesh layers. The linear forward model is expressed in the following equation

$$d_i = K_{ij} \cdot p_j, \tag{8.1}$$

where **K** represents the sensitivity matrix that expresses the contribution of a single voxel of the mesh to a particular observed datum. The column index j of $\mathbf{K_{ij}}$ indicates the contribution of the j^{th} prismatic voxel of the mesh to the i^{th} observation, i.e. the magnetic field generated in the spatial position of the i observation by the j prismatic voxel, as if the voxel had unitary susceptibility. This matrix is evaluated according to Bhattacharyya (1964), who derived analytical relationships for the magnetic field generated by a rectangular prism, as described in chapter 6. The induced magnetization was introduced into the algorithm procedure, which considers a geomagnetic field vector with the same direction as the source magnetization, a hypothesis which is well justified by the fact that many anomalies are generated by sources whose magnetization is induced by the actual ambient field. Alternatively, an average remanent magnetization direction must be properly evaluated and introduced into the sensitivity matrix (Helbig,1963; Claerbout, 1976; Andersen and Pedersen, 1979). Since the linear operator **K** has a multi-dimensional null-space, the solution requires regularization (Tikhonov and Arsenin, 1977). To this aim, the very useful set of Matlab routines developed by Hansen (1994)were adopted. The opti-

mal solution $\mathbf{P}_{opt}$ minimizes the misfit between the observed data and the anomaly generated by the model in a least-squares sense, with the additional constraint of also minimizing a particular regularizing norm:

$$\mathbf{P}_{opt} = arg(min\left\{|\mathbf{K}\cdot\mathbf{p}-\mathbf{d}|^2+\lambda^2|\mathbf{L}\cdot\mathbf{p}|^2\right\}), \tag{8.2}$$

where $\mathbf{L}$ is a square matrix whose dimension equals the number of unknown parameters. The Lagrange multiplier λ is taken to represent a compromise between data fitting and norm of the solution. Large values of λ generate very compact solutions at the expense of a large least-squares norm that indicates a poor data fit, instead lower λ values generate solutions which, while fitting the data very well, in many cases are far from the true model. The optimal λ value is obtained by the L-curve principle (Lawson and Hanson, 1974; Hansen and OLeary, 1993), which is a plot of log $|\mathbf{L}\cdot\mathbf{p}|^2$ versus log $|\mathbf{K}\cdot\mathbf{p}-\mathbf{d}|^2$: being L-shaped this curve has the optimal in a distinct corner which is the point of maximum curvature. Figure 8.1b illustrates an example of L-curve related to the inversion of synthetic anomaly (fig 8.1a), performed using $n = 400$ data. In proximity of the optimal $\lambda = 12.9491$ the least-squares norm χ^2 is 420, and thus the reduced least-squares norm (χ^2/n) is 1.05, which indicates a good fit. These results thus allow the interpretation of the optimal λ value as a good balance between data fitting and norm of the solution, giving a good result in terms of least-squares statistics. A common practice in inverse problems is to identify $\mathbf{L}$ with the identity matrix. This corresponds to finding the minimum L^2-norm solution of the linear problem. Li and Oldenburg (1996) showed that in potential-field inversion this is unsatisfactory since the solution tends to be clustered towards the top of the mesh, where low values of density or magnetization can fit the observed data very well. I designed a regularization matrix $\mathbf{L}$ which generates solutions at a consistent depth. Li and Oldenburg (1996) corrected the radial decay of the kernel by using an empirical function which simulates the decay of the magnetic field with depth, and following their principle I assumed a

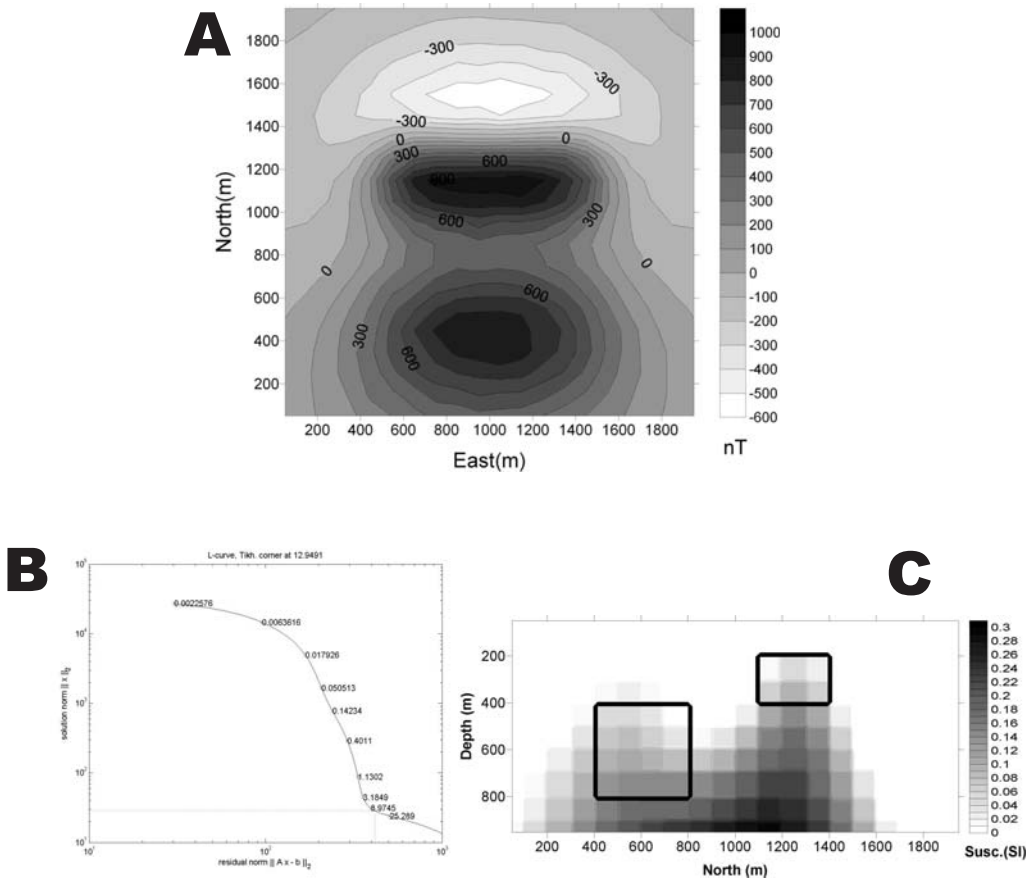

Figure 8.1: (A)Synthetic anomaly of two prismatic bodies; (B) L-curve of inversion of the anomaly; (C) result of the inversion process

diagonal shape for $\mathbf{L}$ so that

$$\mathbf{L}(z)_{ij} \equiv F_{reg}(z)\delta_{ij}, \tag{8.3}$$

whereδ_{ij} is the Kronecker symbol and F_{reg} indicates the function expressing the contribution of a horizontal layer of the mesh at depth z. The choice of F_{reg} is crucial to perform a process of inversion. The first order approximation of the function $F_{reg}(z)$ is

$$F_{reg} \approx \frac{z^{1.5}}{l_z^{1.5}}, \tag{8.4}$$

where l_z is the vertical extension of the mesh, and the depth z is measured from the top of the mesh to the center of the layer to avoid divergences in equation 8.4.

As shown by Li and Oldenburg (1996) the choice of the depth function is empirical and in particular the use of a greater exponent in equation 8.4 flattens the solution excessively towards the bottom of the mesh, without preserving the vertical ratios between depths of separate sources. Lower values of the same exponent instead produce too-shallow results. By using equations 8.3-8.4, $\mathbf{p}$ can be defined as

$$\mathbf{p} \equiv \mathbf{L}^{-1}(z) \cdot \mathbf{p}', \tag{8.5}$$

which emphasizes the deep layers of the mesh given the increasing values of $\mathbf{L}^{-1}(Z)$ with depth. Being diagonal and having non-zero values on the diagonal $\mathbf{L}$(z) is invertible, and equation (8.2) takes on the following form

$$\mathbf{P}'_{opt} = arg(min\left\{|\mathbf{K} \cdot \mathbf{L}^{-1} \cdot \mathbf{p}' - \mathbf{d}|^2 + \lambda^2 |\mathbf{p}'|^2\right\}). \tag{8.6}$$

This result is obtained by the following steps:

$$min\left\{|\mathbf{K} \cdot \mathbf{L}^{-1} \cdot \mathbf{p}' - \mathbf{d}|^2 + \lambda^2 |\mathbf{p}'|^2\right\} =$$

$$min\left\{|\mathbf{K} \cdot \mathbf{L}^{-1} \cdot \mathbf{p}' - \mathbf{d}|^2 + \lambda^2 |\mathbf{L} \cdot \mathbf{L}^{-1}\mathbf{p}'|^2\right\} =$$

$$min\left\{|\mathbf{K} \cdot \mathbf{p} - \mathbf{d}|^2 + \lambda^2 |\mathbf{L} \cdot \mathbf{p}|^2\right\}. \tag{8.7}$$

Equation 8.7 agrees with the results of Boulanger and Chouteau (2001) and Pignatelli et al. (2006), where the sensitivity matrix was directly corrected by multiplying it for a power-law function which increases with depth. I found the minimum $\mathbf{L}^2 - norm$ solution $\mathbf{p}'_{opt}$, and finally the correct vector $\mathbf{p}_{opt} \equiv \mathbf{L}^{-1}(z) \cdot \mathbf{p}'_{opt}$. Although in the case of vertically dislocated sources this regularization preserves the difference in depth, it is however insufficient, as shown by comparing figure 8.1a, in which the magnetic anomaly is generated by a source made of two prismatic bodies buried at different depths, with figure 8.1c where a vertical cross-section is shown to be northward oriented with the result of the inversion compared with the true sources. I have inverted 20 x 20 data contaminated by random Gaussian noise with a standard deviation of 3% of the data amplitude by using a mesh of 20 x 20 x

10 voxels centered under the anomaly. The solution obtained is far from the true model because the chosen regularization tends to put the maximum magnetization towards the bottom of the mesh. At this point, the regularization is corrected by applying a factor able to close the solution at the bottom of the mesh by following this relationship:

$$L^{-1}(z)_{ij} \equiv F_{reg}^{-1}(z) \cdot B(z) \cdot \delta_{ij}, \tag{8.8}$$

where function $B(z)$ should contain the DTB information. The choice of $B(z)$ is based on the preservation of the power-law decay of the regularization matrix at depths shallower than the dtb of the generating source, a property essential when seeking the correct depth-to-the-top ratios. Below the dtb of the generating source I should obtain instead a negligible solution. The function $B(z)$ should thus have a constant unitary value at shallow depths and should annihilate itself at depths greater than the dtb of the generating source. A possible form of $B(z)$ can be obtained through the Fermi function (Landau and Lifsits, 1977):

$$B(z) = \frac{1}{exp[(z^2 - z_0^2)/(\Delta z)^2] + 1}, \tag{8.9}$$

where z_0 represents the coordinate where the function halves its maximum value, with a characteristic thickness given by Δz. The parameter z_0 of the Fermi function is associated with the depth to the bottom of the source. The thickness $z \equiv z_0/2$ reduces the number of parameters, in that this choice is a good compromise between the step-behavior of the Fermi function and its smoothness and differentiability. The final version of the inverse regularization matrix is thus

$$L^{-1}(z)_{ij} \equiv \frac{z^{3/2}}{l_z^{3/2}\left\{exp[(z^2 - z_0^2)/(z_0/2)^2] + 1\right\}} \cdot \delta_{ij}. \tag{8.10}$$

By analyzing the behavior with depth z of the regularization matrix $\mathbf{L}$(z), expressed in equation (8.9), concluding that the *a priori* probability distribution function $\rho(p)$ is drastically suppressed outside the depth range defined by the Fermi function, i.e. for depths greater than z_0.

8.1.3 Synthetic tests

In this section some inversions of synthetic anomalies was performed, having established that the DTB parameter can be estimated in a stable way from the data. The choice of different DTB values allows the closure the solution at different bottom depths: larger Z_0 values generate deeper sources. Figure 8.2 shows the inversion model of the field generated by a synthetic source described by a prism at a given depth in the range $Z \in [300; 700]$ m. Different inversions have been performed by using different values of the DTB parameters. The mesh was made of 20x20x10 cu-

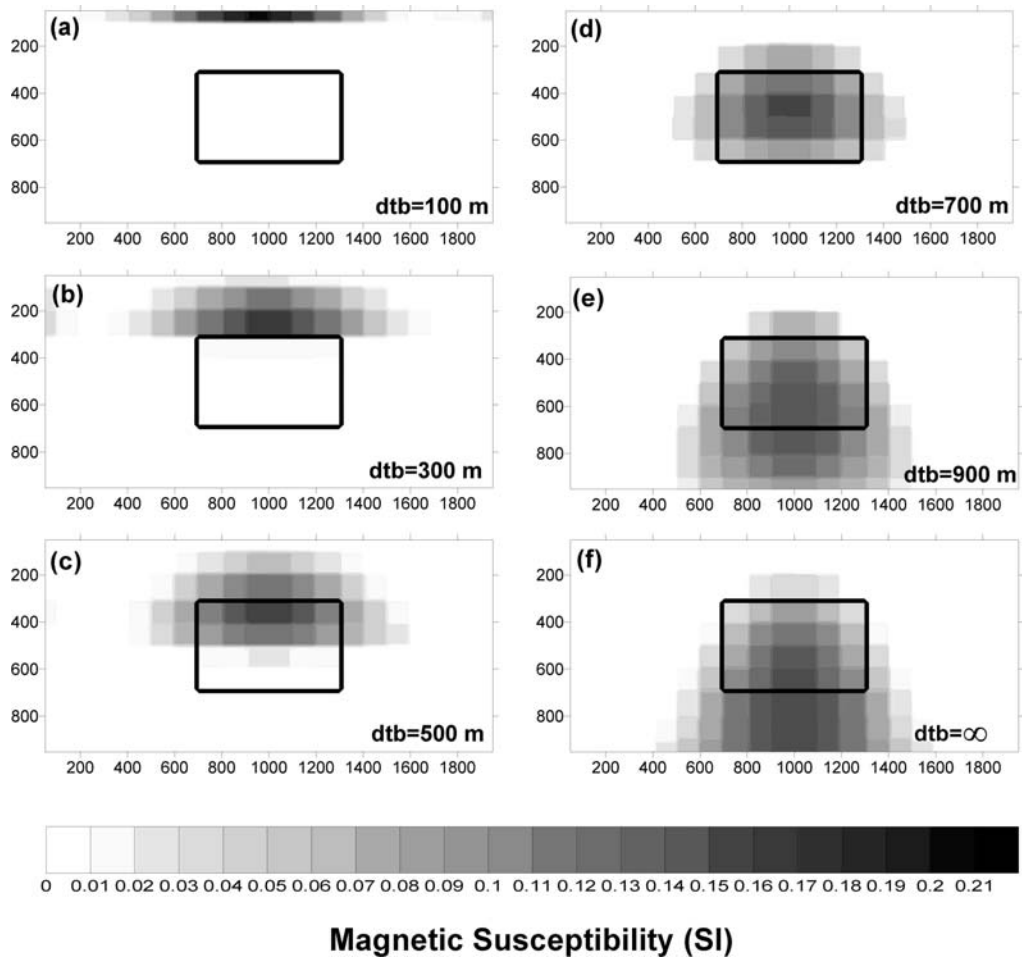

Figure 8.2: Results of inversions of the synthetic model of a prism buried at depth from 300 to 700 m. The solutions have been obtained at different values of DTB

bic voxels centered around the anomaly, with a cell size of 100 m and the data was again contaminated with random Gaussian noise. The solution of this inversion was placed at different depths according to the DTB values. The optimal DTB value, which is represented by the plots where maximum magnetization values are located inside the synthetic prism, is ideally situated around 700 m, in good agreement with the depth-to-the-bottom of the true source. The DTB parameter is also important in the definition of the optimal dimension of the mesh used to invert the anomaly data. While the horizontal geometry of the mesh can be decided by analyzing the horizontal shape of the anomaly, the vertical extension is more problematic since an optimal choice reduces the number of layers thus increasing the numerical performance of the inversion itself. A correct preliminary calculation of DTB values is the main goal of this inversion algorithm since the real inverse procedure, and thus the shape of the solution is based on the DTB value. I shall now describe the main steps of the inversion procedure:

1. Evaluation of the mesh grid dimensions able to contain the source;

2. Performance of a set of fast inversions with a regularization matrix with a Fermi function aimed at minimizing the N-norm of the solution in terms of Z_0.The optimal DTB is found as the Z_0 which minimizes the N-norm;

3. The final inversion is performed with the DTB obtained, which replaces Z_0 in the regularization matrix. The mesh-grid at this level can be redefined, for example by neglecting layers deeper than DTB and then increasing the number of layers shallower than DTB by reducing the thickness of the layer.

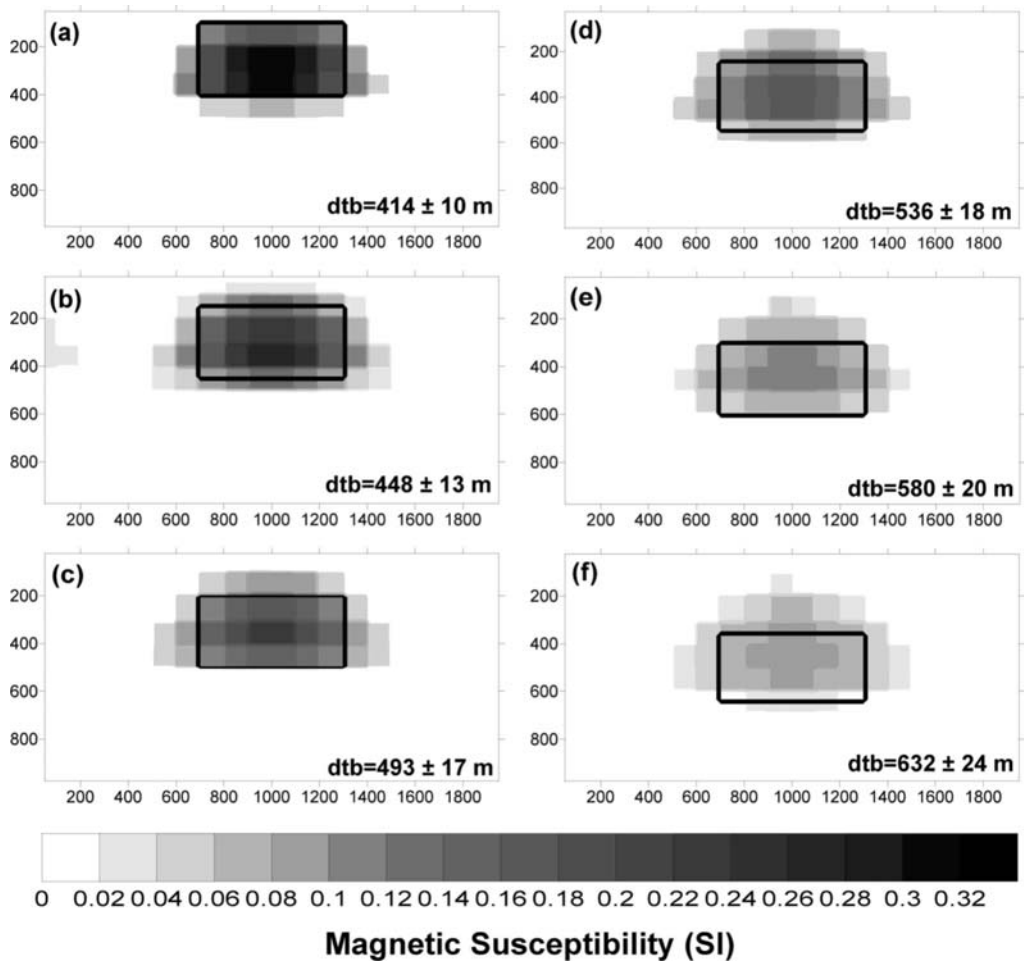

Figure 8.3: Results of inversions of a prism buried at different depth (400-650 m). The solutions have been obtained by using the DTB value previously estimated by the minimization of the N-norm

For a clearer explanation of this procedure I show the result of inversion of the same synthetic anomalies of figure 8.2 with defined dtb values. The prismatic body has a thickness of 300 m and its depth position ranges from 300 to 700 m. The previous evaluation of DTB value was performed at each position of the prismatic body to obtain a set of values of the bottom. The final result is shown in figure 8.3, where each source calculated is located inside the prism. The next chapter describes how this algorithm was applied to the real magnetic data of the 41°parallel zone.

9 The 3D inversion of the 41^{st} parallel zone

Previous chapters have explained the rationale behind of the inverse problem and its application in a number of synthetic tests. This chapter illustrates application of the 3D inverse algorithm to observed magnetic data in a measured dataset while introducing a greater number of parameters in the analytic process such as natural noise and a scattered distribution of the anomalies. In these terms, the inversion of real data can be performed after a precise constraint of the mesh and the number of data. The result of the inversion process is a set of horizontal slices and X-Z and Y-Z cross sections able to define in all three dimensions the distribution of magnetization. This 3D inversion focused on the 41^{st} parallel and Selli-Magnaghi region and the models created of the two areas show a peculiar distribution of magnetization where the development of the magnetic source is influenced by their crustal setting.

9.1 The 3D recovered models

The previous bidimensional inversion of the magnetic anomaly field has shown a link between the E-W 41^{st} area and the nearby Selli-Line Magnaghi sub-region. Since it can be seen that the two areas share a common NE-SW magnetized trend linking the continental Campanian margin to the oceanic structure of the Southern Tyrrhenian sea, which suggests a deep crustal structure displaced in a NE-SW direction, I apply the 3D inversion process to obtain a clearer picture of the deep structures of these two areas. The aim of this study was also to evaluate the vertical development of the generating sources and their geometric relationships. The first model considers the magnetic lineament along the 41^{st} parallel and subsequently the magnetic pattern of the Selli Line region is examined. Figure 9.1 shows the areas studied through the 3D inversion algorithm.

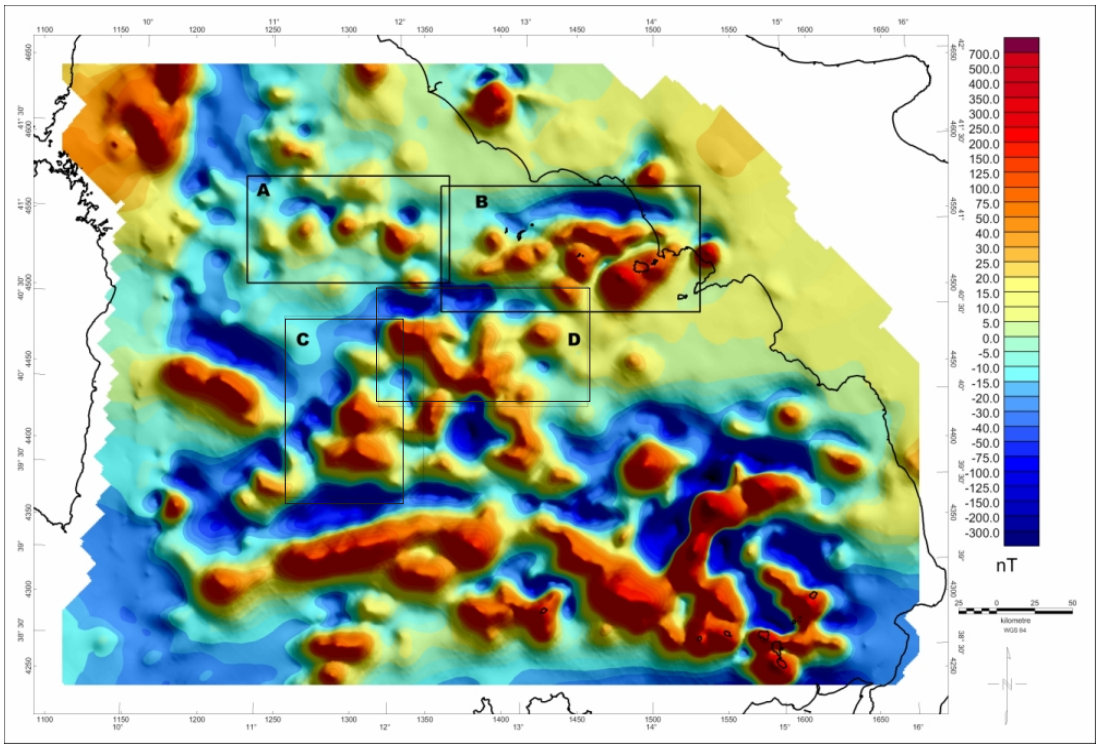

Figure 9.1: Vision of the areas object of 3D inversion

9.1.1 3D Model of the 41^{st} parallel

The depth-distribution model of the magnetic sources of the 41^{st} parallel divides this area into two distinct western and eastern sub-regions (respectively boxes A and B in figure 8.1). The western area (Box A) is a region of 7000 km^2 (100 x 70 km) extending from 40°30'to 41°15'and longitudinally from 11°00'to 12°10', characterized by a E-W lineament consisting of three magnetic anomalies. As previously described these magnetic anomalies are not related to the morphology, but are instead centered on a system of N-S striking structural lows. Northward of this area lies the submerged structure of the Vercelli seamount, which is considered an intrusive body with a grano-dioritic chemism imposed about 7.5 My ago (Tortonian),(Barberi et al., 1978) and which shows a N-S distribution with its top located at a depth of 50 meters. The western portion of the 41^{st} parallel is magnetically characterized by

a low-frequency anomaly pattern running E-W, on which are superimposed three high-frequency anomalies with amplitudes of 75-100 nT. Since this lineament introduces similar magnetic characteristics to those of the Vercelli, I may assume that their buried magnetic sources are also intrusive structures of the same nature, which would suggest that these magnetic sources were emplaced during the Tortonian in the initial phase of the rifting process. Currently available literature does not contain geological information regarding these evidences, therefore the 3D inverse model would appear an important tool for the interpretation of this area. In practical terms, the 3D inverse algorithm was applied to these three anomalies as a single ensemble (case 1) and subsequently as individual anomalies (case 2). Interestingly the two approaches provided different information: case 1 provided an overall vision of the deep structure pattern with an evaluation of a common geometry between the varying sources, whereas the individual analyses gave a clear vertical development of the sources with information about the possible rotation of the structure.

The area of interest was then modeled using a prismatic mesh of 30x30x15 cells (X,Y and depth directions) with 700 real data items, in an overall mesh size able to contain the three magnetic anomalies. As described in the previous section, the inversion process uses two separately-staged algorithms: the first providing a DTB value and the second plotting the depth distribution of the source. In the first stage the DTB analysis gave a maximum depth value of 14 km, which is in agreement with the local bottom distribution of the magnetic basement (16-18 km) obtained with a thermal model (see chapter 6) and with the Moho depth (20-22 km, Nicolich, 2001). The actual inversion phase was thus constrained by means of this DTB value, and the result is a tridimensional distribution of the magnetization from the surface to a plane located at a depth of 15 km. For a better definition of the model, an integrated view of a number of horizontal slices computed at different depths, X-Z and Y-Z cross-sections was performed. Figure 9.2 illustrates the X-Y planes at different depths. The distribution of magnetization shows a closure at a plane of 15-16 km as suggested by the DTB analysis. The depth distribution values differ for the three

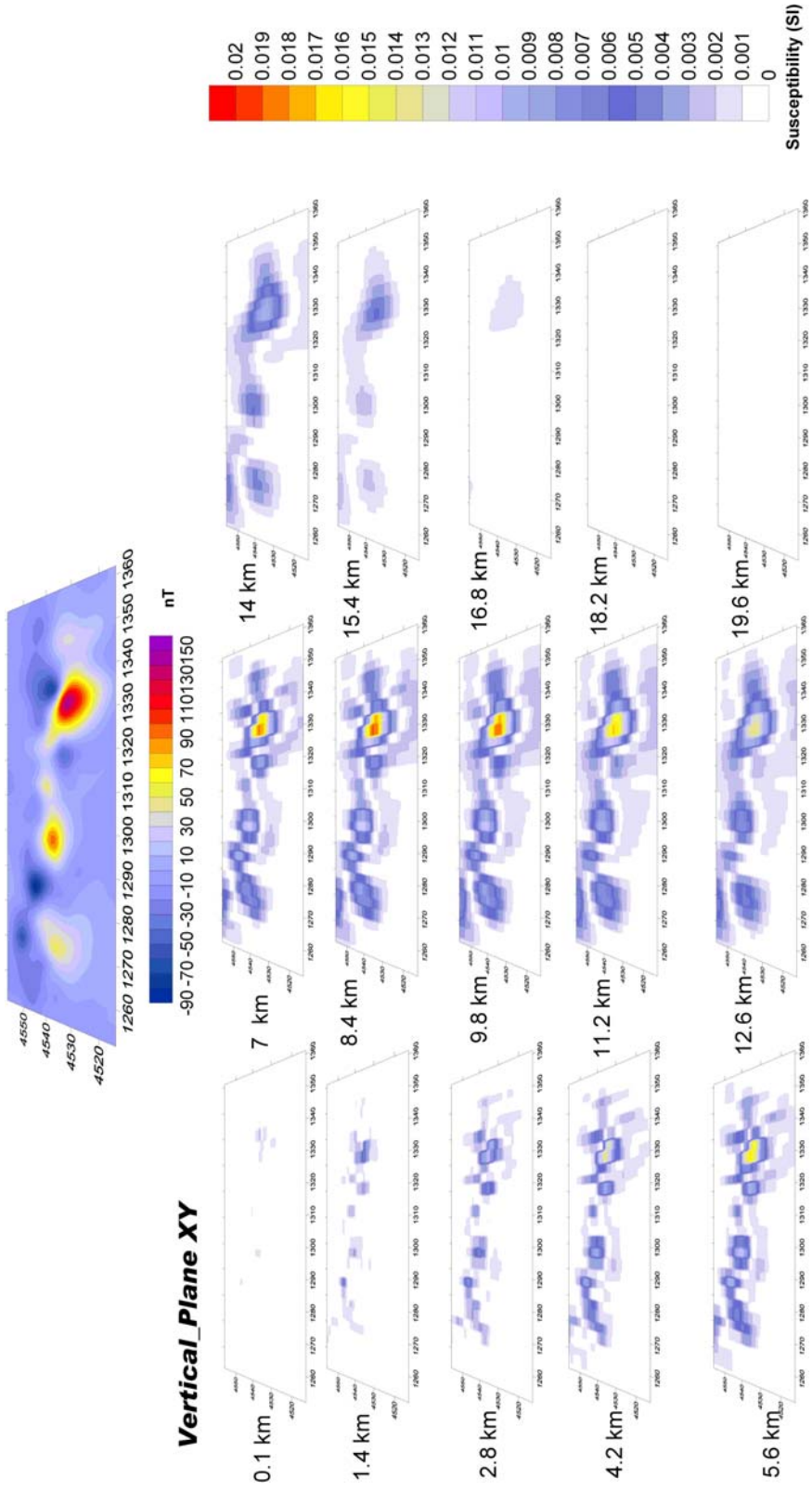

Figure 9.2: The recovered model of three anomalies ensemble, horizontal cross-section

anomalies: the eastern and western anomalies show bottom closures at 14-15 km, whereas the central anomaly closes at 11 km. The maximum value of magnetization is located on the planes at 8-10 km. On the shallower planes the geometry of the sources is closely connected to an E-W lineament. The vertical distribution of the sources ensemble shows a common shape and a common dimension. Generally speaking the model of a magnetic anomaly shows a magnetization that becomes larger at deeper locations, this behaviour being caused by the weight of the low-frequency component of the signal; in our case study however this effect was not observed. This could suggest that the shape of the sources is bounded by a peculiar crustal setting that has obstructed the northward and southward growth of the sources with a preferential development E-W. I have drawn an envelope of sources at the shallower plane which matches the source distribution of each X-Y plane (fig. 9.3). The latitudinal development of the magnetization can be observed on the X-Z cross-sections, which are slices spaced every 3.5 km. The different shapes of the generating sources may be caused by the different cut of the sources by the X-Z plane, however only those section cutting at the center provide an accurate description of the body. The sources have an oblique pattern with an asymmetrical development (fig. 9.5). Towards the depth to the surface it is possible to observe a large distribution which becomes smaller. At a km-coordinate of 4530-4540 the magnetized body decays abruptly with a point of boundary corresponding to the 41^{st} parallel, and this behaviour is visible on different sections. The abnormal shape of the source may be generated by a structural element capable of obstructing the lateral growth of the source. This boundary extends along the study area with a E-W trend and is also portrayed structurally by the X-Z sections.

The model shows magnetic bodies buried in a confined crustal portion with a N-S dimension of 20-30 km where the presence of an E-W striking vertical boundary is compatible with a vertical fault system or contact between two crustal blocks.

As the model of the three-anomaly ensemble is not able to throw light on the development of each source, the three anomalies were inverted separately (Fig. 9.6).

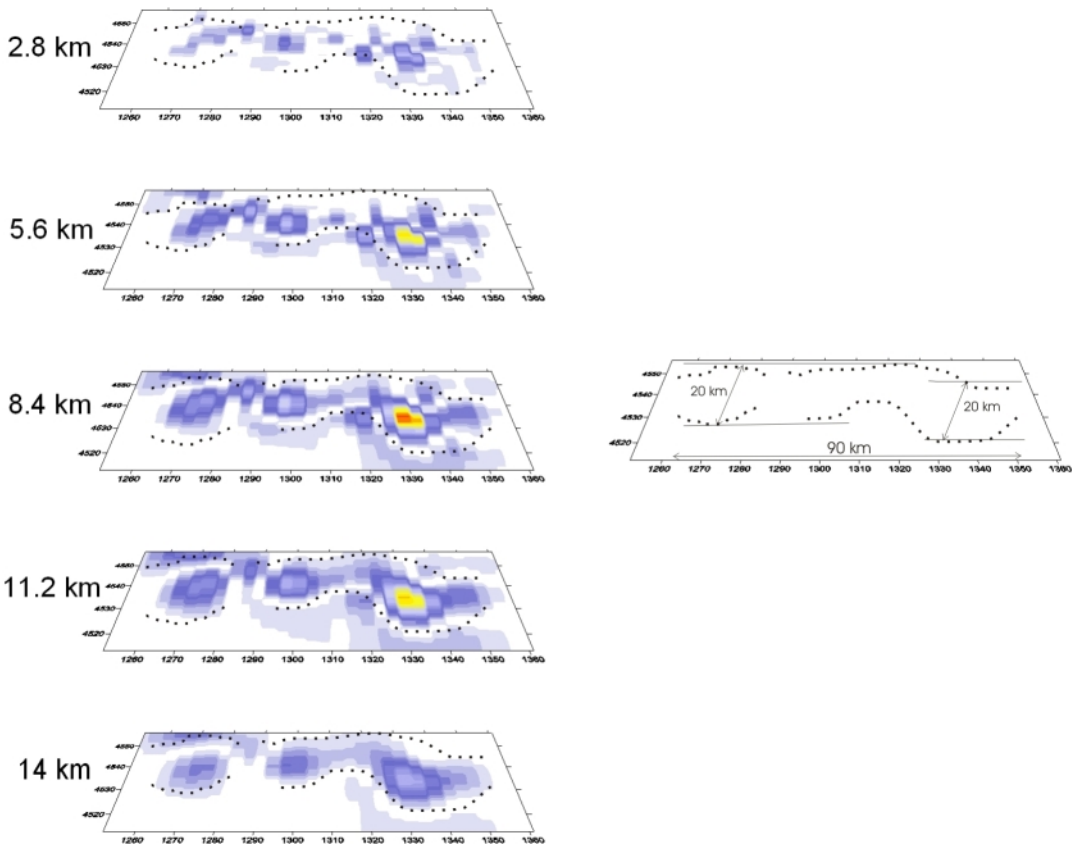

Figure 9.3: Particular of figure 9.2; evaluation of the shape and dimensions of the sources

The magnetization distribution agrees with the previous model in that the three distinct sources show a bottom closure at 14-15 km. The western magnetic anomaly model shows an unusually shaped generating source, where the magnetization closes at a depth of 13 km. Again, the geometry of the source changes with the decrease in depth, and at the deeper plane the magnetization pattern shows a main E-W direction (plane 6-13 km). Above this 6 km plane the body has a NE-SW direction. The amplitude of the azimuth increases for the surface planes, this behaviour being compatible with a anticlockwise rotation of the magnetized structure possibly due to a local E-W movement of the crustal domain. The change in geometry may be due to a different stress rate along the vertical portion, creating a diversified source during the active phase of the 41^{st} discontinuity. If I assume that these buried structures had

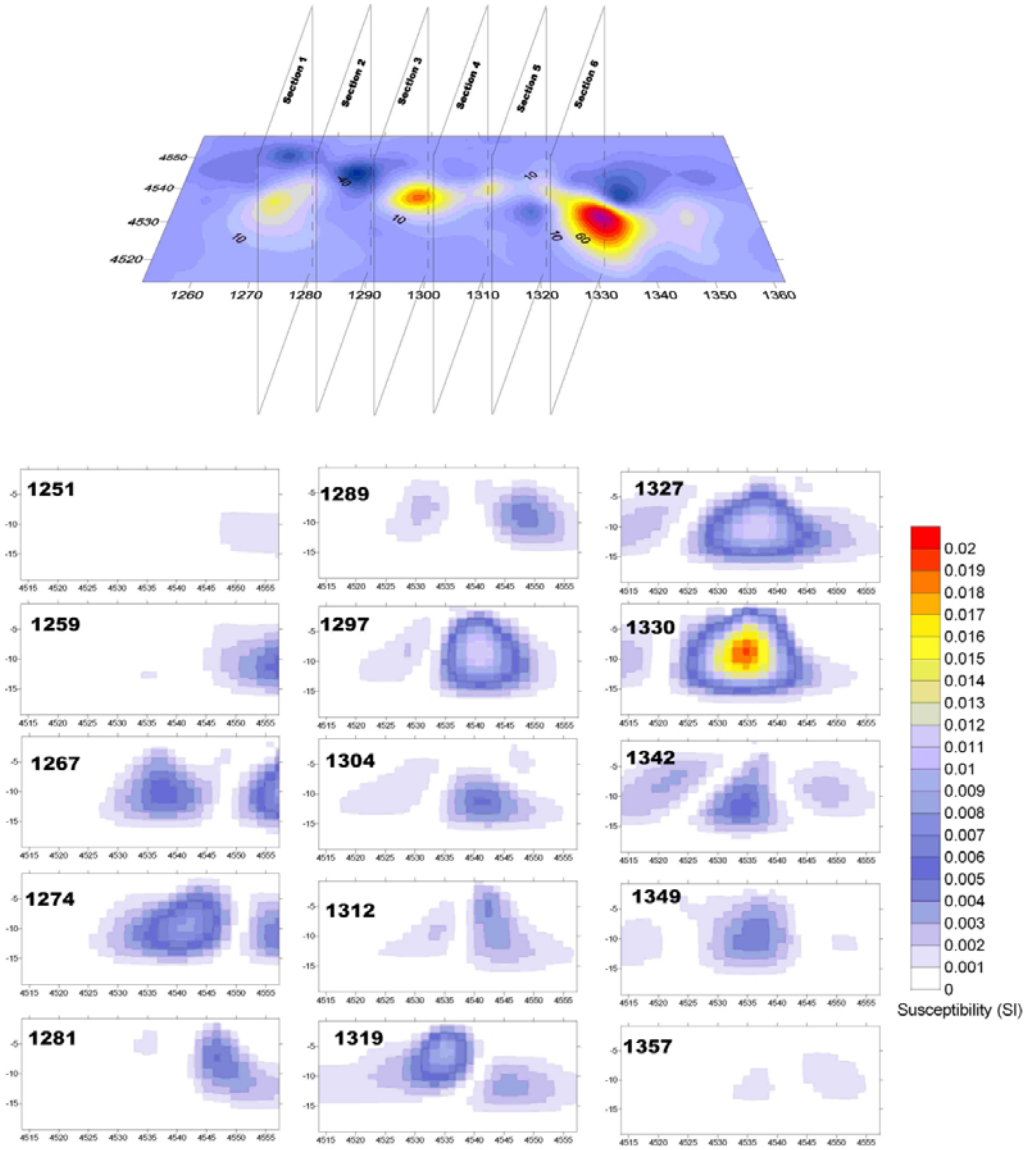

Figure 9.4: X-Z cross sections of the inverse model of figure 9.2

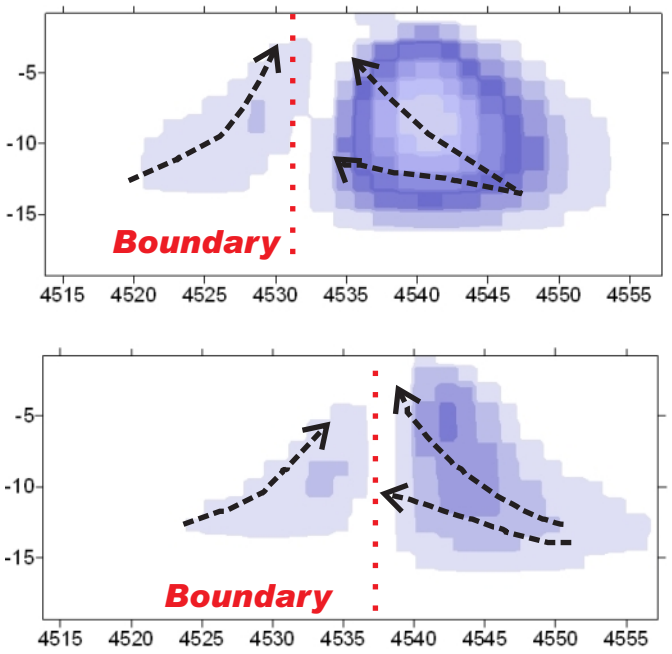

Figure 9.5: Particular of figure 9.4, two X-Z sections with the position of the supposed crustal boundary (red dashed line)

the same evolution as the Vercelli, it is plausible to date them as Tortonian, which means that the western portion of the 41^{st} parallel was active during the Tortonian.

The eastern portion of the 41^{st} (box B figure 9.1) shows a magnetic pattern connected to high frequency anomalies generated by volcanic evidences. This area contains emerged structures of Pliocenic-Quaternary calc-alkaline volcanism such as the Pontine islands and islands of the Central Campanian Province (Serri et al., 2001), and its anomaly field has a main E-W alignment with a NE-SW distribution as secondary component, a magnetic pattern which may indicate overlapping of two distinct contributions. For study purposes the ensemble of anomalies belonging to box B was modeled using a mesh of 30x30x15 voxels after inverting approx 900 real magnetic data. The DTB analysis highlighted a source closure at a depth of 21 km, which agrees with the crustal and thermal settings of the area, while the bottom of the magnetic basement is located at 24-25 km. Figure 9.7 shows this model. Along the vertical direction the plotted sources change their shape, showing a scattered

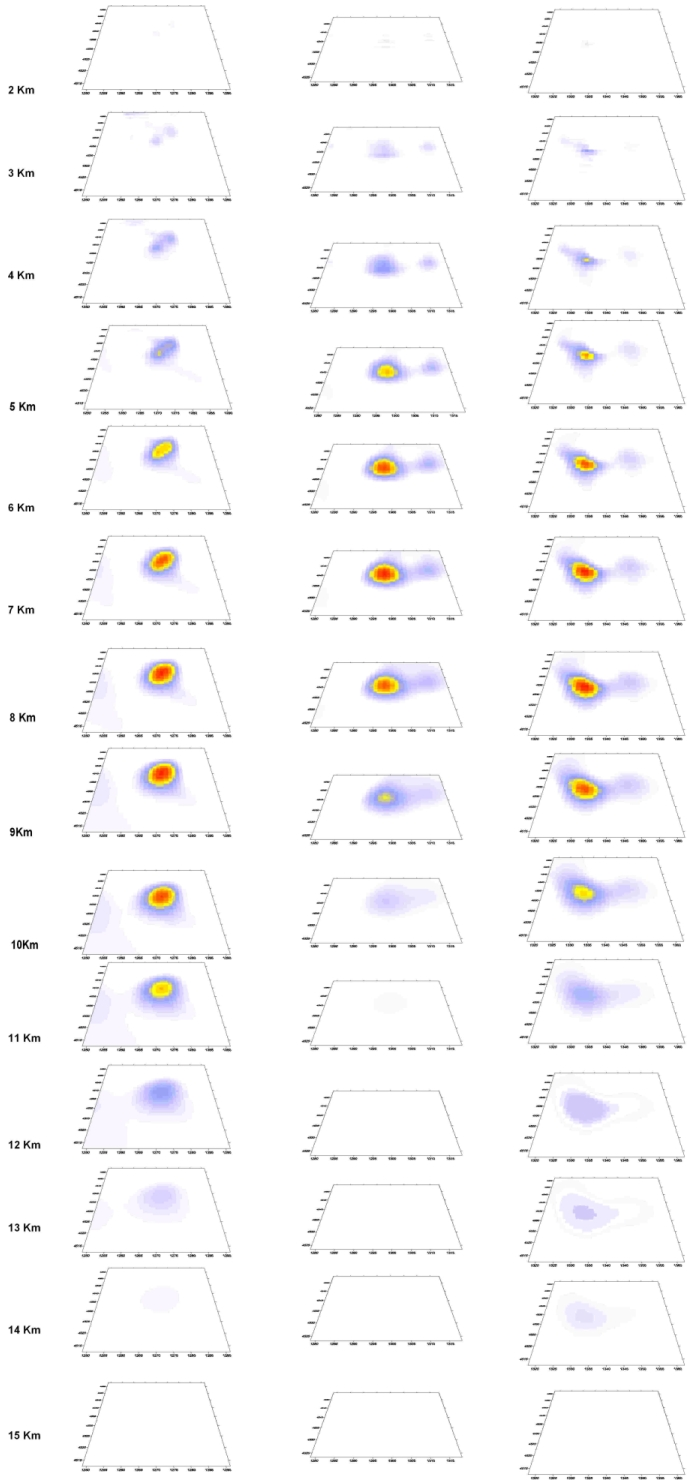

Figure 9.6: Horizontal cross-sections of the three distinct anomalies

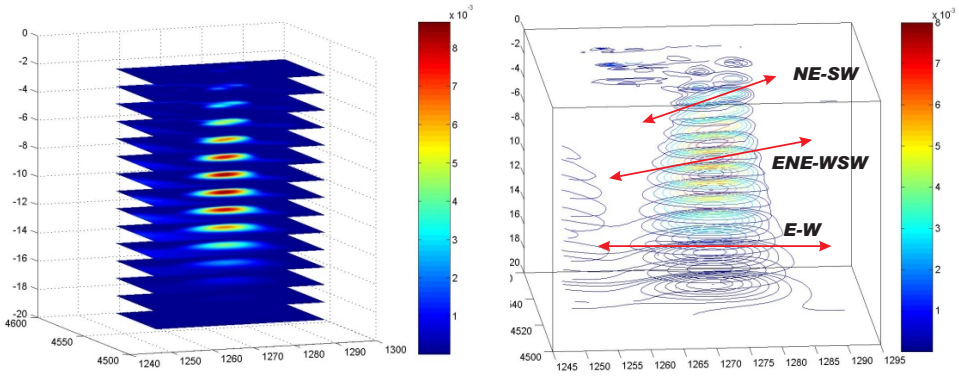

Figure 9.7: 3D model of the western magnetic evidence of Box A; on left side, 3D color full slices vision, on the right side, 3D contoured slices vision

distribution at the shallower planes where the structure rises up. Starting from the plane at 11 km of depth the shape of the source is dominated by two main magnetization trends running E-W and NE-SW. This dual magnetic pattern disappears in the last plane (about 21 km) where the magnetization shows only an E-W trend. The two distinct ensembles of sources are associated with two main magnetic patterns with the E-W component deriving from the activity of this discontinuity and well correlated with the magnetization of the western portion of the 41st parallel zone. The NE-SW magnetized pattern instead may be related to superimposition of E-W and NE-SW magnetic components. The general E-W magnetic pattern is affected by an oblique component due to a NE-SW structural element such as the Selli line, and observation of the displacement of the Selli Line points to a close relationship between this structural element and the NE-SW magnetized pattern. The western portion of the 41st shows a magnetic feature closely related to two distinct geodynamic settings: firstly the E-W movement which has generated a lineament of magnetic sources along the parallel, and secondly a NE-SW deformation due to the Southern Tyrrhenian Sea opening. The X-Z cross sections highlight the compact shape of the source, thus confirming the range of depth distribution (2-20 km) suggested by the DTB analysis (fig. 9.8). In some X-Z cross-sections, the

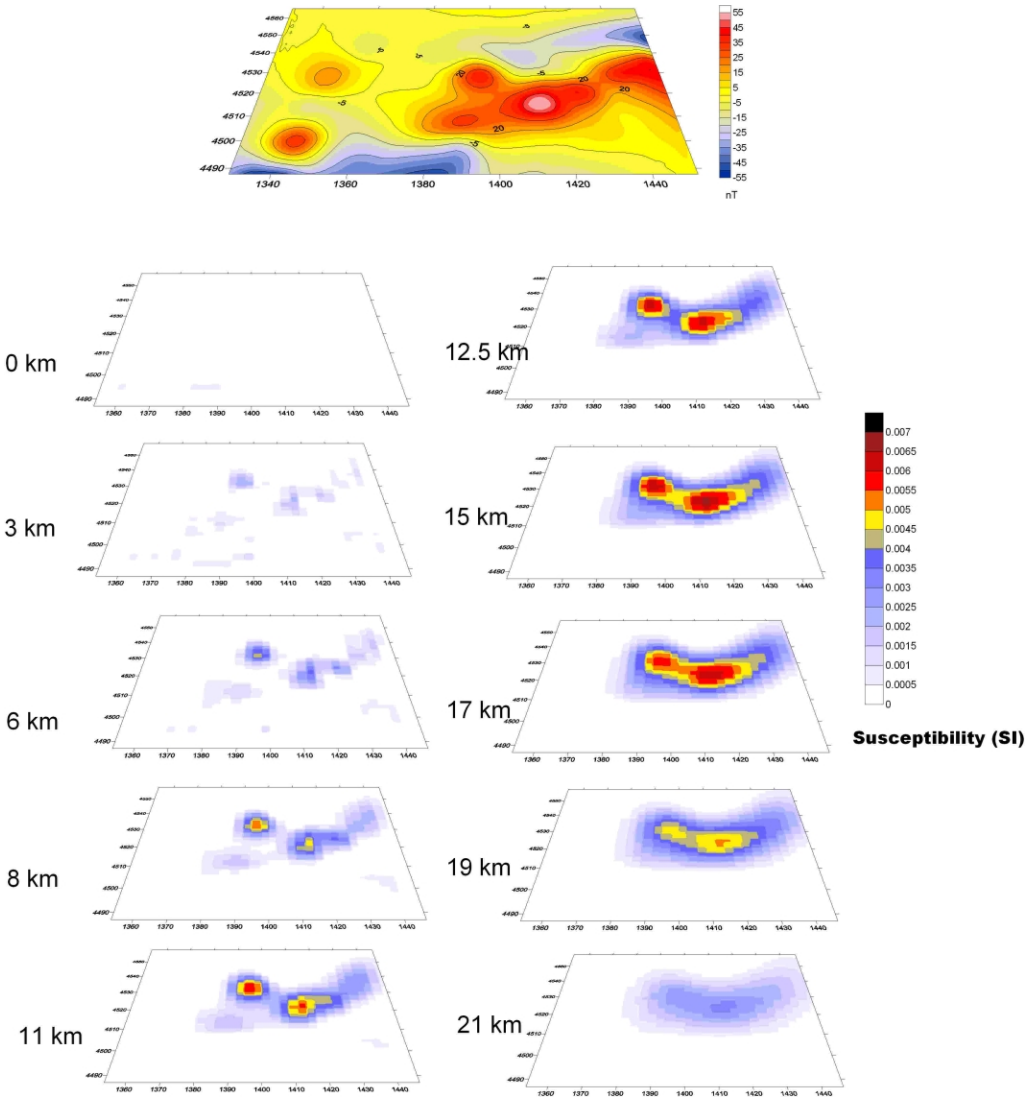

Figure 9.8: Inversion of magnetic anomalies of east portion of 41^{st} parallel (box B in fig. 9.1), horizontal cross-sections

source has an abnormal shape with an oblique development similar to the geometry previously observed in the box A model. The growth of the source is stopped by a boundary located at a well defined coordinate. In this case the geographic position of the boundary is not centered on the 41^{st} but is shifted southward by 20-30 km. As shown in Figure 9.9 this last feature may suggest a non-linear displacement along the 41^{st} of the vertical structural boundaries. The N-S shift of the presumed 41^{st} discontinuity occurs in a zone with a low magnetic anomaly density. The magnetic evidences of western 41^{st} domain are separated from their eastern counterparts by a small area characterized by low-frequency contributions without shallow sources. This area divides the two magnetic domains along the same E-W alignment, as can be seen from a global model of the buried sources of the 41^{st} which shows two well-defined separate magnetic patterns (figure 9.10). The western domain is dominated by small, isolated shallow sources (with 13-14 km maximum bottom depth), while conversely the eastern portion is characterized by an ensemble of sources with a more complex geometry and a bottom depth of 20-21 km. The two domains are separated by a zone containing no sources. Observing the thermal state of the 41^{st} parallel, the depth of the Curie isotherm increases between the two magnetic domains (figure 9.11), and this variation of the thermal state suggests a different crustal structure between the western and eastern portions of the 41^{st}, thus confirming the complex setting of the study area. The fact that the 41^{st} parallel divides the Northern and Southern domains also suggests a crustal differentiation along itself.

9.1.2 3D Model of the Selli Line region

The inversion process applied to the magnetic anomaly field of the 41^{st} parallel zone has highlighted particular information on the crustal features of the area. In particular the model of the eastern portion of the parallel shows an abnormal magnetized pattern connected to a source ensemble oriented NW-S, and this result indicates the usefulness of a quantitative analysis of the magnetic source of the Selli line and its neighboring areas. In concrete terms, the 3D inversion procedure was focused on the

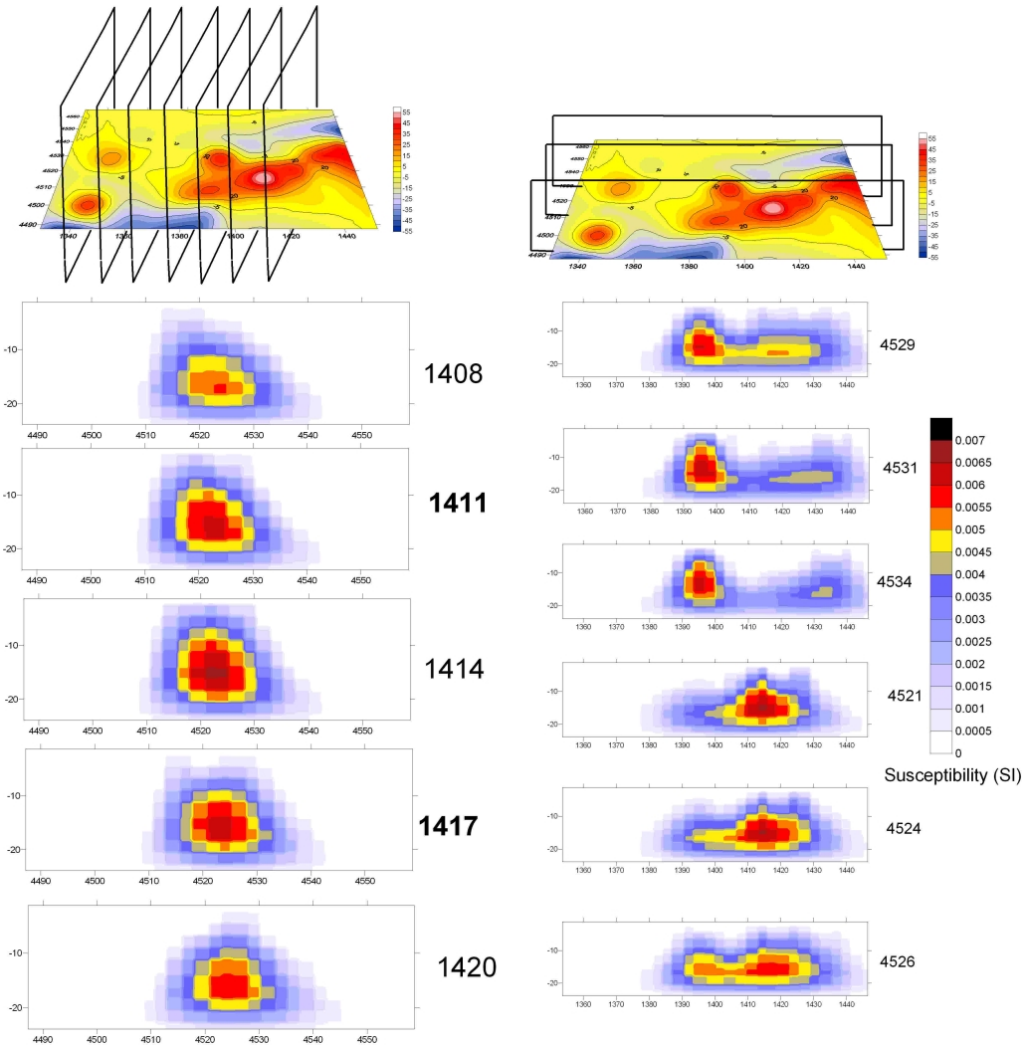

Figure 9.9: Global vision of the X-Z and Y-Z cross sections of the model of figure 9.7

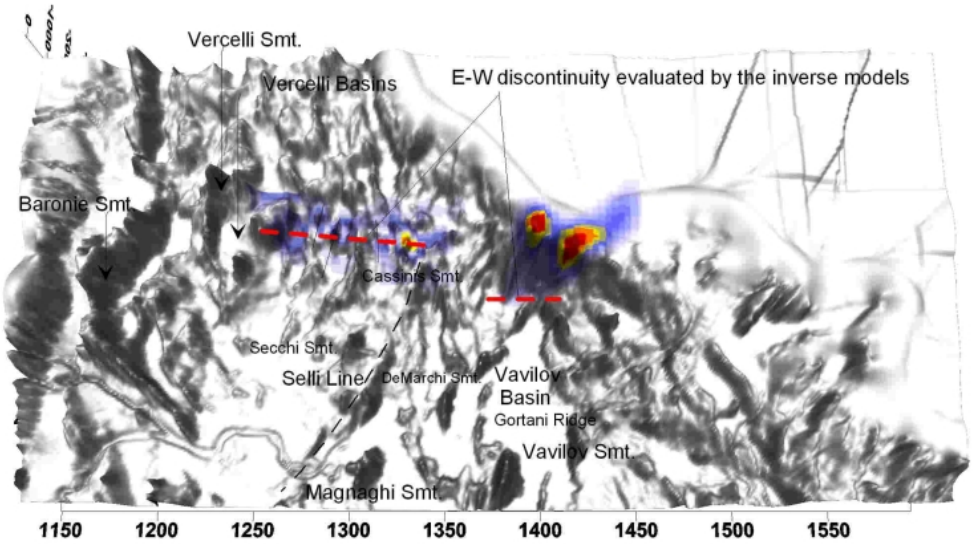

Figure 9.10: Recovered model of magnetic anomaly of the 41st parallel zone overlapped to 3D bathymetry; red tracks represent the traces of the 41st discontinuity derived from magnetic analysis.

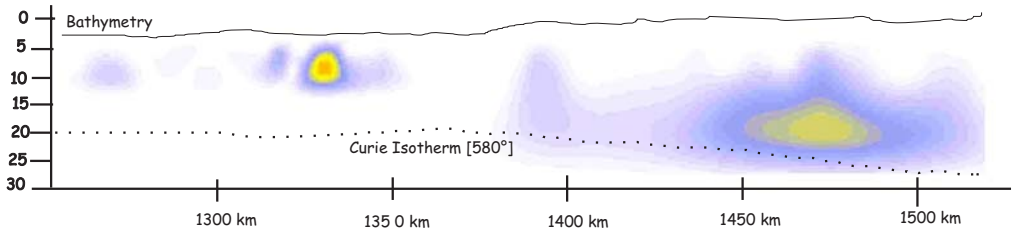

Figure 9.11: Inverse model of the global magnetic structure of 41st parallel zone with superimposed the Curie Isotherm

Selli and Magnaghi basin area (box C) and the northernmost portion of the Vavilov basin (box D) (Fig. 9.1). The magnetic pattern of the Selli line and Magnaghi basin sub-region was previously analysed through a 2D inverse algorithm which gave a magnetization distribution strongly dominated by the structural setting of the area. In particular the highly magnetized rocks are confined by the Selli line fault system and by a set of E-W normal vertical faults of undefined age. The 2D model also underlined a complex structure of the crust where the presumed oceanic crust domain is locally broken by tilted and rotated continental blocks. In the study area instead the deep crustal setting is less clearly defined: the crustal-mantle discontinuity rises from 25-30 km in the Sardinia region to 10 km around the Vavilov Smt while the exact Moho depth is unknown. The only estimate available is a Moho depth varying from 20 to 10 km as a result of the work of Sartori et al. (2004), who studied the crustal features along a E-W profile across the Selli line. The area was inverted with a 20x20x10 voxel mesh and 700 real data items, providing a closure of the source at a depth of 16 km, which in fact matches the Moho distribution. The model highlights the high magnetic component of the generating structures of the Magnaghi basin and its seamount (fig. 8.12). The first evidence of magnetization (lowest values) occurred at a depth of 4 km, while the horizontal cross-section of 11 km shows the maximum magnetization value. The recovered source shows a N-S elongated shape, and this geometry coincides with the bathymetric structure of the Magnaghi basin. The Tortonian-Messinian opening of the Southern Tyrrhenian occurred in an E-W direction thus generating N-S distensive structures. In the northwestern area, around the De Marchi Smt. is located a E-W trending magnetized structure, a feature which suggests a change in magnetic pattern between the basin and its bordering areas. I simulated a set of Y-Z cross-sections (fig. 9.13). In an E-W direction the source of the Magnaghi basin shows a particular geometry. Westward, the magnetization has an oblique trend with a vertical edge corresponding to the Selli Line while in the opposite direction the source has a regular shape. This behaviour confirms the active role of the Selli line in the opening of the Mag-

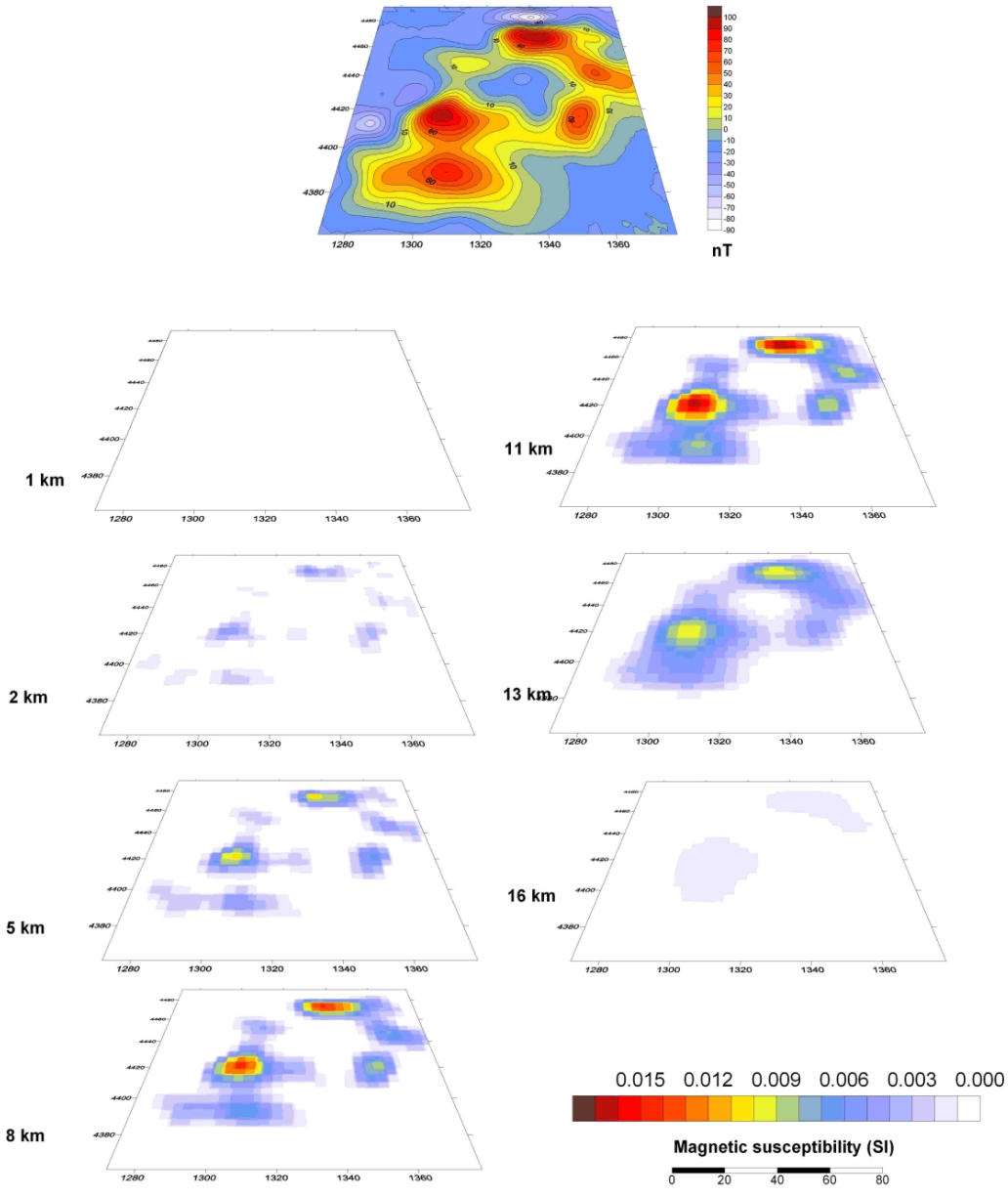

Figure 9.12: Horizontal cross-sections of the Selli Line region

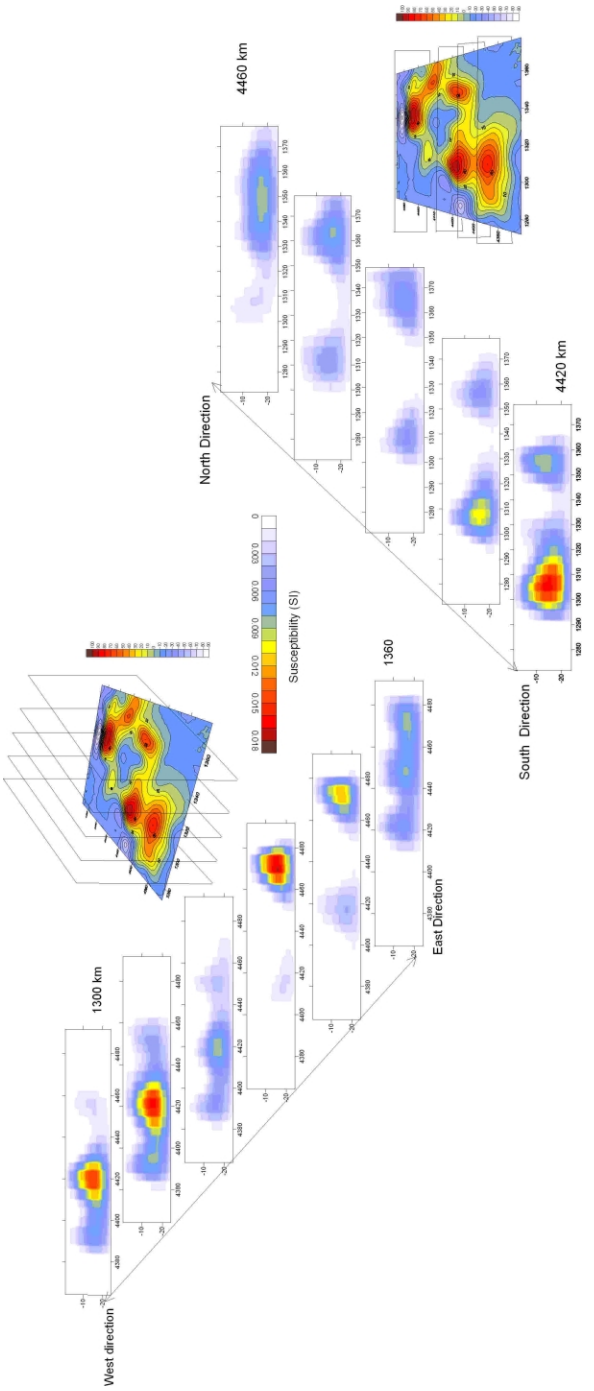

Figure 9.13: Global vision of the X-Z and Y-Z cross-sections of the Selli line region

naghi basin. It follows that the Selli Line may be also considered a deep crustal boundary whose morpho-bathymetric structure represents a shallow evidence of a deep structure involving the lower crust. Considering the Northern portion of the model, the Magnaghi basin source has an abrupt vertical closure where a large E-W source is displayed. This particular shape is visible in the X-Z cross-sections (figure 9.13). The Y-Z plane cutting the E-W source instead highlights a longitudinally developed source with a maximum depth of 13-15 km; this magnetic body is situated in the Magnaghi Basin and is bordered to the westward by the Selli line. Around the De Marchi region are imposed several normal-vertical faults as described in the Structural Map of Italy (Bigi et al., 1989,1990), in which these E-W faults are interpreted as small structures that deform only the Selli Line. Conversely, the models illustrated in figures 9.12-13 suggests an E-W trending deformation of the Selli line and of the Magnaghi-Demarchi region due to development of a transcurrent system. Additionally, the depth-distribution of the magnetic source highlights an activity on the part of this fault in the deep crustal portion of the Magnaghi basin. The result of the inversion gives a magnetic pattern of the Selli Line strongly dominated by the shallow structural features of the upper crust. From a magnetic point of view, this NE-SW fault system represents the real boundary between the Sardinia margin and the Magnaghi basin and is a discontinuity which also involves the deep portions of the crust, thus confirming an active role of the Selli line in the geodynamic process of the Southern Tyrrhenian Sea.

The Magnaghi basin shows a N-S magnetized pattern caused by E-W crustal stretching, although the magnetization is associated not only with the oceanic crust but also to a lesser extent with the submerged volcanic edifice. In the northern portion of the study area, the distribution of the sources changes its main direction from N-S to E-W, with the point of transition located around the De Marchi Smt, where a set of E-W vertical faults is displayed. The model created suggests a delimited crustal portion of the Magnaghi domain defined by two main vertical crustal boundaries with NE-SW and E-W directions. Finally, I shall examine the inverse

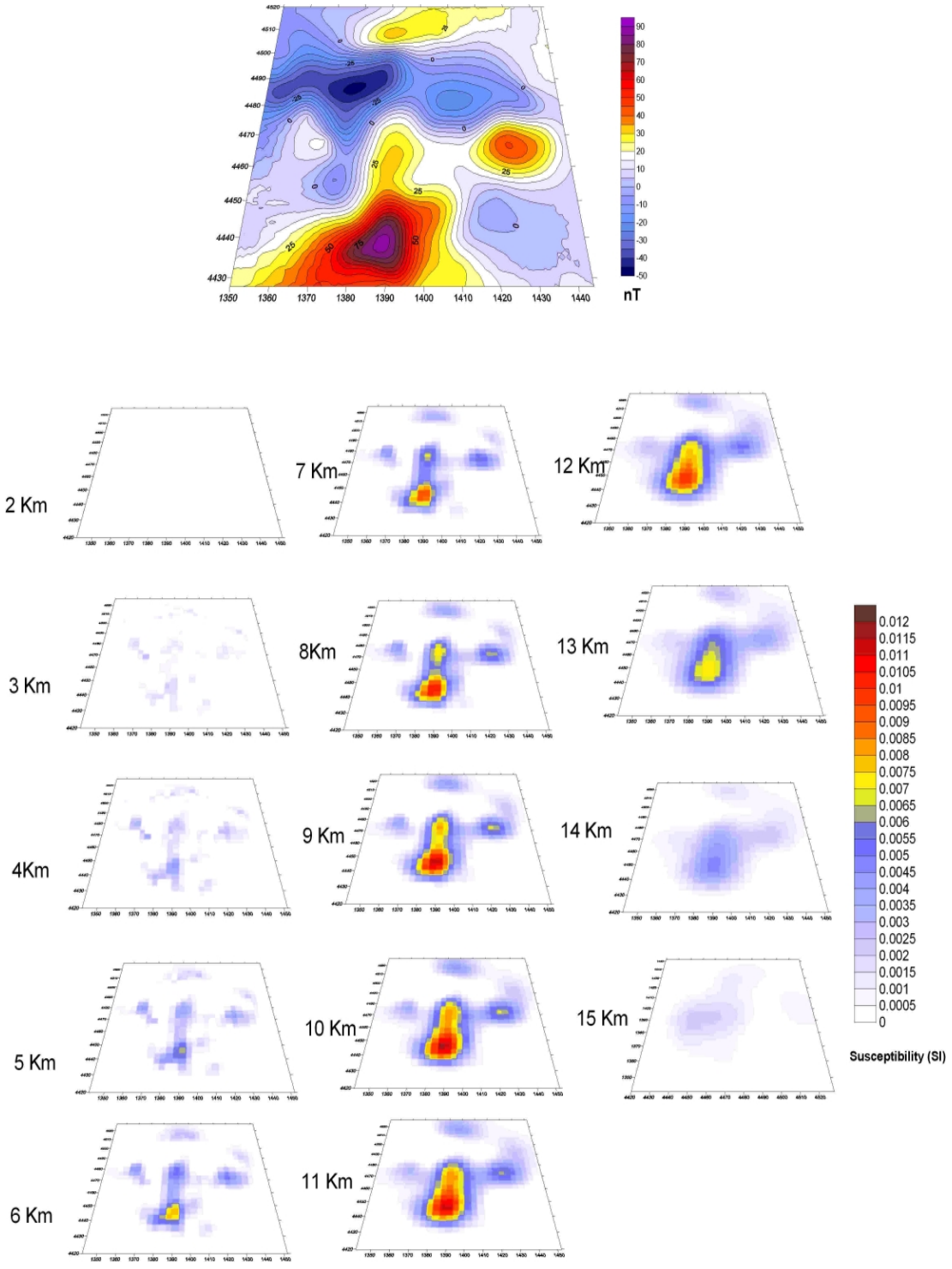

Figure 9.14: Recovered model of the northernmost portion of the Vavilov basin, horizontal cross-sections

model of the Vavilov basin area, which is enclosed in box D of figure 8.1 where the northern structures of this basin are located. The Vavilov basin is an abyssal area of triangular shape with a maximum depth of 2500 m, believed to have been formed as follows. The opening process of the Southern Tyrrhenian sea continued eastward after formation of the Magnaghi basin and during the Early Pliocene (4.6-2.3 My ago, Marani and Gamberi, 2004) crustal depletion occurred particularly in the eastern portions with an oceanic crustal development and the opening of a new basin. At the center of this area is located a volcanic edifice of Late Pliocenic age (3.0 My ago, Kastens et al., 1988) known as the Vavilov Seamount, whose magnetic pattern is dominated by high-value magnetic anomalies associated with the submerged volcanic evidences of the basin (oceanic crust with relics of continental crust blocks). The Vavilov edifice is well isolated from the nearby areas by its negative magnetized pattern, in that this structure shows an anomaly of -300/350 nT with a shape compatible with the topographic structure. The negative magnetization may be attributed to the age of its formation. The building of the seamount, in particular its northern portion, occurred during an inverse magnetic polarity chron C2A-Gauss epoch. The anomaly field of this basin shows a NNE-SSW development similar to the magnetic pattern of the Magnaghi basin. The Vavilov basin may be defined as a large structure with a N-S length of approx 2.5°, whose northernmost portion has a sharp shape confined at the lower edge by the 41^{st} parallel. Since the oceanic domain is not well defined in this portion, the inversion process was focused in this area. The magnetic anomaly field was inverted by using a prismatic mesh of 30x30x15 voxels and about 800 measured data items. The depth-to-the-bottom analysis has highlighted a closure of the deep source at a depth of 15 km, a value compatible with the depth of the Moho discontinuity values (from 10 to 15 km, Sartori et al., 2004). I applied the DTB value to constrain the inversion to this depth, thus obtaining the model shown in figure 9.14 (horizontal cross-sections).

The main magnetic source is represented by a N-S magnetized body with a length of 50 km. In the deep planes the N-S structure is interspersed with ENE-

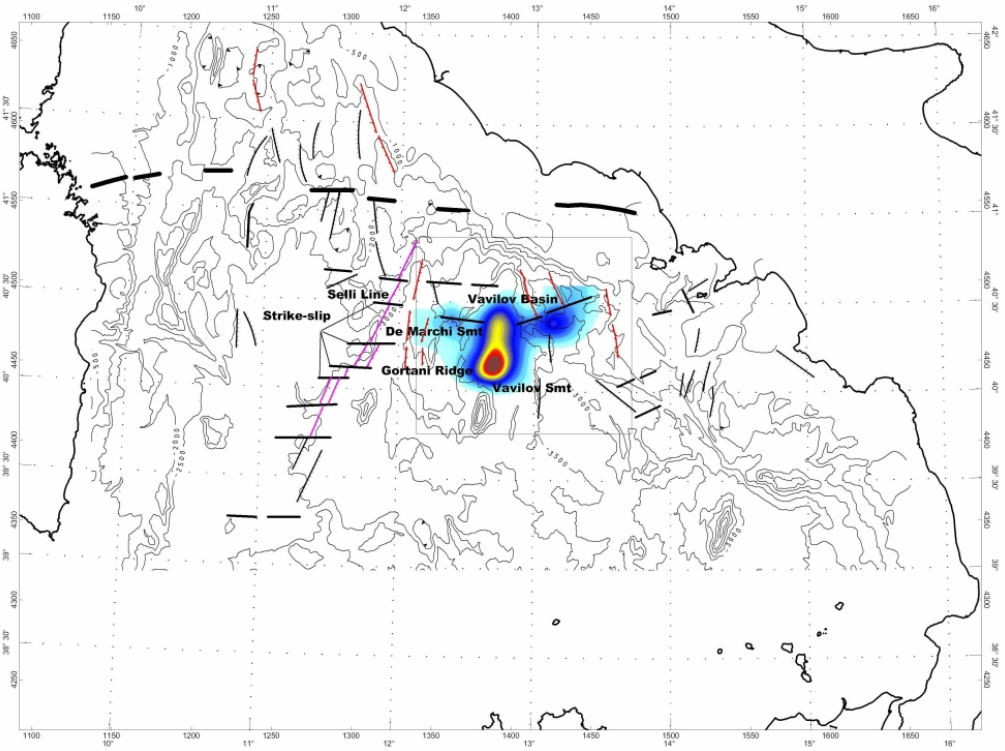

Figure 9.15: Horizontal cross section (plane at 10 km od depth) superimposed to the morpho-bathymetrical feature of the Southern Tyrrhenian Sea.

WSW trending magnetization. The main magnetic source is associated with smaller magnetized bodies located inside the abyssal basin, therefore the related magnetic pattern may be associated with an ambiguous relationship between the submerged structure and the oceanic crustal formation. Superimposing a plane of the model (cross-section of 10 km showing maximum value of magnetization) on the structural map of the Southern Tyrrhenian Sea, it is clearly visible that the magnetic source of the Vavilov basin is confined at the northernmost portion by an E-W vertical undefined fault (fig.8.15). This structural element is linked to the E-W fault system which breaks the Selli line and the Magnaghi basin, and the same E-W deformation also has a leading role in the distribution and shapes of the magnetic sources in the Vavilov basin, since the ENE-WSW magnetized pattern is well linked to a structural evidence represented by a NE-SW fault system. This fault is imposed on a calc-

alkaline volcanic structure linked to the subduction related volcanism which occurred during the Messinian-Pliocene (Bigi et al., 1990). Along the fault direction a small magnetized source developed with an oblique shape due to the displacement of the structural elements.

10 Interpretation of the results

This last chapter describes the interpretation of the results of the 3D inverse process through analysis of the inverse models of the two main areas, the 41^{st} parallel and the Selli Line region. I begin by describing the structural setting of the E-W magnetic lineament along latitude N41^{st} and highlighting its relationship with the Southern Tyrrhenian Sea. The second part addresses a chronological reconstruction of the Selli Line fault system, which enables to define the overall geodynamics of the Central Tyrrhenian area.

10.1 The structural setting of the 41^{st} parallel zone

The results given by the different quantitative analyses of the anomaly field of the Central Tyrrhenian make it possible to produce a structural/geologic reconstruction of the 41^{st} parallel zone, an area which has so far not been studied directly partly because it is little known and partly due to its inaccessibility. For these reasons magnetic prospection provides a useful tool to study its crustal setting.

The 41^{st} parallel zone contains several magnetic anomalies which form the well-known magnetic lineament. This feature however is only the first consideration regarding this area, in that all the geophysical and geological data on the Central Tyrrhenian Sea confirm the peculiar role of the 41^{st} parallel in the geodynamic evolution of the entire Tyrrhenian. As described in the first chapter of this thesis, the crustal and lithospheric setting of the Tyrrhenian is dominated by a clear division between the northern and southern portions, and a boundary between these two domains is represented by the 41^{st} parallel. The statistical analysis of the power spectrum and the wavelet analysis of the magnetic data have highlighted a clear geographic position of this boundary, which may also be associated with the gravimetric data. Study of the apparent magnetization maps has suggested a distribution of magnetic sources in a NE-SW direction which connect the easternmost portion of the 41^{st} parallel zone with the northernmost area of the Selli-Magnaghi region. The

3D inversion of the magnetic evidences of the E-W lineament has provided information on the 3D geometry of the buried sources, thus allowing a possible interpretation. More specifically, figure 10.1 shows the superimposition on the bathymetric surface of a common X-Y cross section (plane at 8 km of depth) related to different 3D models (see previous chapter). The 3D inversion of the magnetic anomalies

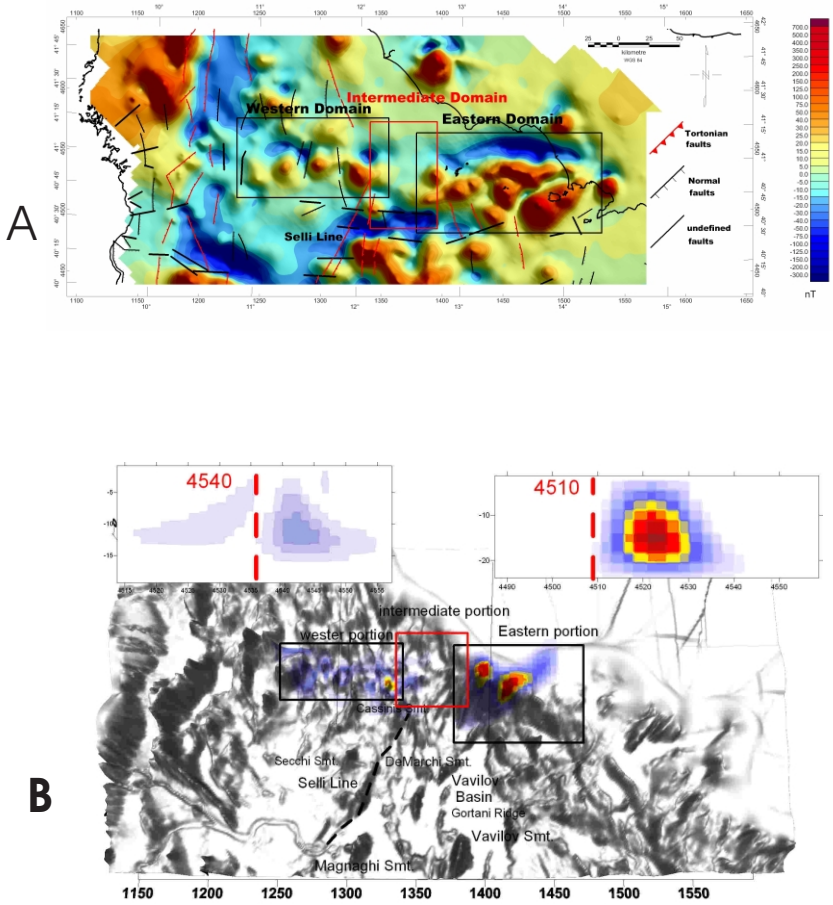

Figure 10.1: A) Magnetic anomaly field of the Central Tyrrhenian Sea; B) X-Y cross-section of the 41^{st} parallel overlapped on the bathymetric surface with two Y-Z cross-sections (extracted from fig. 9.4 and 9.9)

of the 41^{st} discontinuity highlights a key point: the magnetic characteristics along this alignment are non-homogeneous, thus demonstrating the existence of a clear distinction between the eastern and western portions. The western domain of the

41^{st} lineament is characterized by three distinct magnetic anomalies which are not apparently associated with a related morphologic structure such as submerged edifices. However this area also contains the submerged/intrusive Vercelli complex, which is believed to be a grano-dioritic intrusion developed during the Tortonian age (Barberi et al., 1978), therefore potentially connected to the Tortonian rifting process which occurred in the Northern Tyrrhenian Sea. Since the Vercelli structure's magnetic pattern is compatible with the three anomalies of the westernmost portion of the 41^{st} lineament, the buried sources generating the anomaly field may be considered of an intrusive nature like that of the Vercelli. It is therefore possible that this ensemble of sources is related to a common Tortonian geodynamic phase.

The sources associated with the three magnetic evidences show a bottom closure at a depth of 14 km, which is compatible with the basement depth obtained through thermal studies. The modeled sources have a distinctive shape dominated by an oblique growth trend, and along their longitudinal distribution show an abrupt decay around the coordinate of the 41^{st} parallel, which may be due to a structural boundary (fig. 10.1b). Looking instead at the easternmost portion of the E-W magnetic lineament, the distribution of the magnetic sources shows a different behaviour, in that maximum bottom depth at 19 km with an increase of the depth of the magnetic basement in contrast with the western domain. The model of the eastern portion also highlights the superimposition of two main magnetization trends, of which the first runs E-W and the second NE-SW, the latter thus being compatible with the magnetic behaviour of the Selli Line region. As a result it may be deduced that this common distribution of magnetization is due to a common deformative event, which strengthens the hypothesis that the NE-SW magnetic pattern is further evidence of a possible relationship between the 41^{st} and the Southern Tyrrhenian Sea. The inverse model of the magnetic anomalies of the eastern portion of the 41^{st} parallel zone has highlighted an abnormal distribution of magnetization similar to that of the sources of the western area. The vertical distribution of magnetization is dominated by an oblique trend, which suggests that the supposed crustal bound-

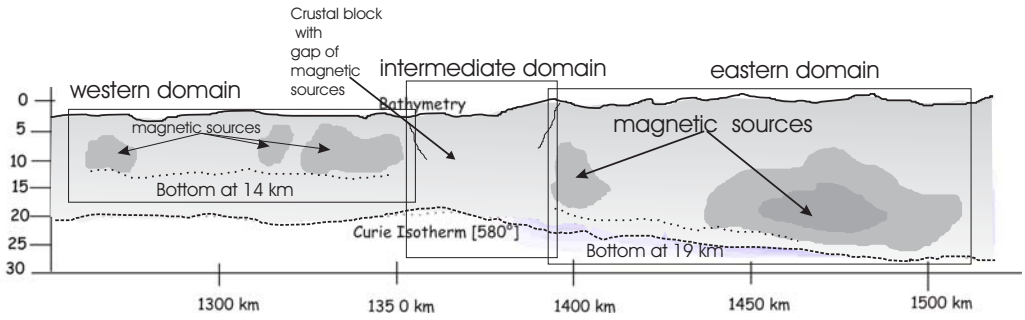

Figure 10.2: Structural sketch of the 41^{st} parallel.

ary is not located at the coordinate of the 41^{st} parallel but lies 20-30 km further south, this southward shift presumably being caused by a superimposition of two effects, namely (A) the E-W movement and (B) a NE-SW trending deformation due to the Southern Tyrrhenian opening. According to this hypothesis the Selli Line shows an active role in the geodynamic evolution of the Central Tyrrhenian Sea, and the NE-SW fault system may be the cause of the different displacement of the 41^{st} parallel. The E-W and NE-SW movements confirms that the 41^{st} parallel may be divided into two domains, with the eastern domain separated from the western by a particular crustal portion, here referred to as *intermediate zone*. Between the two domains lies a zone characterized by a gap in magnetic evidences, where the magnetic basement and Curie isotherm increase in depth and additionally which shows different crustal features in contrast with the general setting. Observing the geographical distribution of the structural elements of the Central Tyrrhenian Sea, the Selli Line is located below the intermediate area (fig.10.1a). The area between the two magnetic domains of the 41^{st} parallel may thus be interpreted as a crustal block which divides the E-W lineament, obstructing the northward development of the Selli Line (fig. 10.2).

The division of the 41^{st} lineament into two distinct domains is also supported by the stratigraphy data of the syn-rift sediments (Rosembaum and Lister, 2004). Syn-rift sedimentation in the Tyrrhenian area began in the Tortonian and the dis-

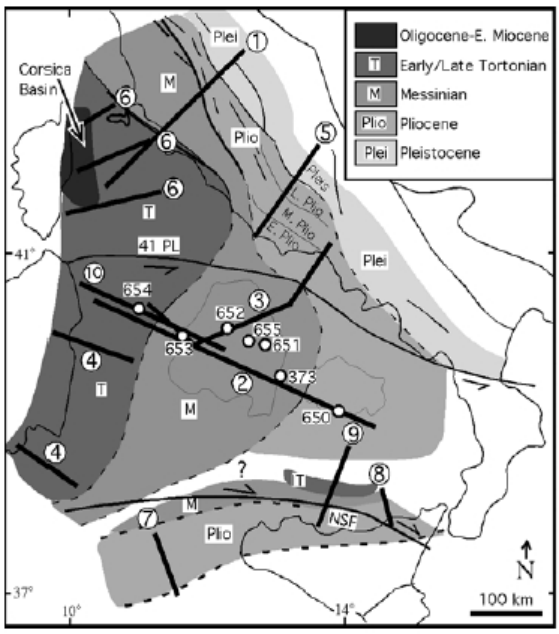

Figure 10.3: Distribution of the earliest syn-rift deposits of the Tyrrhenian Sea, from Rosembaum and Lister (2004)

tribution of these syn-rift deposits was strongly dominated by the direction of the extension. According to Rosembaum and Lister (2004) the Selli Line divides the Tyrrhenian Sea into two main domains, of which that located at the western end of the Selli is characterized by Tortonian syn-rift deposits while the second domain is located in the eastern portion where Messinian-Pliocene syn-rift sequences have been recovered. As clearly shown in figure 10.3 (after Rosembaum and Lister 2004), the limit between Tortonian and Messinian-Pliocenic syn-rift deposits crosses the 41^{st}. The distribution of the syn-rift deposits agrees with our reconstruction: the extensional movement changes direction and amplitude along the Selli Line, thus also involving the 41^{st} parallel zone. For a clear reconstruction of the geodynamics of the Central Tyrrhenian area I shall now define the chronological evolution of the Selli Line fault system.

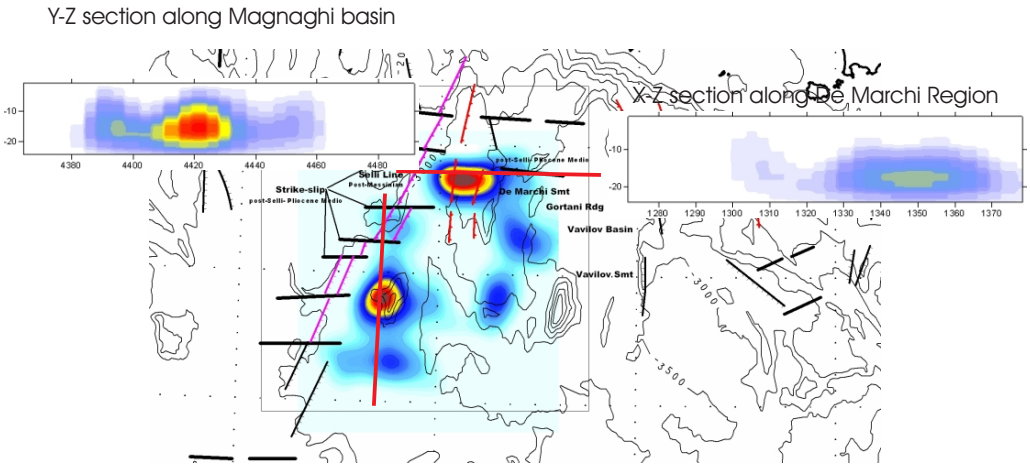

Figure 10.4: Inversion models of the Selli Line-Magnaghi region with Y-Z and X-Z cross-section obtained from model of figure 9.13

10.2 Chronological reconstruction of the Selli Line region

The tectonic evolution of the Southern Tyrrhenian Sea is dominated by an eastward roll-back movement of the Africa-Europa subduction system (Malinverno and Ryan, Patacca et a., 1990, Doglioni, 1991, 1994). As described above, the distribution of the syn-rift sediments is an important tool for analysis of the tectonic evolution. The time-sequence of the opening process of the Southern Tyrrhenian Sea is known but the moment in which its the extensive structures were formed has to date not been pinpointed. Several seismic profiles have been plotted crossing the Selli Line (Sartori et al., 2004), showing that the Selli displaces the Messinian sedimentary units without affecting the Tortonian sequences. This behaviour is also supported by analysis of the ODP-Leg 107 data (Kastens, 1988). On the basis of the reconstruction of Tortonian sediment distribution by Cipollari et al.(1999), the Selli Line may be dated as a Messinian structure. The inversion models of the Selli Line-Magnaghi region described in the previous chapter are illustrated in figure 10.4, which gives an overall vision of the models of this area. Examination of the overall picture leads to the following conclusions regarding the evolutive steps of the Selli-Line and Magnaghi region.

1. The fault system extends for 100-120 km NE-SW, dividing the Sardinian block (Cornaglia Terrance) from the Magnaghi abyssal basin;

2. The Selli Line is limited to the north and south by two distinct E-W discontinuities: the 41^{st} parallel zone and the North Sicily Fault (NSF, Rosembaum and Lister, 2004);

3. Analysis of the model of the Magnaghi basin shows that the magnetic source is delimited to the westward by a deep crustal boundary (maximum 10-12 km). If we accept that the Magnaghi basin was formed during the Messinian-Pliocene (Kastens, 1988; Serri et al., 2001), then chronologically the Selli Line belongs between two defined time sequences: the Tortonian syn-rifts are located in the western portion of the faults system whereas the magnetic source of the Magnaghi basin (Messinian-Pliocene) developed in the eastern portion. The Selli Line may therefore be interpreted as a Messinian-Pliocenic structure;

4. The distribution of the magnetic sources around the northernmost zone of the Selli line follows an E-W pattern, with an E-W elongated source located around the De Marchi region. This magnetic structure runs along an E-W vertical fault (strike slip) of unknown age(Bigi et al., 1990). The E-W elongated magnetic source is associated with the structure of the De Marchi basin (3.6-5 Ma, Sartori et al., 2004), suggesting a Pliocenic age of the E-W trending fault that borders this source;

5. The Selli Line is broken and deformed by a sequence of younger E-W strike-slips of Pliocenic age. Lastly, the Selli Line may be interpreted as the northwesternmost limit of the Southern Tyrrhenian basin of Messinian age.

The E-W strike-slip system which interrupts the Selli Line may be related to a Pliocenic re-activity of the E-W extensional movement along the 41^{st} parallel.

10.3 A geodynamic scenario

Interpretation of the magnetic inverse models suggests that the current crustal/geologic setting of the Central Tyrrhenian Area is strongly correlated with the development of two main structures, the 41^{st} parallel and the Selli Line. A chronological reconstruction of the NE-SW fault system and the crustal features of the 41^{st} parallel makes it possible to create a possible geodynamic scenario for the Central Tyrrhenian Sea, although it is clear that my reconstruction is only one evolutive scenario based on the model created by inverting the magnetic data. Figure 10.5 shows the various magmatic products and the distribution of the main structural elements.

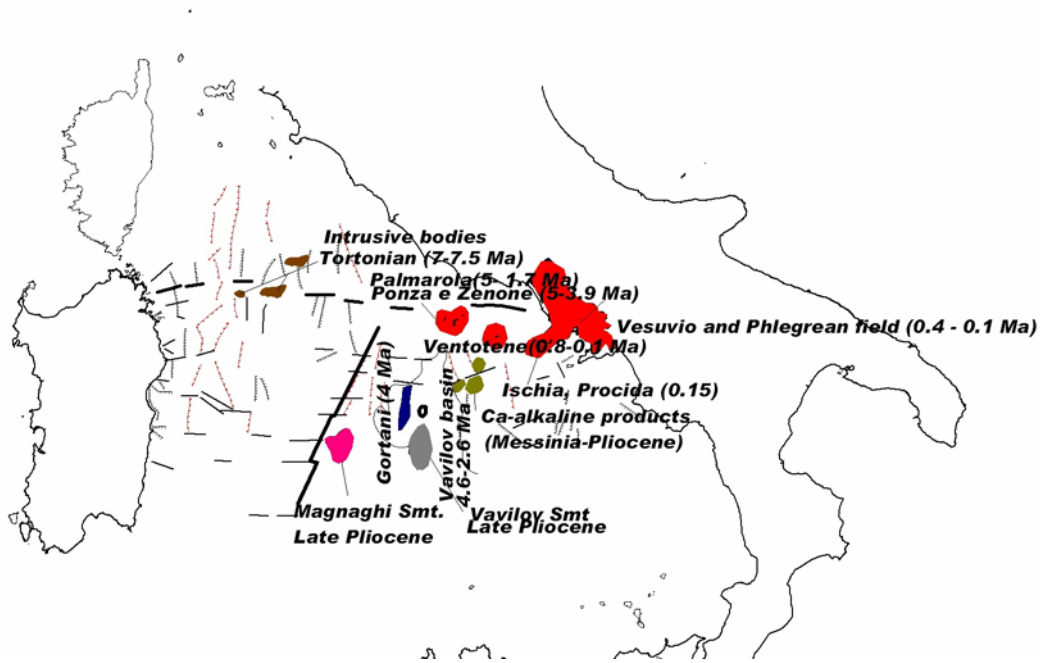

Figure 10.5: Map showing the distribution of the main magmatic events of the Central Tyrrhenian Sea (from Bigi et al., 1990 and Serri et al., 2001)

1. STAGE - In the Southern Tyrrhenian Sea an extensional tectonic connected to an eastward flexural movement of the subduction system commenced during the Tortonian. The Europa-Africa roll-back followed a preferential direction

due to two main discontinuities: the 41^{st} parallel and the North Sicily Fault. During the Tortonian phase the extensional movement occurred in the westernmost portion of Central Tyrrhenian Sea (fig. 10.6a), and the formation of the buried intrusive structures of the western portion of the 41^{st} lineament is correlated with this evolution stage. A continuous eastward movement of the extension may have generated the E-W elongated shape of the magnetic sources of this area and indeed the anticlockwise rotation of the source suggests a left movement along the 41^{st} discontinuity.

2. STAGE - The E-W extension along the 41^{st} parallel zone was still active during the Messinian. After emplacement of the intrusive bodies in the western portion of the 41^{st} parallel, the eastward movement drifted into the central portion of the lineament, an area in which there is a distinctive crustal block elongated for 40-50 km, characterized by a considerable thickness with a deep magnetic basement (figs. 10.1, 10.2). This block interrupts the E-W deformation and generates a gap of intrusive/effusive structures along the 41^{st} parallel zone (fig 10.6b). It was during this stage that the first evidences of the Selli Line NE-SW fault system were laid at the south of this crustal block, while the current position of this fault system may be due to the relationship between crustal setting of this middle portion of the 41^{st} parallel and the E-W extensional movement.

3. STAGE - The Selli Line is a large structure extending for one hundred kilometers and dividing two crustal blocks (Sardinia-Southern Tyrrhenian). Its formation may be the cause of the southward shift of the crustal boundary located on the easternmost portion of the 41^{st} parallel (fig. 10.6c) and in this context I can hypothesize that during the Late Messinian-Early Pliocene a NE-SW movement along the Selli Line generated a dislocation of the crustal blocks located in the eastern part of the Central Tyrrhenian. This deformation is highlighted by a NE-SW trending pattern of magnetization which connects

the Campanian margin and the northernmost portions of the Magnaghi and Vavilov basins.

4. STAGE - During the Pliocene the Central Tyrrhenian Sea was subjected to an E-W extension with a new E-W deformation involving the Selli Line region and with a number of E-W elongated strike-slips being displaced along the Selli Line itself. The inverse model provides the age of these faults, which are distributed along the Selli Line and around the westernmost portion of the Magnaghi-Vavilov basins (fig. 10.6d). Their displacement suggests a close relationship with an extensional movement localized at a nearby point such as the 41^{st} parallel and coincides with the fact that during the Pliocene the Central Tyrrhenian Sea was dominated by a re-activity of an E-W movement affecting the 41^{st} parallel.

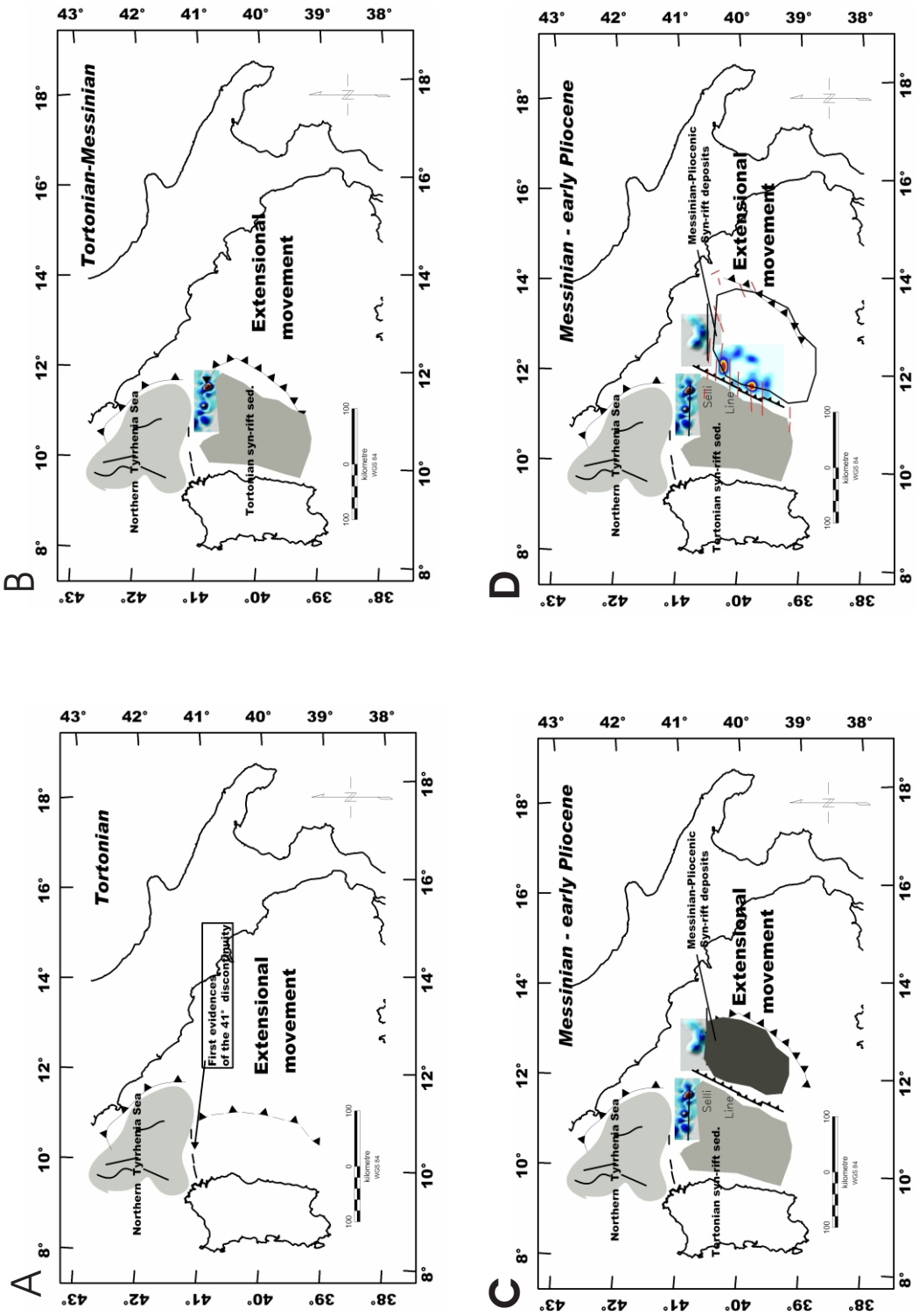

Figure 10.6: Map showing the evolution of the extensional movement in the Central-Southern Tyrrhenian Sea since the Middle Tortonian; A) Tortonian stage: the Northern Tyrrhenian basin is formed and the extensional movement is moved in the southern portion; B) Tortonian-Messinian Stage: The extension shows a E-W direction along the 41^{st} parallel, the Tortonian syn-rift deposits took place in the westernmost portion of the basin; C) Messinian-Pliocene stage: The roll-back movement shifts in a NW-SE position with the imposition of the first evidence of the Selli Line; the easternmost sources of the 41^{st} parallel zone are southward dislocated; D) Pliocenic stage: A E-W tectonic deforms the Selli Line and the structures of the Magnaghi Basin

The above points describe the four main stages in the evolution of 41^{st} discontinuity. There are several Pleistocenic-Quaternary products outcropping along this lineament (Bruno et al., 2002), but it would appear that these products were a passive result of the discontinuity since in terms of geodynamic evolution the activity of the 41^{st} discontinuity ended in the Pliocene age.

The evolution of the Central portion of the Tyrrhenian Sea is dominated by the existence of a discontinuity along a latitude of 41^{st}. The main effects of the extensional movement are concentrated in this area, where they form a lineament of emerged and submerged structures. A possible lithospheric nature of the 41^{st} discontinuity is suggested by the outcropping of OIB-type rocks on Palmarola (Pliocenic age, Cadoux et al., 2005). The Selli Line fault system may be interpreted as an effect of the extensive tectonic along the 41^{st} parallel since both the shape of the Selli Line and its geographical position are strongly correlated to the crustal features of the discontinuity of the 41^{st} parallel.

The bibliography

Andersen, F. H. and Pedersen, L.B. 1979. Some relations between potential fields and the strength and center of their sources, Geoph. Prosp., 27, 761-774.

Barbosa, V. C. F. and Silva J.B.C. 1994. Generalized compact gravity inversion, Geophysics, 59, 57-68.

Ballarin S. 1963. Il campo della gravita in Italia: carte delle anomalie topografiche- isostatiche. Commis. Geodet. It. Mem., 17.

Barberi, F., Bizouard, H., Capaldi, G.et al. 1978. Age and nature of basalts from the Tyrrhenian abyssal plain.In:Hsu,K.,Montadert,L.et al.(Eds.),Initial Reports of the DSDP, 42/I.US Government Printing ,Washington,DC,509-514.

Bartole, R. 1995. The north Tyrrhenian-Northern Apennines post-collisional system: constrain for geodynamic model, Terra Nova, 7-30

Beccaluva, L., Bonatti, E., Dupuy, C. et al. 1990. Geochemistry and mineralogy of volcanic rocks from ODP sites 650,651,655, and 654 in the Tyrrhenian Sea, Proceeding of the ODP, Scientific Results, 107, 49-74

Beccaluva, L., Di Girolamo, P., Serri G. 1991. Petrogenesis and tectonic setting of the Roman Volcanic Province, Lithos, 26, 191-221.

Bellani, S., Squarci, P., Taffi, L., Ceccarelli, A., Fiordelis, A. 1994. Sintesi dei dati di gradiente geotermico e di flusso di calore ottenuti da pozzi di profoditàmedio-piccola perforati nella Toscana centro-meridionale. Rapporto CNR-IIRG/ENEL-VDAG,14 pp

Bhattacharyya, B. K. 1964. Magnetic anomalies due to prism-shaped bodies with arbitrary polarization, Geophysics, 29, 517-531.

Bhattacharyya, B. K. and Leu, L.K. 1975. Analysis of magnetic anomalies over Yellowstone National Park: mapping Curie point isothermal surface for geothermal reconnaissance,J. Geophys. Res., 80, 4461-4465.

Bigi, G., Castellarin, A., Catalano, R. et al. 1989. Synthetic structural-kinematic map of Italy, scale 1:2000000, Progetto finalizzato Geodinamica, CNR, Roma

Bigi, G., Cosentino, D., Parotto, M. et al. 1990-1992. Structural Model of Italy and Gravimetry Map. Sheets 1-9,Progetto finalizzato Geodinamica, CNR, Roma

Blakely, R. J. 1988. Curie temperature isotherm analysis and tectonic implications of aeromagnetic data from Nevada, J. Geophys. Res., 93, 11817-11832.

Blakely, R. J. 1995. Potential Theory in Gravity and Magnetic Applications, Cambridge University Press, Cambridge, U. K.

Boccaletti, M., et al. 1990a, Migrating foredeep-thrust belt system in the northern Apennines and southern Alps, Palaeogeogr. Palaeoclimatol. Palaeoecol., 77, 3-14.

Boccaletti, M., Nicolich, R., Tortorici, L. 1990b. New data and hypothesis on the development of the Tyrrhenian Basin, Palaeogeogr. Palaeoclimatol. Palaeoecol., 77, 15- 40.

Bottinga,Y. and Steinmetz, L. 1979.A geophysical, geochemical, petrological model of the sub-marine lithosphere,Tectonophysics,55,311-347.

Boulanger, O. and Chouteau, M. 2001. Constraints in 3D gravity inversion, Geoph. Prosp., 49, 265-280.

Burrus, J.and Foucher, J.P. 1986. Contribution to the thermal regime of the

Provencal basin based on flumed heat flow surveys and previous investigation. In: The European Geotraverse PArt 2 (eds. Galson and St. Mueller), Tectonophysics, 128, 303-334

Cadoux, A., Pinti, D.L., Aznar, C., Chiesa, S., Gillot, P. 2005. New chronological and geochemical constraints on the genesis and geological evolution of Ponza and Palmarola Volcanic Islands (Tyrrhenian Sea, Italy), Lithos, 81, 121-151

Cain, J.C., Hendricks, S., Daniels, W.E., Jensen, J.C. 1968. Computation of the main geomagnetic field from spherical harmonic expansion. Date User's Note NSSDC, 68-11, Greenbelt, Maryland.

Calcagnile, G. and Panza, G.F. 1980. The main characteristics of the lithosphere
-asthenosphere system in Italy and surrounding regions. Pure Appl. Geophys., 119, 865-879.

Caratori Tontini, F., Faggioni, O., Beverini, N., Carmisciano, C. 2003. Gaussian envelope for 3D geomagnetic data inversion, Geophysics, 68, 996-1007.

Caratori Tontini, F., Stefanelli, P., Giori, I., Faggioni, O., Carmisciano, C. 2004.The revised aeromagnetic anomaly map of Italy, Ann. Geoph., 47, 1547-1555.

Catalano R., Doglioni C., Merlini S. 2001. On the Mesozoic Ionian basin. Geophys. J. Int., 144, 49-64.

Cataldi, R., Mongelli, F., Squarci, P., Taffi, L., Zito, G., Calore, C. Geothermal ranking of Italian Territory, Geothermics, 24, 115-129

Chapin, D.A. 1996. A deterministic approach toward isostatic gravity residuals A case study from South America, Geophysics, 4, 10221033.

Chiappini, M., Meloni, A., Boschi, E., Faggioni, O., Beverini, N., Carmisciano, C., Marson, I. 2000. Shaded relief magnetic anomaly map of Italy and surrounding marine seas. Ann. Geoph., 43, 983-989.

Claerbout, J. F. 1976. Fundamentals of Geophysical Data Processing with Applications to Petroleum Prospecting, McGraw-Hill, New York.

Connard, G., Couch, R., Gemperle, M. 1983. Analysis of aeromagnetic measurements form the Cascade Range in central Oregon, Geophysics, 48, 376-390.

Consiglio Nazionale delle Ricerche. 1992. Structural Model of Italy and Gravity Map. Progetto Finalizzato Geodinamica. Quaderni de La Ricerca Scientifica, 114 (3) (9 sheets)CNR.

Cooley, J.W and Turkey, J.W. 1965. An algorithm for the machine calculation of complex Fourier series. Mathem. Comput., 19, 297-301

Daubechies, I. 1990: The wavelet transform time-frequency localization and signal analysis. IEEE Trans. Inform. Theory, 36, 961-1004.

Della Vedova, B., Bellani, S., Pellis, G., Squarci, P. 2001. Deep temperatures and surface heat flow distribution. In: Vai, G.B., Martini, I.P. (Eds.), Anatomy of an Orogen: The Apennines and Adjacent Mediterranean Basins. Kluver Academic Publishing, Great Britain, pp. 65-76.

Della Vedova, B. and Pellis, G. 1980. Deep thermal trend for the Po valley from Agio temperature measurements in gas and oil wells. Boll. Geof. Teor. App. 23, 129-138

Della Vedova, B., Pellis, G., Foucher, J.P., Rheault, J.P. 1984. Geothermal structure of the Tyrrhenian Sea. Marine Geology, 55, 271-289

Della Vedova, B. and Pellis, G. 1986. Realizzazione della mappa di flusso di calore per i mari italiani. In: Rapporto finale del P.F. Oceanografia e Fondi Marini-S.P Risorse Minerarie, CNR, ROma, 295-340

Della Vedova, B. and Pellis, G. 1988. Thermal regime of the South Adriatic Basin. Preliminary results. Atti 7°Convegno GNGTS, 1403-1408

Della Vedova, B., Marson, I., Panza, G.F., Suhadolc, P. 1991. Upper mantle of the Tuscany area: A framework for its recent tectonic evolution, Tectonophysics, 195, 311-318

Della Vedova, B., Pellis, G., Crisci, G., Barca, D. 1993. Regime termico e processi magmatici nel Tirreno Meridionale. Atti 11°Convegno GNGTS, 601-612

Della Vedova, B., Lucazeau, F., Pasquale, V., Pellis, G., Verdoya, M. 1995. Heat flow in the tectonic provinces crossed by the Southern segment of the European geotraverse, Tectonophysics, 244, 57-74

Doglioni, C. 1991. A proposal of kinematic modeling for W-dipping subduction - Possible application to the Tyrrhenian-Apennine system, Terra Nova, 3, 423-434

Doglioni, C., Harabaglia, P., Merlini, S., Mongelli, F., Peccerillo, C., Piromallo, C. 1999. Orogens and slab vs. their direction of subduction, Earth Science rev. 45, 167-208

Doglioni, C., Innocenti, F., Morellato, C., Procaccianti, D., Scrocca, D. 2004. On the Tyrrhenian Sea opening, Mem. Descr. Carta.Geol.It, 64, 147164.

Ellam, R.M., Hawkesworth, C.J., Menzies, M.A., Rogers, N.W. 1989.The volcanism of southern Italy: role of subduction and the relationship between potassic and sodic alkaline magmatism, Journal of Geophysical Research, 94, 4589-4601.

Faccenna, C., Mattei, M., Funiciello, R., Jolivet, L. 1997. Styles of back-arc extension in the Central Mediterranean. Terra Nova, 9: 126-130.

Faggioni, O., Beverini, N., Carmisciano, C., Giori, I. 2001. A metrologic method of anomaly field amplitude bottom reduction in undersampled Geomagnetic Marine Surveys. Mar. Geoph. Res., 22, 63-79.

Faggioni, O. and Caratori Tontini, F. 2003. Quantitative evaluation of the time-line reduction performance in high definition marine magnetic surveys, Mar. Geophy. Res., 23, 353-365

Fairhead, J.D. and Odegard, M.E. 2002. Advances in gravity survey resolution, The Leading Edge.

Farge, M. 1992. Wavelet transforms and their applications to turbulence. Annu. Rev. Fluid Mech., 24, 395-457.

Favali, P., Funicello, R., Salvini, F. 1993. Geological and seismological evidence of strike-slip displacement along the E-W adriatic-central Apennine belt, In: Recent Evolution and Seismicity of the Mediterranean Region (Boschi et al. eds), 333-346.

Favali, P., Funicello, R., Mattietti, G., Mele, G., Salvini, F. 1993. An active margin across the Adriatic Sea (central Mediterranean Sea), Tectonophysics, 219, 109-117

Fedi, M., Florio, G., Rapolla, A. 1990. The role of remanent magnetization in the Southern Italian crust from aeromagnetic anomalies, Terra Nova, 2, 629-637

Fedi, M., Quarta, T., De Santis, A. 1997. Inherent power-law behavior of magnetic field power spectra from a Spector and Grant ensemble. Geophysics, 62, 4, 1143-1150.

Fedi, M., and Quarta, T. 1998. Wavelet analysis for the regional-residual and local separation of potential field anomalies, Geophys. Prospect., 46, 507-525.

Fedi, M. and Rapolla, A. 1999. 3-D inversion of gravity and magnetic data with depth resolution, Geophysics, 64, 452-460.

Finetti, R. 2003. The CROP profiles across the Mediterranean Sea (CROP Mare I and II), Mem. Desc. Cart. Geol. It, 62, 171-184

Foufoula-Georgiou, E. and Kumar, P. Eds. 1995. Wavelets in Geophysics. Academic Press, 373 pp.

Francalanci L., Taylor, S.R., Mc Culloch M.T., Woodhead J. 1993. Petrological and geochemical variations in the calc-alkaline rocks of Aeolian arc (Southern Tyrrhenian Sea, Italy). Con- trib. Mineral. Petrol., 113, 300-313.

Francalanci, L. and Manetti, P. 1994.Geodynamic models of the southern Tyrrhenian region: constraints from petrology and geochemistry of the Aeolian volcanic rocks. Bol. Geof. Teo. App., 36,283-292.

Gregotski, M.E., Jensen, O., ArkaniHamed, J. 1991. Fractal stochastic modeling of aeromagnetic data, Geophysics, 56, 17061715.

Gueguen, F., Doglioni, C., Fernandez, M. 1998. On the post-25 Ma geodynamic evolution of the western Mediterranean. Tectonophysics, 298 259-269.

Good, I.J. 1958. An interaction algorithm and practical Fourier Analysis. J. Roy. Stat. Soc., 20, 361-372.

Guillen, A. and Menichetti, V. 1984. Gravity and magnetic inversion with minimization of a specific functional, Geophysics, 49, 1354-1360.

Gunn, P.J. 1975. Linear transformations of gravity and magnetic fields, Geophysical Prospecting, 23, 300-312.

Hansen, P. C. 1994. Regularization tools: A Matlab package for analysis and solution of discrete ill-posed problems, Num. Alg., 6, 1-35.

Hansen, P. C. and O'Leary, D. P. 1993. The use of L-curve in the regularization of discrete ill-posed problems, SIAM J. Sci. Comput., 14, 1487-1503.

Hoernle, K., Zhang, Y., Grabham, D. 1995. Seismic and geochemical evidence for largescale mantle upwelling beneath the eastern Atlantic and Western Europe, Nature, 374, 3438.

Hutchison, I. 1986. Numerical modeling of the oceanic heat flow. A western Mediterranean case study. In: Thermal model in sedimentary basins (ed J. Burrus). Editions Technip Paris, 359-373

Helbig, K. 1963. Some integrals of magnetic anomalies and their relation to the parameters of the disturbing body, Zeitschrift f. Geophysik, 29, 81-96.

Ho-Liu, P, Montagner, J.P., Kanamori, H. 1989. Comparison of iterative back-projection inversion and generalized inversion without blocks: Case studies in attenuation tomography, Geophys. J. Int., 97, 19-29.

Jones, E. J. W. 1999. Marine Geophysics, Jones Wiley & Sons, Chirchester, 173-174

Kanasewich, E.R. 1977. Time sequence Analysis in Geophysics, The University of Alberta press, 1-364.

Kastens, K.A., Mascle, J., Aroux, C., et al. 1987. Proceedings of the Ocean Drilling Program (Part A). Initial Reports, (Sites 650-656) ODP, 107, 1013 pp.

Karner, G.D. and Watts, A.B. 1983. Gravity anomalies and flexure of the lithosphere at mountain ranges, J. geophys. Res., 88, 1044910477.

Kastens, K.A. et al. 1988. ODP Leg 107 in the Tyrrhenian Sea: Insights into passive margin and back-arc basin evolution. Geol. Soc. Am. Bull., 100, 1140-1156.

Landau, L. D. and Lif¡sits E.M. 1977. Statistical Physics, MIR, Moscow.

Langel, R.A., International Geomagnetic Reference Field, 1991 revision - International Association of Geomagnetism and Aeronomy (IAGA), Division V, Working Group 8: the main field and secular variation. Physics of the Earth and Planetary Interiors, 70, 1-6.

Last, B. J. and Kubik, K. 1983. Compact gravity inversion, Geophysics, 48, 713-721.

Lavecchia, G. 1988. The Tyrrhenian-Apennines system: Structural setting and seismotectogenesis, Tectonophysics, 147, 263- 296.

Li, Y. and Oldenburg, D. W. 1996. 3-D inversion of magnetic data, Geophysics, 61, 394–408.

Locardi, E. and Nicolich, R. 1988. Geodinamica del tirreno e dell'Appennino Centro-Meridionale:la nuova carta della Moho. Mem.Soc.Geol.It.,41 , 121-140.

Loddo, M., Mongelli, F., Pecorini, G., Tramacere, A. 1982. Prime misure di flusso di calore in Sardegna, CNR, RFE-RP,10, 181-210

Makris, J., Morelli, C., Zanolla, C. 1998. The Bouguer gravity map of the Mediterranean Sea (IBCMG), Boll. Geof. Teo. Appl. , 39, 7998.

Malinverno, A. and Ryan, W.B.F. 1986. Extension in the Tyrrhenian Sea

and shortening in the Apennines as a result of arc migration driven by sinking of lithosphere,Tectonics, 5, 227245.

Mandelbrot, B.B. 1967. How long is the coast of Britain? Statistical self-similarity and fractional dimensions, Science, 156 636638.

Marani, M.P. and Gamberi, F. 2004. Structural framework of the Tyrrhenian Sea unveiled by seafloor morphology,Mem. Descr. Carta.Geol.It, 64, 97108

Marani, M.P. 2004. Super-Inflation of a spreading ridge through vertical accretion, Mem. Descr. Carta.Geol.It, 64, 185-194

Marcotte. D.L., Hardwick, C.D., Nelson, J.B. 1992. Automated interpretation of horizontal magnetic gradient profile data, Geophysics, 57, 288-295

Maus, S. and Dimri, V.P. 1994. Scaling properties of potential fields due to scaling sources, Geophys. Res. Lett., 21, 891894.

Maus, S., Gordon, D., Fairhead,D. 1997. Curie-temperature depth estimation using a self-similar magnetization model, Geophys. J. Int., 129, 163-168.

Menke, W. 1989. Geophysical Data Analysis: Discrete Inverse Theory, Academic Press, San Diego.

Mongelli, F., Loddo M., Calcagnile, G. 1975. Some observations on the Apennines gravity field. Earth Planet. Sci. Letters, 24, 385-393.

Mongelli, F., Zito, G., Cataldi, R., Celati, R., Della Vedova et al. 1991. Geothermal regime of Italy and Surrounding seas. In: Terrestrial heat flow and the lithosphere structure (eds V.Chermak and L. Rybach), Springer-Verlag, Berlin, 381-394

Musacchio, M., Carrara, G., Gamberi, F., Marani, M.P. 1999. Tectonic setting of the eastern Tyrrhenian margin, Geoitalia-Fist, 184-185

Nettleton, L.L. 1939. Determination of density for reduction of gravimeter observations, Geophysics, 4, 176 183.

Nicolich, R. 1989. Crustal structure from seismic studies in the frame of the European Geotraverse (southern segment) and CROP Projects. In: Boriani A., Bonafed M., Piccardo G. B., Vai G. B. (Eds.): The lithosphere in Italy. Advances in Earth Science Research.le. Atti Convegni Lincei, 80, 41-61.

Nicolich, R. and Dal Piaz, G.V. 1992. - Moho isobaths. Structural Model of Italy. Scale 1:500,000. Quaderni della Ricerca Scientifica, 114 (3), CNR.

Nicolich, R. 2001. Deep Seismic transect, in Anatomy In: Vai, G.B., Martini, I.P. (Eds.),Anatomy of an Orogen: The Apennines and Adjacent Mediterranean Basins. Kluver Academic Publishing, Great Britain, pp. 47-52.

Nicolosi, I., Speranza, F., Chiappini, M. 2006. Ultrafast oceanic spreading of the Marsili Basin, southern Tyrrhenian Sea: evidence from magnetic anomaly analysis, Geology, 34,717-720.

Oldenburg, D.W. and Li, Y. 2003. Discussion on '3-D inversion of gravity and magnetic data with depth resolution', Geophysics, 68, 400-403.

Parker, R.L. 1972. The rapid calculation of potential Anomalies, Geophys. J. R. astr. Soc., 31, 447455.

Parker, R.L. 1977. Understanding inverse theory, Ann. Rev. Earth planet Sci., 5, 3564.

Pasquale, V. 1985. A review of the heat flow density values in Northern Italy.

Collana Studi e Ricerche, Accademia ligure delle Scienze, VI, 6, 77-90

Panza, G.F. 1984. Structure of the lithosphere-asthenosphere system in the Mediterranean region. In: Kahle H.G., Mueller S., Wilson P. (Eds.): Crustal dynamics in the Alpine-Mediterranean region. ù Ann. Geophys., 2, 137-138.

Panza, G.F. and Suhadolc, P. 1990. Properties of the lithosphere in collisional belts in the Mediterranean-A review, Tectonophysics, 182, 39-46

Panza G.F., Scandone P., Calcagnile G., Mueller S., Suhadolc P. 1992. The lithosphere-asthenosphere system in Italy and surrounding regions. Quaderni de La Ricerca Scientifica., 114, CNR.

Panza, G.F., Pontevivo, A., Chimera, G., Raykova, R., Aoudia, A. 2003. Lithosphere-asthenosphere: Italy and surroundings sea, Mem.Descr. Cart. Geolg. It.

Patacca, E., Sartori, R., Scandone, P. 1990. Tyrrhenian Basin and Apenninic arcs: kinematic relations since late Tortonian times. Mem. Soc. Geol. It, 45, 425-451.

Pedersen, L. B. 1991. Relations between potential fields and some equivalent sources, Geophysics, 56, 961-971.

Pignatelli, A., I. Nicolosi, M. Chiappini. 2006, An alternative 3D source inversion method for magnetic anomalies with depth resolution, Ann. Geophys., in press.

Pilkington, M. and Todoeschuck, J.P. 1993. Fractal magnetization of continental crust, Geophys. Res. Lett., 20, 627630.

Pilkington, M. 1997. 3-D magnetic imaging using conjugate gradients, Geo-

physics, 62, 1132-1142.

Portniaguine, O. and Zhdanov, Z. 2002. 3-D magnetic inversion with data compression and image focusing, Geophysics, 67, 15321541.

Rybach, L. and Jaffe, F.C. 1976. Geothermal potential in Switzerland. Proceedings of the Second Symposium on the development and use of the Geothermal resources, San Francisco, 241-244

Rybach, L., Werner, D., Muller, St. 1977. Heat flow, heat production and crustal dynamics in the Central Alps, Switzerland. Tectonophysics, 41, 113-126

Robin, C., Colantoni, P., Gennesseaux, M., Rehault, J. P. 1987. Vavilov seamount: a mid alkaline Quaternary volcano in the Tyrrhenian basin, Mar. Geol., 78, 125136.

Royden, L. 1988. Flexural Behaviour of the Continental Lithosphere in Italy Constraints imposed by gravity and deflection data, J. Geoph. Res., 93, 77477766.

Rosenbaum, G. and Lister, G. 2004. Neogene and Quaternary rollback evolution of the Tyrrhenian Sea,the Apennines, and the Sicilian Maghrebides, Tectonics, 23, TC1013, doi:10.1029/2003TC001518, 2004

Sandwell, D.T. and Smith, W.H.F. 1997. Marine Gravity anomaly from GEOSAT and ERS1 satellite altimetry, J. geophys. Res., 102, 1003910054.

Sartori, R. 1990. The main results of ODP leg 107 in the frame of Neogene to Recent geology of peri-Tyrrhenian areas. In: Kastens and Muscle et al. (eds): Proceedings of the ODP. Scentific Results, 107, 715-730

Sartori, R., Carrara, G., Torelli, L., Zitellini, N. 2001. Neogene evolution of the southwestern Tyrrhenian Sea (Sardinia Basin and western bathyal plane), Mar.

Geol.,175 ,47-66

Savelli, C. 1988. Late Oligocene to Recent episodes of magmatism in and around the Tyrrhenian Sea:Implications for the processes of opening in a young inter-arc basin of intra-orogenic (Mediterranean) type, Tectonophysics, 146, 163-181.

Savelli, C. and Schreider, A. A. 1991.The opening processes in the deep Tyrrhenian basin of the Marsili and Vavilov, as deduced from magnetic and chronological evidence of their igneous crust, Tectonophysics, 190, 119131.

Savelli, C. 2002. Time-space distribution of magmatic activity in the western Mediterranean and peripheral orogens during the past 30 Ma (a stimulus to geodynamic considerations) J. Geodynamics,34, 99-126.

Scarascia, S., Lozej A., Cassinis, R. 1994. Crustal structures of the Ligurian, Tyrrhenian and Ionian seas and adjacent onshore areas interpreted from wide-angle seismic profiles. Boll. Geofis. Teor. Appl., 36, 5-19.

Schreider, A.A. 1993.Chronology of the oceanic linear magnetic anoma lies, Phys. Earth, 4, 319.

Seber, D., Sandvol, E., Sandvol, C., Brindisi, C., Barazangi, M. 2001. Crustal model for the Middle East and North Africa region: implications for the isostatic compensation mechanism, Geophys. J. Int., 147, 630638.

Selli, R., Lucchini, F., Rossi, P.L., Savelli, C., Del Monte, M. 1977. Dati geologici, petrochimici, radiometrici sui vulcani centro-tirrenici, Giornale di Geologia,42, 221-246

Serri, G. 1990. Neogene-Quaternary magmatism of the Tyrrhenian region:

characterization of the magma sources and geodynamic implications, Mem. Soc. Geol. It., 41,219-242.

Serri G., Innocenti F., Manetti P. 1993. Geochemical and petrological evidence of the subduction of delaminated Adriatic continental lithosphere in the genesis of the Neogene-Quaternary magmatism of central Italy. Tectonophysics, 223, 117-147.

Serri, G., Innocenti, F., Manetti, P. 2001. Magmatism from Mesozoic to Present: petrogenesis, time-space distribution and geodynamic implications, in Anatomy of an orogen: the Apennines and adjacent Mediterranean Basins, edited by G. B. Vai and I. P. Martini, Kluwer Academic, London UK.

Servizio geologico nazionale. 1989.Gravimetric Map of Italy, scale 1:1.000.000. 2 sheets. Servizio Geologico Italia, Istituto Poligrafico e Zecca dello Stato, Roma.

Simpson, R.W., Jachens, R.C., Blakely, R.J., Saltus, R.W. 1986. A new isostatic residual gravity map of the conterminous United States with a discussion on the significance of isostatic residual anomalies, J. geophys. Res., 91, 83488372.

Silva, J. B. C., Medeiros, W. E., Barbosa, V. C. F. 2001. Potential-field inversion: Choosing the appropriate technique to solve a geological problem, Geophysics, 66, 511-520.

Simons, F. J., Van der Hilst, R. D. J., Montagner, P., Zielhuis, A. 2002. Multimode Rayleigh wave inversion for heterogeneity and azimuthal anisotropy of the Australian upper mantle, Geophys. J. Int., 151, 738-754.

Spadini, G. and Wezel, F.C. 1994. Structural evolution of the 41^{st} parallel zone: Tyrrhenian sea. Terra Nova 6, 552-562.

Spector, A. and Grant, F. S. 1970. Statistical models for interpreting aero-

magnetic data, Geophysics, 35, 293-302.

Tarantola, A. and Valette, B. 1982. Generalized nonlinear inverse problems solved using the least squares criterion, Rev. Geophys., 20, 219-232.

Tarantola, A. 1987, Inverse Problem Theory, Elsevier, Amsterdam.

Tikhonov, A. N. and Arsenin, V. Y. 1977. Solutions of Ill-Posed problems, Winston & Sons, Washington D. C.

Telford, W.M., Geldart, L.P., Sheriff, R.E. 1990. Applied Geophysics (2^{nd} edition), Cambridge University Press, Cambridge

Thorarinsson, F. and Magnusson, S.G. 1990. Bouguer density determination by fractal analysis, Geophysics, 7, 932935.

Torrence, C. and Compo,P.G., 1998. A Practical guide to Wavelet analysis, Bull. Americ. Met. Soc., 79, 1, 61-78

Van Dijk, J. P. and Scheepers, P.J.J. 1995. Neotectonic rotation in the Calabrian Arc; implications for a PlioceneRecent geodynamic scenario for the Central Mediterranean, Earth Sci. Rev., 39, 207246.

Vannucci, G., Pondrelli, S., Argnani, A., Morelli, A., Gasperini, P., Boschi, E. 2004. An atlas of Mediterranean seismicity, Ann. Geoph., 47.

Zito, G., Mongelli, F., De Lorenzo, S., Doglioni, C. 2003. Heat Flow and Geodynamics in the Tyrrhenian Sea, Terra Nova, 15, 425-432.

Zhdanov, M. S. 2002. Geophysical inverse theory and regularization problems, Elsevier Science Publishing, London.

Acknowledgements

I thank the two supervisors Fabio Caratori Tontini and Osvaldo Faggioni for their helpfulness during the thesis development. I am grateful to Michael Marani of Ismar Bologna for his competent support during the geologic interpretative phase of the thesis. I am indebted to the INGV staff of Fezzano for the technical and logistic support. I wish to thank N. Zitellini and F. Mulargia for their constructive comments and contributions. Finally I thank Eni for the concession to use the aeromagnetic data.

This thesis is dedicated to my family, Elena and Mattia.

Appendix: the magnetic field of a prismatic source

The magnetic field of a prismatic source has been intensively used throughout the thesis. Since one can be interested to perform again the work and the tests of the thesis, I will show the formula of the prismatic source field. The full calculation can be found in Bhattacharyya (1964) here the conclusive results are reported.

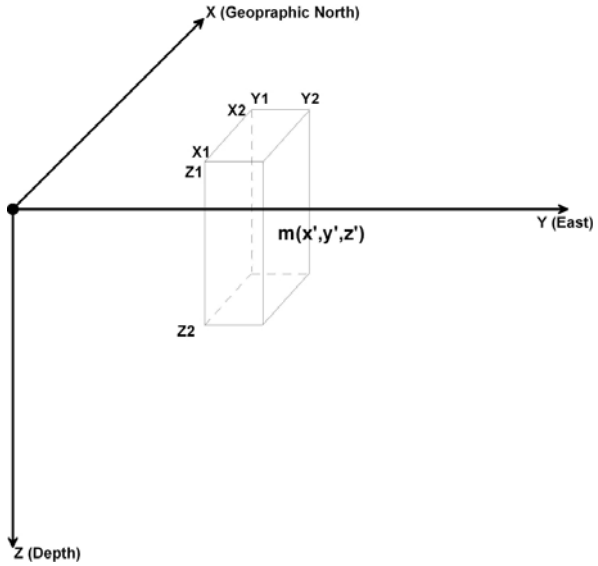

Figure 0.1: Geometry of the prismatic source

I define the next variables:

$$
\begin{array}{lll}
u_1 = x - x_2 & R_1 = u_1^2 + v_1^2 & R_7 = u_2^2 + w_1^2 \\
u_2 = x - x_1 & R_2 = u_1^2 + v_2^2 & R_8 = u_2^2 + w_2^2 \\
v_1 = y - y_2 & R_3 = u_2^2 + v_1^2 & R_9 = v_1^2 + w_1^2 \\
v_2 = y - y_1 & R_4 = u_2^2 + v_2^2 & R_10 = v_1^2 + w_2^2 \\
w_1 = z - z_2 & R_5 = u_1^2 + w_1^2 & R_11 = v_2^2 + w_1^2 \\
w_2 = z - z_1 & R_6 = u_1^2 + w_2^2 & R_12 = v_2^2 + w_2^2
\end{array}
$$

The relationship that connects the component of the magnetization vector $\mathbf{m}^t = (m_x; m_y; m_z)$ with the magnetic field $\mathbf{b}^t = (b_x; b_y; b_z)$ is given by

$$\begin{pmatrix} b_x \\ b_y \\ b_z \end{pmatrix} = \begin{pmatrix} T_{xx} & T_{xy} & T_{xz} \\ T_{yx} & T_{yy} & T_{yz} \\ T_{zx} & T_{zy} & T_{zz} \end{pmatrix} \cdot \begin{pmatrix} m_x \\ m_y \\ m_z \end{pmatrix}$$

The symmetric traceless tensor $\mathbf{T}$ has obviously 5 independent components that can be obtained one from the other by an appropriate rotation of the coordinate system. For this reason here I write only the expression for one component with coupled indexes:

$$T_{xx} = \begin{cases} & \arctan\left(\frac{v_2^2 w_2^2}{u_1\sqrt{w_2^2+R_2}}\right) - \arctan\left(\frac{v_1^2 w_2^2}{u_1\sqrt{w_2^2+R_1}}\right) \\ + & \arctan\left(\frac{v_1^2 w_1^2}{u_1\sqrt{w_1^2+R_1}}\right) - \arctan\left(\frac{v_2^2 w_1^2}{u_1\sqrt{w_1^2+R_2}}\right) \\ + & \arctan\left(\frac{v_1^2 w_2^2}{u_2\sqrt{w_2^2+R_3}}\right) - \arctan\left(\frac{v_2^2 w_2^2}{u_2\sqrt{w_2^2+R_4}}\right) \\ + & \arctan\left(\frac{v_2^2 w_1^2}{u_2\sqrt{w_1^2+R_4}}\right) - \arctan\left(\frac{v_1^2 w_1^2}{u_2\sqrt{w_1^2+R_3}}\right) \end{cases}$$

and one with mixed ones:

$$T_{xy} = \begin{cases} & \ln\left(\frac{w_2+\sqrt{w_2^2+R_1}}{w_1+\sqrt{w_1^2+R_1}}\right) - \ln\left(\frac{w_2+\sqrt{w_2^2+R_2}}{w_1+\sqrt{w_1^2+R_1}}\right) \\ + & \ln\left(\frac{w_2+\sqrt{w_2^2+R_4}}{w_1+\sqrt{w_1^2+R_4}}\right) - \ln\left(\frac{w_2+\sqrt{w_2^2+R_3}}{w_1+\sqrt{w_1^2+R_3}}\right) \end{cases}$$

The magnetic anomaly ΔF is obtaining projecting the magnetic anomalous field onto the ambient geomagnetic field with inclination I and declination D

$$\Delta F \simeq b_x \cos D \cos I + b_y \sin D \cos I + b_z \sin I$$

Appendix: Matlab routines

```
%%%%%%%%%%%%%%%%%%%%%%%% %COMMENT%%%%%%%%%%%%%%%%%%%%%%%%%%%%%%%%%%%%
                        MAIN PROGRAM MAGLAYER
Main program performing an apparent magentization map
Input data: geometry of the bottom and top of the study area, the
magnetic anomaly, inclination and declination of the magnetic field,
maximum and minimum value of magnetization
This program requires two function: magbox and dircos
%%%%%%%%%%%%%%%%%%%%%%%%END COMMENT%%%%%%%%%%%%%%%%%%%%%%%%%%%%%%%%%%%%

file_in=input('input scatter data file :','s')
Mat_input_scat=load(file_in);
cell_size=input('grid_cell_size: ');
main_inc=input('input inclination of main filed in degrees: ');
main_decl=input('input declination of main filed in degrees: ');
mag_inc=input('input inclination of the magnetization in degrees: ');
mag_decl=input('input declination of the magnetization in degrees: ');
azim=input('input north azimut in degrees: ');
Mag_min=input('input minimum value of magnetization: ');
Mag_max=input('input maximum value of magnetization: ');
X_scat=Mat_input_scat(:,2);
Y_scat=Mat_input_scat(:,1);
Top_scat=Mat_input_scat(:,5);
Bot_scat=Mat_input_scat(:,6) ;
An_scat=Mat_input_scat(:,3);
High_scat=Mat_input_scat(:,4);
X_min=min(X_scat);
X_max=max(X_scat);
Y_min=min(Y_scat);
Y_max=max(Y_scat);
X_g=X_min:cell_size:X_max;
Y_g=Y_min:cell_size:Y_max;
[East_grid,North_grid]=meshgrid(Y_g,X_g);
An_grid=griddata(Y_scat,X_scat,An_scat,East_grid,North_grid);
An_grid(isnan(An_grid))=0;
Top_grid=griddata(Y_scat,X_scat,Top_scat,East_grid,North_grid);
Top_grid(isnan(Top_grid))=0;
Bot_grid=griddata(Y_scat,X_scat,Bot_scat,East_grid,North_grid);
Bot_grid(isnan(Bot_grid))=0;
High_grid=griddata(Y_scat,X_scat,High_scat,East_grid,North_grid);
High_grid(isnan(High_grid))=0;
[ndataeast,ndatanorth]=size(An_grid);
```

```
for j=1:ndatanorth;
    MAT_x_g(:,j)=X_g';
end
for i=1:ndataeast;
    MAT_y_g(i,:)=Y_g;
end
k=0;
for i=1:ndataeast;
    for j=1:ndatanorth;
        if An_grid(i,j)~=0.
            k=k+1;
            an_dat(k)=An_grid(i,j);
            X_dat(k)=MAT_x_g(i,j);
            Y_dat(k)=MAT_y_g(i,j);
            high_dat(k)=High_grid(i,j);
            X1_pris(k)=MAT_x_g(i,j)-(0.5*cell_size);
            X2_pris(k)=MAT_x_g(i,j)+(0.5*cell_size);
            Y1_pris(k)=MAT_y_g(i,j)-(0.5*cell_size);
            Y2_pris(k)=MAT_y_g(i,j)+(0.5*cell_size);
            Z1_pris(k)=Top_grid(i,j);
            Z2_pris(k)=Bot_grid(i,j);
        end
    end
end
n_point=k;
h = waitbar(0,'Building the magnetization matrix...');
for i=1:n_point;
    waitbar(i/n_point)
    Mat_dat_par(i,:)=magbox(X_dat(i),Y_dat(i),high_dat(i),X1_pris,Y1_pris,...
        Z1_pris,X2_pris,Y2_pris,Z2_pris,mag_inc,mag_decl,main_inc,...
        main_decl,azim);
end
close(h);
v=size(an_dat);
nabla=zeros(v);
lb=nabla+Mag_min;
ub=nabla+Mag_max;

Mag_par=lsqlin(Mat_dat_par,an_dat,[],[],[],[],lb,ub);
Mag_grid=griddata(Y_dat,X_dat,Mag_par,East_grid,North_grid);
contourf(East_grid,North_grid,Mag_grid)
colorbar
```

```
% output data
X_dat=X_dat';
Y_dat=Y_dat';
Z1_pris=-Z1_pris';
Z2_pris=-Z2_pris';
an_dat=an_dat';
A=size(Mag_par');
B=zeros(A);
magnet=B+Mag_par';
C=magnet';
out=[X_dat,Y_dat,Z1_pris,Z2_pris,an_dat,C];
```

FUNCTION MAGBOX

Function to evaluate the magnetic field of a prismatic box with unitary magnetization, where (x0,y0,z0) indicates the spatial position of the data measurement and (x1,y1,z1,x2,y2,z2) are the coordinates of the corners of the box. The direction in degrees of the inducing field and the magnetization are indicated by (fi,fd) and (mi,md), while azim is the azimuth of the geographic north

```
function anbox=magbox(x0,y0,z0,x1,y1,z1,x2,y2,z2,mi,md,fi,fd,azim)
[mx,my,mz]=dircos(mi,md,azim);
[fx,fy,fz]=dircos(fi,fd,azim);
u1=(x0-x2);
u2=(x0-x1);
v1=(y0-y2);
v2=(y0-y1);
w1=(z0-z2);
w2=(z0-z1);
r1=u1.^2+v1.^2;
r2=u1.^2+v2.^2;
r3=u2.^2+v1.^2;
r4=u2.^2+v2.^2;
r5=u1.^2+w1.^2;
r6=u1.^2+w2.^2;
r7=u2.^2+w1.^2;
r8=u2.^2+w2.^2;
r9=v1.^2+w1.^2;
r10=v1.^2+w2.^2;
r11=v2.^2+w1.^2;
r12=v2.^2+w2.^2;
txx=+atan(v2.*w2./(u1.*sqrt(w2.^2+r2))) ...
    -atan(v1.*w2./(u1.*sqrt(w2.^2+r1))) ...
    +atan(v1.*w1./(u1.*sqrt(w1.^2+r1))) ...
    -atan(v2.*w1./(u1.*sqrt(w1.^2+r2))) ...
    +atan(v1.*w2./(u2.*sqrt(w2.^2+r3))) ...
    -atan(v2.*w2./(u2.*sqrt(w2.^2+r4))) ...
    +atan(v2.*w1./(u2.*sqrt(w1.^2+r4))) ...
    -atan(v1.*w1./(u2.*sqrt(w1.^2+r3)));
tyy=+atan(w2.*u2./(v1.*sqrt(u2.^2+r10))) ...
    +atan(w1.*u1./(v1.*sqrt(u1.^2+r9))) ...
    +atan(w1.*u2./(v2.*sqrt(u2.^2+r11))) ...
    +atan(w2.*u1./(v2.*sqrt(u1.^2+r12))) ...
    -atan(w1.*u2./(v1.*sqrt(u2.^2+r9))) ...
    -atan(w2.*u1./(v1.*sqrt(u1.^2+r10))) ...
```

```
    -atan(w2.*u2./(v2.*sqrt(u2.^2+r12))) ...
    -atan(w1.*u1./(v2.*sqrt(u1.^2+r11)));
tzz=-txx-tyy;
txy=+log((w2+sqrt(w2.^2+r1))./(w1+sqrt(w1.^2+r1))) ...
    -log((w2+sqrt(w2.^2+r2))./(w1+sqrt(w1.^2+r2))) ...
    +log((w2+sqrt(w2.^2+r4))./(w1+sqrt(w1.^2+r4))) ...
    -log((w2+sqrt(w2.^2+r3))./(w1+sqrt(w1.^2+r3)));
tyx=txy;
txz=+log((v2+sqrt(v2.^2+r5))./(v1+sqrt(v1.^2+r5))) ...
    -log((v2+sqrt(v2.^2+r6))./(v1+sqrt(v1.^2+r6))) ...
    +log((v2+sqrt(v2.^2+r8))./(v1+sqrt(v1.^2+r8))) ...
    -log((v2+sqrt(v2.^2+r7))./(v1+sqrt(v1.^2+r7)));
tzx=txz;
tyz=+log((u2+sqrt(u2.^2+r9))./(u1+sqrt(u1.^2+r9))) ...
    -log((u2+sqrt(u2.^2+r10))./(u1+sqrt(u1.^2+r10))) ...
    +log((u2+sqrt(u2.^2+r12))./(u1+sqrt(u1.^2+r12))) ...
    -log((u2+sqrt(u2.^2+r11))./(u1+sqrt(u1.^2+r11)));
tzy=tyz;
bx=txx.*mx+txy.*my+txz.*mz;
by=tyx.*mx+tyy.*my+tyz.*mz;
bz=tzx.*mx+tzy.*my+tzz.*mz;
anbox=100.*(bx.*fx+by.*fy+bz.*fz);
```

FUNCTION DIRCOS

Function to calculate the direction cosines from inclination and declination of the magnetic field

```
function [a,b,c]=dircos(incl,decl,azim)
Xincl=.017453293*incl;
Xdecl=.017453293*decl;
Xazim=.017453293*azim;
a=cos(Xincl)*cos(Xdecl-Xazim);
b=cos(Xincl)*sin(Xdecl-Xazim);
c=sin(Xincl);
```